Tunneling Spectroscopy of the Two-Dimensional Electron Gas

by

Ho Bun Chan

A.B. Physics
Princeton University, 1993

Submitted to the Department of Physics
in partial fulfillment of the requirements for the degree of

Doctor of Philosophy

at the

MASSACHUSETTS INSTITUTE OF TECHNOLOGY

September 1999

© Massachusetts Institute of Technology 1999. All rights reserved.

Author . . . .
Department of Physics
August 20, 1999

Certified by . . . .
Raymond C. Ashoori
Associate Professor
Thesis Supervisor

Accepted by . . . .
Thomas J. Greytak
Professor, Associate Department Head for Education

Tunneling Spectroscopy of the Two-Dimensional Electron Gas

by

Ho Bun Chan

Submitted to the Department of Physics
on August 20, 1999, in partial fulfillment of the
requirements for the degree of
Doctor of Philosophy

Abstract

We measure the single particle density of states (DOS) of a two-dimensional electron system (2DES) in a GaAs/AlGaAs heterostructure. Using a technique that we call "Time Domain Capacitance Spectroscopy" (TDCS), we measure the complete current-voltage characteristics for tunneling into the 2DES without making ohmic contacts to it. TDCS detects the tunneling current in regimes difficult to access by conventional methods, such as when the in-plane conductance is low. For the first time we detect the contributions of localized states to the tunneling current.

The DOS of an interacting 2DES in the diffusive limit displays logarithmic energy dependence near the Fermi level. Using TDCS, we measure the voltage dependence of the tunneling conductance of a semiconductor 2DES and observe the logarithmic Coulomb anomaly for the first time in 2D systems other than thin metal films. As we increase the density, this suppression in tunneling conductance narrows and recedes. Nevertheless suppression reappears when we apply a magnetic field perpendicular to the 2D plane. We find that the tunneling conductance depends linearly on voltage near zero bias for all magnetic field strengths and electron densities. Moreover, the slopes of this linear gap are strongly field dependent. The data are suggestive of a new model of the tunneling gap in the presence of disorder and screening.

We also use TDCS to study the interactions among electronic spins. By applying excitations less than kT, we observe that equilibrium tunneling into spin-polarized quantum Hall states (ν=1, 3, 1/3) occurs at two distinct tunneling rates for samples of very high mobility. Some electrons tunnel into the 2DES at a fast rate while the rest tunnel at a rate up to 2 orders of magnitude slower. Such novel double-rate tunneling is not observed at even-integer filling fractions where the 2DES is not spin-polarized. The dependence of the two rates on magnetic field, temperature and tunnel barrier thickness suggests that slow in-plane spin relaxation, possibly related to formation of Skyrmions, leads to a bottleneck for tunneling of electrons.

Thesis Supervisor: Raymond C. Ashoori

Title: Associate Professor

Acknowledgments

Throughout the six years of my graduate career, there have been many people who helped me.

First of all I would like to thank my advisor: Prof. Ray Ashoori. Few graduate students have the privilege of learning their skills directly from their advisor. Ray spent a huge amount of time with me in the lab to teach me the essential experimental skills, especially during my first two years here. Ray's energy and dedication have always inspired me. Ray gave me the opportunity to share the fun, and occasionally the frustration, of setting up a new lab. It is a remarkable experience to witness every piece of equipment arriving in the lab which was once completely empty.

I benefited a lot in learning from theorists. In particular, I would like to thank Prof. Leonid Levitov who is always patient in answering my questions. I received so much help from him that I regard him as a second mentor for my thesis. I would also like to thank Prof. Allan MacDonald for helping me to understand my data.

There are numerous people who contributed to the success of this thesis project. I am very grateful to Prof. Michael Melloch, Loren Pfeiffer and Ken West for growing our samples. Ilia Sokolinski constructed a prototype of the high frequency multipliers and wrote the main body of the software for the earlier version of the data averager that is essential to the success of this project. It was a pleasure working with Ilia. Misha Brodsky built both the multi-channel digital-analog converter and the cryogenic probe with rigid coax. I also thank Misha for putting up with me as his office-mate for six years. Paul Glicofridis built the second generation multipliers and summers, as well as mounted some of my early samples. He and Steve Moss selflessly devoted their time to take care of the helium liquidifier so that I could keep the dilution fridge cold. Omar Saleh built the rotating stage on a cryogenic probe, which enables me to measure tunneling in parallel and perpendicular magnetic fields. Sven Heemeyer arranged everything in order in the lab. Predrag Nikolic helped me with sample mounting and data acquisition in the previous year. I must thank Prof. Tom Greytak, Prof. Daniel Kleppner, Dale Fried, Tom Killian, David Landhuis and

Loren Willmann in the spin-polarized hydrogen group for letting me borrow their tools and equipment, especially during my first few years here. I also thank David Goldhaber-Gordon for helping me with latex when I am writing this thesis.

I am grateful to Prof. Peter Wolff, Nikolai Zhitenev, David Abusch-Magder and my undergraduate thesis advisor, Prof. Erramilli Shyamsunder who gave me useful career advice.

I enjoyed participating in the basketball team of our lab, named "Single Electrons." It was a lot of fun playing basketball with David Berman, Young Lee and Stuart Tessmer. It has also been a pleasure talking to and working with Gleb Finkelstein, Kazu Nomoto and Dima Pouchine.

Finally, I want to thank my family for their understanding and support in my choosing the career of physics. Physics is not an orthodox choice of career in the society I was brought up.

This work was supported by Office of Naval Research, National Science Foundation, DMR; Center for Materials Science, the Joint Services Electronics Program, and the Packard Foundation.

Contents

1 Introduction **13**

1.1 Introduction to 2D Electron Systems 15

1.2 Simplest picture of Tunneling Suppression 17

1.3 Thermodynamic and Single- Particle Density of States 18

1.4 Single-particle DOS and Tunneling Conductance 19

2 Time Domain Capacitance Spectroscopy **22**

2.1 Limitations of Conventional Tunneling Measurements 23

2.2 Sample Design 25

2.3 Basic Concepts 28

2.3.1 Setting up Voltage across the Tunnel Barrier 28

2.3.2 Detecting the Tunneling Current 30

2.3.3 Data averaging 33

2.3.4 Typical I-V curves 34

2.4 Schematic of Setup 35

2.4.1 Pulse Sequence 37

2.4.2 Measuring Low Frequency Capacitance by Balancing the Bridge 38

2.4.3 Fitting Procedure 40

2.4.4 Summary 42

3 Zero-bias Coulomb Anomaly for Tunneling into disordered 2D Electronic Systems **45**

3.1 Origin of the Logarithmic Correction to the single particle DOS: Qualitative Picture 47
3.2 Samples 50
3.3 Experimental Result 52
3.3.1 Explanation of the Asymmetry in the Conductance Curves . . 54
3.3.2 Normalization Procedure and Logarithmic DOS Correction . . 56
3.4 Significance of measuring the Coulomb anomaly in semiconductor 2DEG 59
3.4.1 GaAs quantum wells define purely 2D systems 59
3.4.2 Short Screening Length for 2DEG in GaAs 61
3.4.3 DOS Corrections in the quasi-ballistic regime 62
3.5 Breakdown of Logarithmic Voltage Dependence at Large Corrections 63
3.5.1 Semi-classical Theory of the Coulomb Anomaly 64
3.5.2 Fitting Power Law to Data at large tunneling suppression . . 66
3.6 Enhancement of tunneling conductance by weak magnetic field 68
3.6.1 Zero-bias conductance in a weak magnetic field 68
3.6.2 Measurements in perpendicular and parallel fields 70
3.6.3 Weak localization effects on tunneling conductance 72
3.6.4 Cooper channel interactions in a disordered 2DEG 74
3.7 Summary 77

4 Linear Energy Gap for Tunneling into the 2DEG in perpendicular Magnetic Field 78
4.1 Samples 80
4.2 Linear Dependence of Tunneling conductance on Voltage 82
4.3 Comparison of TDCS data to tunneling data from double quantum wells 89
4.4 Linear Coulomb gap with universal slope in 2D 90
4.5 Coulomb Blockade Gap 94
4.6 Conclusion 98

5 Tunneling into Ferromagnetic Quantum Hall States: Observation of a Spin Bottleneck 99

5.1 Spin Physics for the $\nu = 1$ Ferromagnetic State 101
5.2 Samples 104
5.3 Equilibrium Tunneling at $\nu = 1$ 106
5.4 Sample Inhomogeneity: Comparison between Tunneling at $\nu = 1$ and $\nu = 2$ 111
5.5 Tunneling of Spin-up and Spin-down Electrons 113
5.6 Energy Scale of the Double-rate Phenomenon 116
5.7 Phase Separation vs. In-plane Relaxation 120
5.8 Spin Bottleneck for Tunneling 122
5.9 MacDonald's Model for Tunneling at $\nu = 1$ 123
5.9.1 General Formalism 123
5.9.2 Coupling of the Two spin subsystems through $dN_\uparrow/d\mu_\downarrow$ and $dN_\downarrow/d\mu_\uparrow$ 126
5.10 Comment on double tunneling rates at $\nu = 3$ 128
5.11 Comparison to result from another research group 129
5.12 Summary 129

6 Future Prospects **131**
6.1 Tunneling into $\nu = 1$ at tilted Magnetic Fields 132
6.2 Coulomb Anomaly in high mobility sample 132
6.3 Single Particle Density of States in a non-quantizing Magnetic Field . 133
6.4 Excitation Voltage Study of the Tunneling Enhancement at weak magnetic field 134
6.5 Excitation Voltage Dependence of Tunneling Conductance at Even Denominator Filling Factors 134
6.6 Reproducible Fluctuations in Equilibrium tunneling conductance . . . 135
6.7 Tunneling Rates into Quantum Dots and Spectroscopy of Excited States 138

A Extracting the Tunneling Current from Response of the Sample to a Step Voltage **141**

B Increasing Voltage Resolution by Digital Dithering **146**

C Sample Fabrication **149**

C.1 Fabrication Procedure for Samples with Schottky Top Electrode . . . 150

C.2 Fabrication Procedure for Samples with Ohmic Top Electrode 151

List of Figures

1-1 Energy diagram for two systems separated by a tunnel barrier. 19

2-1 Schematic of conventional tunneling measurement of tunneling into the 2DEG. 24
2-2 Schematic of tunneling measurement using TDCS 25
2-3 Structure of the samples 26
2-4 Evolution of the conduction band energy of our sample during cycle of measurement. 29
2-5 Capacitance bridge measuring the tunneling current. 31
2-6 Time traces with and without data averaging. 32
2-7 I-V curves obtained by TDCS. 34
2-8 Schematic of TDCS 36
2-9 Sequence of pulses applied in TDCS 39
2-10 Low frequency capacitance at 3T. 41
2-11 Time traces demonstrating the effect of a voltage dependent tunneling resistance. 43

3-1 Interference between two particles undergoing diffusive motion. 48
3-2 The essential layer structure of the samples. 51
3-3 Tunneling conductance versus voltage at zero field for low electron densities 53
3-4 Momentum conservation for tunneling between a 3D and a 2D system. 55
3-5 Normalizing the conductance curves. 56
3-6 Normalized tunneling conductance plotted on a semilog scale. 57

3-7 In-plane resistivity and scattering time vs. electron density 60
3-8 Spreading of charge under the Coulomb barrier 64
3-9 Power law fit to the tunneling conductance at low electron density . . 67
3-10 Zero-bias tunneling current vs. magnetic field for different densities . 69
3-11 Tunneling current dependence on perpendicular and parallel magnetic fields 71
3-12 Qualitative picture of weak localization. 73
3-13 Qualitative picture of Cooper channel interaction. 74

4-1 Simplest picture of the magnetic field induced gap 79
4-2 The essential layer structure of the samples. 81
4-3 Tunneling conductance vs. voltage for various magnetic fields 83
4-4 Tunneling conductance vs. voltage for various magnetic fields 84
4-5 Tunneling conductance vs. voltage near zero bias for six different magnetic fields. 85
4-6 The dependence of the slope of the linear gap on inverse field strength. 86
4-7 Tunneling conductance vs. voltage for various magnetic fields in sample m060296a. 87
4-8 The dependence of the slope of the linear gap on inverse field strength for sample m060296a. 88
4-9 Simulated I-V curve for tunneling between two 2DEG's. 90
4-10 Energy diagram illustrating the Coulomb gap. 91
4-11 Energy diagram of the charge transfer process into a single puddle. . 94
4-12 Coulomb blockade gap model for the tunneling suppression. 95

5-1 Qualitative picture of Skyrmions at $\nu = 1$. 102
5-2 Layer structure and equivalent circuit model of high mobility samples 105
5-3 Linear dependence of the tunneling conductance on excitation voltage in a magnetic field for high mobility samples. 107
5-4 Comparison of recorded signal at $\nu = 1$ and $\nu = 1.5$. 108
5-5 Dependence of the relaxation rate on sample bias at 3.8 T. 110

5-6 Comparison of recorded signal at ν =1 and $\nu = 2$. 112
5-7 Effect of density inhomogeneity on tunneling at $\nu = 1$. 114
5-8 Dependence of relaxation rate and capacitance on sample bias at 5.7T. 115
5-9 Temperature dependence of the fast and slow relaxation rates. 117
5-10 Dependence of the characteristic temperature on magnetic field. . . . 118
5-11 Figure demonstrating that the double-rate tunneling phenomenon disappears at a temperature when the exchange gap is present. 119
5-12 Relaxation rates dependence on tunnel barrier thickness at $\nu = 1/2$ and at $\nu = 1$. 121

6-1 Reproducible fluctuations in tunneling conductance as the sample bias is increased in fine steps. 136
6-2 Evolution of the fluctuations as the magnetic field varies. 137
6-3 Application of TDCS to measure excited states in a quantum dot. . . 139

A-1 Band structure of the samples 142

B-1 Simple picture demonstrating the concept of dithering. 147
B-2 Choosing the dithering voltages. 148

Chapter 1

Introduction

The physics of the two-dimensional electron gas (2DEG) has been a subject of intensive research for several decades. Nonetheless, new and exciting physics of the 2DEG continues to be generated. Topics such as the quantum Hall effect in strong perpendicular magnetic fields and the possibility of existence of a 2D conducting phase remain subjects of strong current interest.

The transport properties of the 2DEG have been extensively studied in Si/SiO_2 and $GaAs/AlGaAs$ systems. The vast majority of these experiments apply an electrical current in the plane of the 2DEG and measure the corresponding voltage drop in directions parallel or perpendicular to the current in order to determine the in-plane resistance or Hall resistance. This thesis, in contrast, focuses on experiments in which electron transport takes place via tunneling in the direction normal to the 2D plane. By measuring the tunneling current, we study the response of the 2D system when an extra electron is injected into it in a tunneling event.

Tunneling experiments have proven to be a powerful probe of correlations in 2D systems. However, due to a number of experimental difficulties, there have been few experiments that measure the tunneling current into a 2DES, in contrast to the large number of experiments measuring transport within the 2D plane. First, in conventional tunneling measurements, electrons that tunnel into a 2D system introduce charge which must be removed from the system to avoid local charge accumulation at long time scales. This is achieved by conduction within the 2D plane. As a result,

conventional measurement schemes can only detect contributions from conducting or extended electron states. The energetics of tunneling into localized sites, though of great theoretical interest, have not been measured experimentally. A second technical problem arises due to the difficulty in making an electrical contact to the 2D layer in semiconductor heterostructures without shorting it to the reservoir providing the tunneling electrons.

In this thesis, we measure tunneling into the 2DEG using a technique we called "Time Domain Capacitance Spectroscopy" (TDCS), which we developed to circumvent the above problems. Using TDCS, we measure the complete current-voltage (I-V) characteristics for tunneling into the 2DEG without making direct electrical contacts to it. TDCS enables us to detect the tunneling current in regimes difficult to access by conventional methods, such as when the in-plane conductance of the 2DEG is low. For the first time we are able to detect the contributions of localized states to the tunneling current.

We describe TDCS in detail in Chapter 2. In Chapter 3, we perform a TDCS study of the zero-bias logarithmic Coulomb anomaly of the tunnel conductance into a disordered interacting 2D system in zero magnetic field. In Chapter 4, we show that in a perpendicular magnetic field, the tunneling conductance varies linearly with voltage. The slope of this linear gap depends strongly on magnetic field. We propose a "Coulomb Blockade Gap" model to explain our data. In Chapter 5 we use TDCS to study spin effects on tunneling into 2D systems at special densities and magnetic field when the system is ferromagnetic. We demonstrate that non-equilibrium spin accumulation leads to a suppression of tunneling current.

The rest of this chapter gives a brief introduction to 2D electron systems and explains why tunneling measurements are powerful probes of electron-electron interactions.

1.1 Introduction to 2D Electron Systems

Two-dimensional electron systems of high mobility are usually created in GaAs/AlGaAs heterostructures grown by molecular beam epitaxy (MBE). MBE has the capability of controlling the crystal composition down to a single atomic layer. One can therefore utilize the conduction band offset between GaAs and AlGaAs to define structures such as potential wells and barriers with atomic resolution. By introducing dopants at appropriate positions, electrons accumulate at the GaAs/AlGaAs interface or in GaAs quantum wells. For a 150 $\mathring{A}$ GaAs quantum well, the confinement results in a separation of about 50 meV between the first and second subband, while the Fermi energy is only 3.6 meV at typical 2D electron density of $1 \times 10^{11} cm^{-2}$. Since we perform our measurement at a temperature of < 1 K (equivalent to 0.1 meV), we can ignore thermal activation of electrons to the second subband and treat electrons in the quantum well as a purely two-dimensional system.

In the absence of a magnetic field, the density of states (DOS) in two dimensions is a constant, dependent only on fundamental constants and the effective mass of the confined electrons. Application of a perpendicular magnetic field has profound effects on 2D systems. In a single particle picture and with no disorder in the 2DEG, the magnetic field essentially confines electrons laterally in identical harmonic oscillator potentials, the number of which equals the number of magnetic flux quanta passing through the 2D system. The resultant quantum energy levels, known as Landau levels, are equally spaced in energy and highly degenerate. Both the degeneracy and the separation between adjacent Landau levels increase linearly with magnetic field. Classically, the degeneracy corresponds to electrons performing cyclotron motion with the same energy at different spatial locations. Therefore, the DOS of an ideal 2D system in a magnetic field consists of a series of delta functions. In a real system with disorder, the Landau levels broaden.

The filling factor ν is the number of Landau levels filled with electrons. One can control ν by changing the 2D electron density at a constant magnetic field to fill the Landau levels successively. Alternatively one can maintain the 2D system at a fixed

density while changing the magnetic field so that ν changes due to variation in the degeneracy of the Landau levels.

In 1980, von Klitzing, Dorda and Pepper [1] measures the transport properties of a 2D system formed at the inversion layer of the Si/SiO_2 system and discovered the quantum Hall effect. They found that as the magnetic field increases, the Hall resistance of a 2DEG rises in steps instead of linearly like in ordinary bulk semiconductors or metals. Each plateau on the Hall resistance is quantized very accurately to the value $\nu h/e^2$, where h is the Planck's constant and e is the electronic charge. At precisely the magnetic fields when the Hall resistance displays steps, the longitudinal (in-plane) conductance drops to zero.

Basic theories of the quantum Hall effect rely on finite DOS between Landau levels. Electronic states between Landau levels are localized while the states in the middle of a Landau level are extended. The Hall plateaus occur around integer filling factors when the chemical potential lies between Landau levels. Since the states near the chemical potential are localized, the 2D system behaves effectively as an insulator at integer fillings. One of the key contributions of this thesis is that we measure tunneling in the quantum Hall regimes when the states at the chemical potential are localized and the in-plane conductance vanishes.

Two-dimensional systems also have remarkable spin properties due to the interplay between Zeeman coupling of electronic spins to an applied magnetic field and Coulomb interactions among electrons. When the lowest Landau level is filled with electrons with a single spin orientation ($\nu = 1$), exchange interactions align electron spins to form a nearly perfect ferromagnet [2]. Recently, theorists predicted that the elementary charge excitations of this $\nu = 1$ quantum Hall state consist of spin textures known as Skyrmions [3, 4]. In Chapter 5, we elaborate on spin properties of these ferromagnetic quantum Hall states and describe our tunneling study of interactions among electronic spins.

1.2 Simplest picture of Tunneling Suppression

The interplay among electron-electron interactions, disorder and/or magnetic field leads to the formation of an energy gap in the single particle density of states (DOS) at the chemical potential [5, 6].

In the simplest picture we can understand the suppression of DOS in the following way: Suppose we start with a fix number of electrons in a disordered background potential. In the ground state, electrons will arrange themselves at positions which minimize their energy with respect to both the disorder potential and their mutual repulsion. Tunneling injects an extra electron suddenly into the system. In general this is not the ground state of the new system. The extra electron has a high Coulomb energy and the system must relax to accommodate the new electron. An electron must pay an extra energy cost in order to tunnel into the system. In other words, there is a reduction in the DOS or the development of a pseudogap near the Fermi energy.

This pseudogap has some unique and remarkable properties. First, it exists even when the 2DEG is compressible, such as at $\nu = 1/2$, where in-plane transport measurements display no activation behavior. Second, the pseudogap, if observable, is always pinned at the chemical potential, in contrast to ordinary band gaps in semiconductors that are fixed in energy. For instance, if the 2D electron density increases by a factor of two, a pseudogap develops at the new chemical potential. These properties arise from the difference the single particle DOS and thermodynamic DOS that will be the subject of the next section.

Different theoretical models lead to entirely different shapes of the pseudogap in the single particle DOS. The exact energy dependence is determined by a number of different factors such as the degree of localization of electronic states, the filling factor ν in the presence of magnetic field, and/or the effectiveness of screening. We will discuss in the later chapters four different models that we believe are the most relevant to our experiment. In Chapter 3, we will describe the logarithmic Coulomb anomaly in tunneling conductance for a diffusive 2D electron system, as well as a semi-classical model that predicts the tunneling conductance varying as power law of

voltage with the exponent determined by the in-plane conductance. In Chapter 4 we will derive the Coulomb gap for a classical system of localized point charges. We will also present in the same chapter a "Coulomb blockade gap" model that we proposed to explain our tunneling data qualitatively.

1.3 Thermodynamic and Single- Particle Density of States

As described in the last section, the tunneling of an electron into or out of the 2DEG may force the system into a non-equilibrium state. This requires the definition of two different DOS: thermodynamic DOS for a system that has relaxed to equilibrium and single-particle DOS that describes the non-equilibrium situation. In this section, we clarify the difference between these two quantities.

The thermodynamic DOS, $\delta N/\delta\mu$, is the change in particle density N of a system for a change in chemical potential μ after a time interval longer than the internal equilibration time of the system. For instance, in low frequency capacitance experiments (described in section 2.4.2), we measure $\delta N/\delta\mu$ by modulating the potentials slowly so that the system evolves reversibly during the course of measurement.

On the other hand, measurements of tunneling conductance yield the single-particle DOS. The single-particle DOS is relevant when the system does not have sufficient time to rearrange during the sudden injection of an electron. In the presence of electron-electron interaction, a pseudogap develops in the single particle DOS reflecting the non-equilibrium accumulation of charge at short time scales. The single-particle DOS may be significantly smaller than the thermodynamic DOS. For instance, in a strong magnetic field the single particle DOS at the chemical potential may be suppressed by several orders of magnitude from the thermodynamic value.

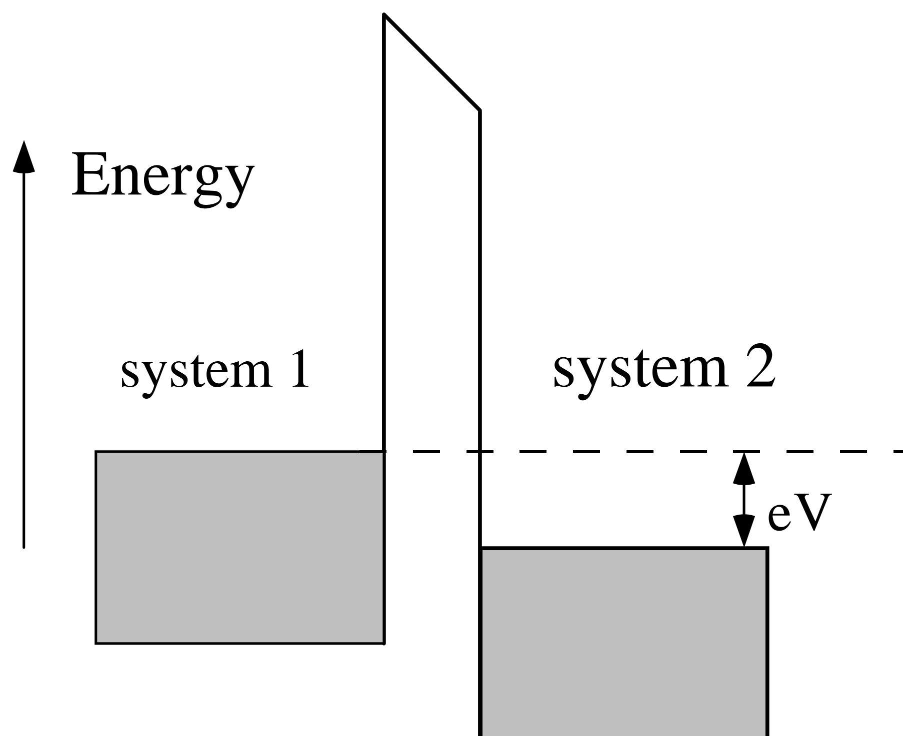

Figure 1-1: Energy diagram for two systems separated by a tunnel barrier.

1.4 Single-particle DOS and Tunneling Conductance

In this section, we will show that measurement of the differential tunneling conductance as a function of voltage yields directly the single-particle DOS as a function of energy.

In Fig. 1-1, a potential barrier separates system 1 and system 2 with electrochemical potential difference of eV. The potential barrier is thin enough so that electrons can tunnel through it under appropriate conditions. One requirement is that there must be a filled state in one system and an empty state at a corresponding energy in the other system. We obtain the tunneling current by integrating over states that

satisfy the above criteria:

$$
\begin{aligned}
I_{tunnel} &= I_{12} - I_{21} && (1.1)\\
&\propto -\frac{e}{\tau}\int_{-\infty}^{\infty} n_1(E-eV)f(E-eV)n_2(E)(1-f(E))dE \\
&\quad +\frac{e}{\tau}\int_{-\infty}^{\infty} n_1(E-eV)(1-f(E-eV))n_2(E)f(E)dE && (1.2)\\
&= \frac{e}{\tau}\int_{-\infty}^{\infty} n_1(E-eV)n_2(E)[f(E)-f(E-eV)]dE && (1.3)
\end{aligned}
$$

where I_{12} is the current from system 1 to 2, e is magnitude of the electronic charge, τ is the average time interval between tunneling events (determined by the barrier thickness and height), $f(E)$ is the Fermi distribution, $n_1(E)$ and $n_2(E)$ are the density of states of system 1 and 2 respectively. In our experiment, system 1 is a highly doped 3D semiconductor that has a featureless DOS for small voltages. Therefore we can assume $n_1(E)$ to be constant over our range of interest. The differential tunneling conductance G then becomes:

$$
G = \frac{dI_{tunnel}}{dV} \propto \frac{e^2}{\tau} n_1 \int_{-\infty}^{\infty} n_2(E) \frac{df(E-eV)}{E} dE \qquad (1.4)
$$

At temperature $T = 0$, the derivative of the Fermi function reduces to a delta function, further simplifying the expression for dI_{tunnel}/dV:

$$
\frac{dI_{tunnel}}{dV} \propto n_2(eV) \qquad (1.5)
$$

The tunneling differential conductance is thus directly proportional to the single particle DOS at low temperatures.

As we will describe in Chapter 2, our experimental setup measures the tunneling conductance I/V instead of the differential conductance dI/dV. Although we can convert I/V to dI/dV by simple differentiation, this process generates a considerable amount of noise. We therefore analyze most data presented in this thesis in the form I/V. This does not introduce any complications to analysis since I/V preserves power

law or logarithmic dependence in dI/dV. For the case of logarithmic dI/dV:

$$\frac{dI}{dV} = A_1 + A_2 \log(V) \tag{1.6}$$

$$I = (A_1 - A_2)V + A_2 V \log(V) \tag{1.7}$$

$$\frac{I}{V} = (A_1 - A_2) + A_2 \log(V) \tag{1.8}$$

where A_1 and A_2 are arbitrary constants. For power law with any exponent α and prefactor A_3:

$$\frac{dI}{dV} = A_3 V^{\alpha} \tag{1.9}$$

$$I = \frac{A_3}{\alpha + 1} V^{\alpha+1} \tag{1.10}$$

$$\frac{I}{V} = \frac{A_3}{\alpha + 1} V^{\alpha} \tag{1.11}$$

So far, we have only observed logarithmic or power law I/V with different exponents in our measurements.

We proceed with Chapter 2 that describes TDCS, a novel technique we developed to measure the tunneling conductance.

Chapter 2

Time Domain Capacitance Spectroscopy

In this chapter we will describe "Time Domain Capacitance Spectroscopy" (TDCS). We developed TDCS to obtain most of the data presented in this thesis. TDCS measures the tunneling current-voltage (I-V) characteristics into mesoscopic semiconductor systems such as two-dimensional electron gas (2DEG) or quantum dots, in regimes not accessible by conventional tunneling measurements. First, TDCS enables us to measure the tunneling current into a 2DEG at arbitrary low in-plane conductance. For the first time we are able to measure the contribution of localized states to the tunneling current. Second, TDCS measures the complete tunneling current-voltage characteristics without making an ohmic contact to the 2DEG. As we will describe in section 2.1, making electrical contacts to mesoscopic semiconductor systems is often difficult, or even impossible in some cases.

TDCS is an extension of AC capacitance measurements on similar samples by Ashoori [7]. The AC technique measures the sample impedance over a wide frequency range to extract the zero-bias tunneling conductance. TDCS, like the AC technique, utilizes a capacitance bridge as the external circuit for detection of the tunneling signal. However, TDCS measures the tunneling signal in real time, in response to a step excitation. Effectively we measure tunneling at all frequencies in a single time trace, provided we repeat the step excitation enough times to signal-average the time

response to recover it from noise. Moreover, application of step excitations allows us to measure the tunneling conductance away from zero-bias and obtain the complete tunneling I-V characteristics, which is often highly non-linear and asymmetric in voltage. From the tunneling I-V, we can deduce the single-particle density of states (DOS) which contains a gap at the Fermi level due to electron-electron interactions, as we described in Chapter 1.

We begin with a review of conventional methods of tunneling measurement and their limitations. Next, we describe our sample design and experimental apparatus for TDCS. In particular, we explain how we set up a voltage across the tunnel barrier even though we do not have an ohmic contact to the 2DEG, and how we manage to detect the tunneling current into localized electronic states. Often we need to make measurements at very low excitations (<10 μV) and signal levels. In some cases it is necessary to signal-average more than 250,000 times to recover the tunneling signal from noise. Ordinary oscilloscopes do not have the data throughput and voltage resolution necessary to recover the signal from noise. We will describe in detail an efficient signal averager we used in place of oscilloscopes.

2.1 Limitations of Conventional Tunneling Measurements

Figure 2-1 shows the conventional experimental setup for measuring tunneling into a two-dimensional (2D) system. Typically one makes an electrical contact at the edge of the 2D system to apply a voltage across the tunneling barrier and to measure the tunneling current. The major limitation is that the in-plane conductance (σ_{2D}) must be much larger than the tunneling conductance (σ_{tunnel}). Otherwise the voltage drops in the 2D plane and the measurement represents transport within the 2D plane instead of across the tunnel barrier. In the extreme case when an electron tunnels into a localized state, it is not possible to detect its contribution to the tunneling current, because it cannot leave the 2D plane through in-plane conduction. As a

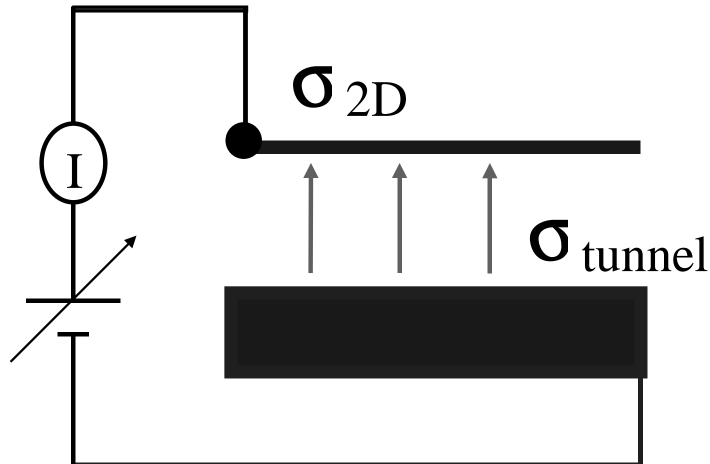

Figure 2-1: Schematic of conventional tunneling measurement of tunneling into the 2DEG.

result, this method cannot measure tunneling current into localized states. It does not work when the 2D in-plane conductance is low, such as at low electron densities or at magnetic fields when the 2DEG is in the quantum Hall regime.

Tunneling experiments into metal films were performed in the 1980's [8, 9, 10, 11, 12, 13, 14]. In some cases, a superconducting metal film is chosen to get around the in-plane resistance problem [9]. Tunneling experiments become even more challenging if one wants to study semiconductor 2D systems in which the quantum Hall effect occurs. 2D systems in semiconductors are embedded within the semiconductor crystal. To make an ohmic contact to the 2D system one typically puts layers of specific metals on the surface of the semiconductor. It is necessary to anneal the metal at a high temperature so that it diffuses from the crystal surface into the 2D system. It is very difficult to control precisely how deep the metal penetrates. When one achieves good electrical contact to the 2DEG, most of the time the metal has diffused all the way to short out the tunnel barrier, making it impossible to measure tunneling. Eisenstein [15] uses a clever selective gating technique to make separate ohmic contacts to two 2D systems in GaAs. However, there still is the problem of in-plane resistance. For the reasons mentioned in this section, there are only a limited number of tunneling experiments on 2D electron systems. The motivation of this

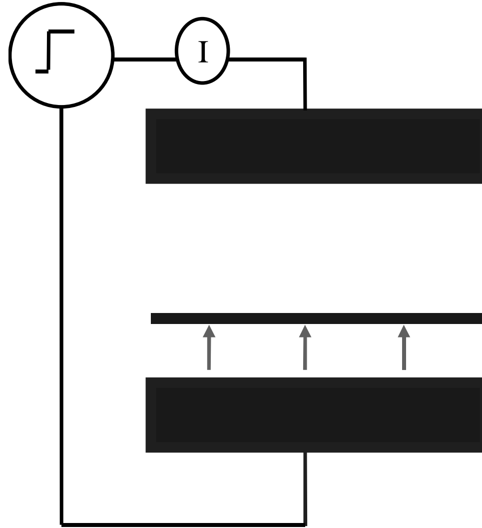

Figure 2-2: TDCS measures tunneling without making any ohmic contacts to the 2DEG.

thesis is to develop an alternative experimental technique capable of measuring the tunneling I-V characteristics at arbitrary low in-plane conductance.

2.2 Sample Design

Using TDCS, we measure the tunneling current using a slightly different approach. As shown in Figure 2-2, we do not make ohmic contacts to the 2D system. We sandwich it between two capacitor plates, close to the bottom one to allow tunneling. There is no charge transfer between the quantum well and the top electrode. Instead of performing a DC measurement as in Figure 2-1, we apply sharp voltage steps to our structure to induce tunneling of electrons back and forth across the tunnel barrier. We deduce the tunneling current by analyzing the time response of the structure to the voltage steps. A DC bias to the top gate repels or attracts electrons into the 2D sheet, permitting variation of the 2D electron density. The 3D substrate remains conducting all the time. Electrons can tunnel everywhere into the 2DEG even when the in-plane conductance is very low.

Figure 2-3(a) shows the structure of our first samples. The sample is a GaAs/AlGaAs

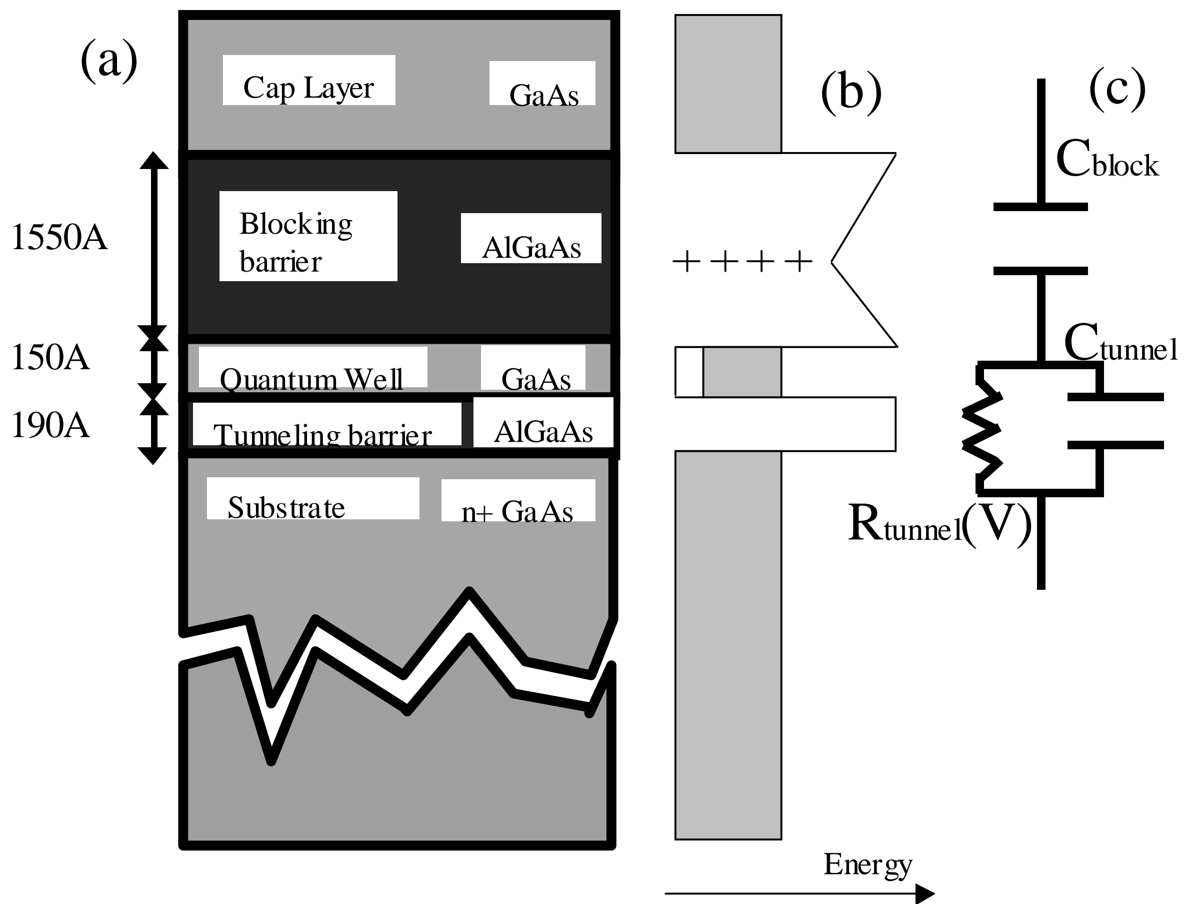

Figure 2-3: (a) Structure of our samples with typical layer thickness. (b) Conduction band energy diagram of our samples. (c) Equivalent circuit diagram of our samples.

heterostructure grown by molecular beam epitaxy. Figure 2-3(b) displays the corresponding conduction band diagram. Our substrate is n+ doped GaAs. On top of that we grow an AlGaAs tunnel barrier followed by a GaAs quantum well, which defines our 2D system. The AlGaAs blocking barrier is thick and prevents conduction between the 2D system and the GaAs top electrode. For these early samples, we introduce dopants in the AlGaAs to provide electrons for the quantum well. The GaAs cap layer is undoped, with chromium-gold Schottky contact acting as the gate. We perform our measurement on a mesa of 400 μm. Our recent samples contain modifications to the above design and have less disorder. We will describe these high mobility samples in Chapter 5.

Figure 2-3(c) shows the equivalent circuit elements representing the sample. We model the tunnel barrier by a capacitor C_{tunnel} in parallel with tunneling resistance R_{tunnel}. Since there is no charge transfer between the quantum well and the top electrode, we model the blocking barrier as a single capacitor C_{block}. As we discussed in Chapter 1, the tunneling current into a 2DEG can be strongly suppressed at small voltages due to electron-electron interactions. Hence R_{tunnel} is not a linear circuit element. In Figure 2-3(c) we deliberately label it as $R_{tunnel}(V)$ to emphasize the fact that its value depends on the voltage V across the tunnel barrier. In Chapters 3 and 4, we study the effect of electron-electron interactions in the 2DEG through the dependence of the R_{tunnel} on V.

Earlier experiments by Ashoori [7] used AC capacitance measurements over a broad frequency range to measure "zero-bias" tunneling in similar samples. In "zero-bias" tunneling (also known as "equilibrium tunneling"), one applies excitation voltages with amplitude less than the thermal energy kT. R_{tunnel} is independent of excitation voltage in this linear response limit and behaves as a linear circuit element. Therefore one can extract R_{tunnel} by fitting the frequency dependence of the sample impedance with suitable choices of the three circuit elements C_{tunnel}, R_{tunnel} and C_{block} in Fig. 2-3(c). However, experimental data obtained using excitation voltages larger than kT are difficult to interpret because the tunneling I-V characteristic is often non-linear and/or asymmetric. In fact, one of the motivations for this thesis

is to develop a technique capable of measuring the non-ohmic $R_{tunnel}(V)$ at large excitation voltages and extracting the complete I-V characteristics for tunneling.

The simple equivalent circuit of the sample in Fig. 2-3(c) represents the sample well under most conditions. However, for magnetic fields at which a 2DEG with low level of disorder is in the $\nu = 1$ state (with the lowest Landau level filled with electrons with a single spin direction), we find unexpectedly that electrons tunnel at two distinct rates. The equivalent circuit of the sample in Fig. 2-3(c) does not describe the sample adequately. We believe the double tunneling rate phenomenon arises from non-equilibrium spin accumulation and will discuss this effect in detail in Chapter 5.

2.3 Basic Concepts

This section explains the basic concept of TDCS. We will discuss how we set up a voltage across the tunnel barrier and detect the tunneling current in the samples described in the last section.

2.3.1 Setting up Voltage across the Tunnel Barrier

Here we describe how we set up a voltage across the tunneling barrier even though we do not have ohmic contacts to the sample. Figure 2-4 shows the time evolution of the conduction band energy during one cycle of measurement. We start with the 2D system in equilibrium with the 3D electrode and their Fermi energies aligned. At time $t = 0$, we apply a sharp voltage step to the bottom electrode. This voltage drops evenly across the sample and creates a voltage offset on the two sides of the tunnel barrier, inducing a tunneling current. As electrons tunnel, this offset equilibrates and we record the decay signal in real time. At sufficiently long times there will be no potential difference between the 2DEG and 3D substrate.

The reason that we are able to extract the tunneling IV is that before we applied the voltage step, the entire 2D plane is at the same potential. Immediately after we applied the voltage step, no extra charge has entered the 2D system and the 2D plane

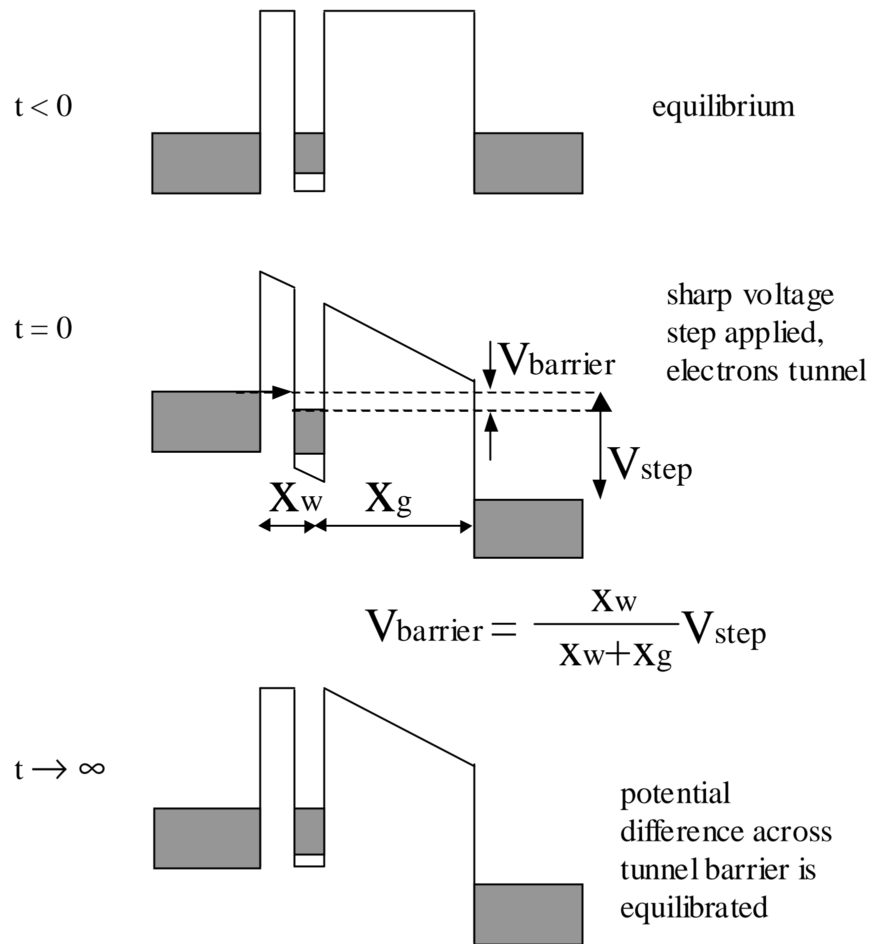

Figure 2-4: Evolution of the conduction band energy of our sample during cycle of measurement.

remains equipotential even when the in-plane conductance is very low. Immediately after the voltage step is applied, the voltage across the tunnel barrier is simply a fraction of the voltage step applied. Its precise value depends on the thickness of our layers:

$$V_{barrier} = \frac{x_w}{x_w + x_g} V_{step} \tag{2.1}$$

where x_w is the separation between the quantum well and the bottom 3D substrate and x_g is the separation between the quantum well and the top gate. Therefore we managed to set up a known voltage across the tunnel barrier, but only for a brief instant because this voltage difference decays with time.

2.3.2 Detecting the Tunneling Current

To measure tunneling, we need to create a voltage difference across the tunnel barrier and detect the current. In the last section we discuss how to set up a voltage when we do not have an ohmic contact to the sample. Next I will describe how we measure the tunneling current.

Figure 2-5 shows the capacitance bridge that we used to measure the tunneling current. The three sheets on the left represent our sample, the top electrode, the bottom electrode and the 2D system of interest. When electrons tunnel from the 3D substrate into the 2D system, they repel electrons in the top electrode, leading to a displacement current I_D flowing out. I_D charges a standard capacitor C_S of known value and we detect the voltage V_S across C_S using a high electron mobility transistor (HEMT). We record the output of the transistor as a function of time. Figure 2-6b shows a typical time trace recorded. The current flowing into a capacitor is proportional to the time derivative of the voltage across it. Therefore, we can deduce the tunneling current by taking the initial time derivative of our recorded signal:

$$I_{tunnel} = -C_{\Sigma} \frac{dV_S}{dt} \tag{2.2}$$

Again the proportionality constant C_{Σ} depends on the thickness of the layers in our sample. Appendix A gives a detailed derivation for Eq. 2.2.

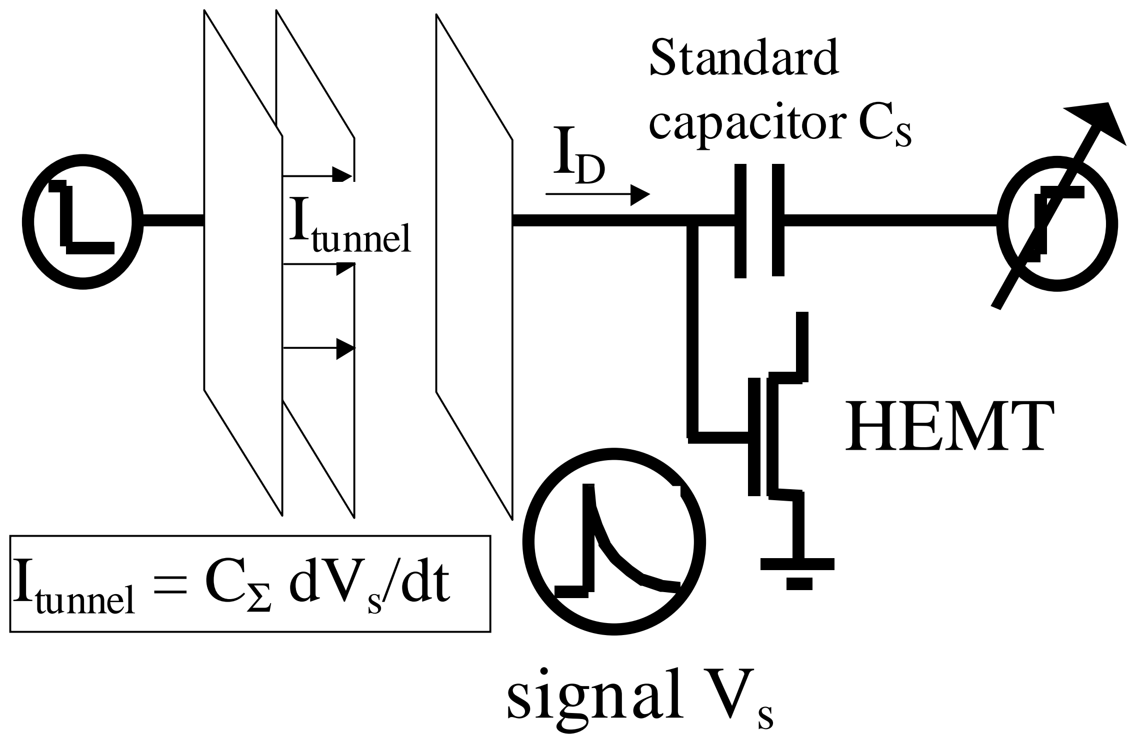

Figure 2-5: Capacitance bridge measuring the tunneling current.

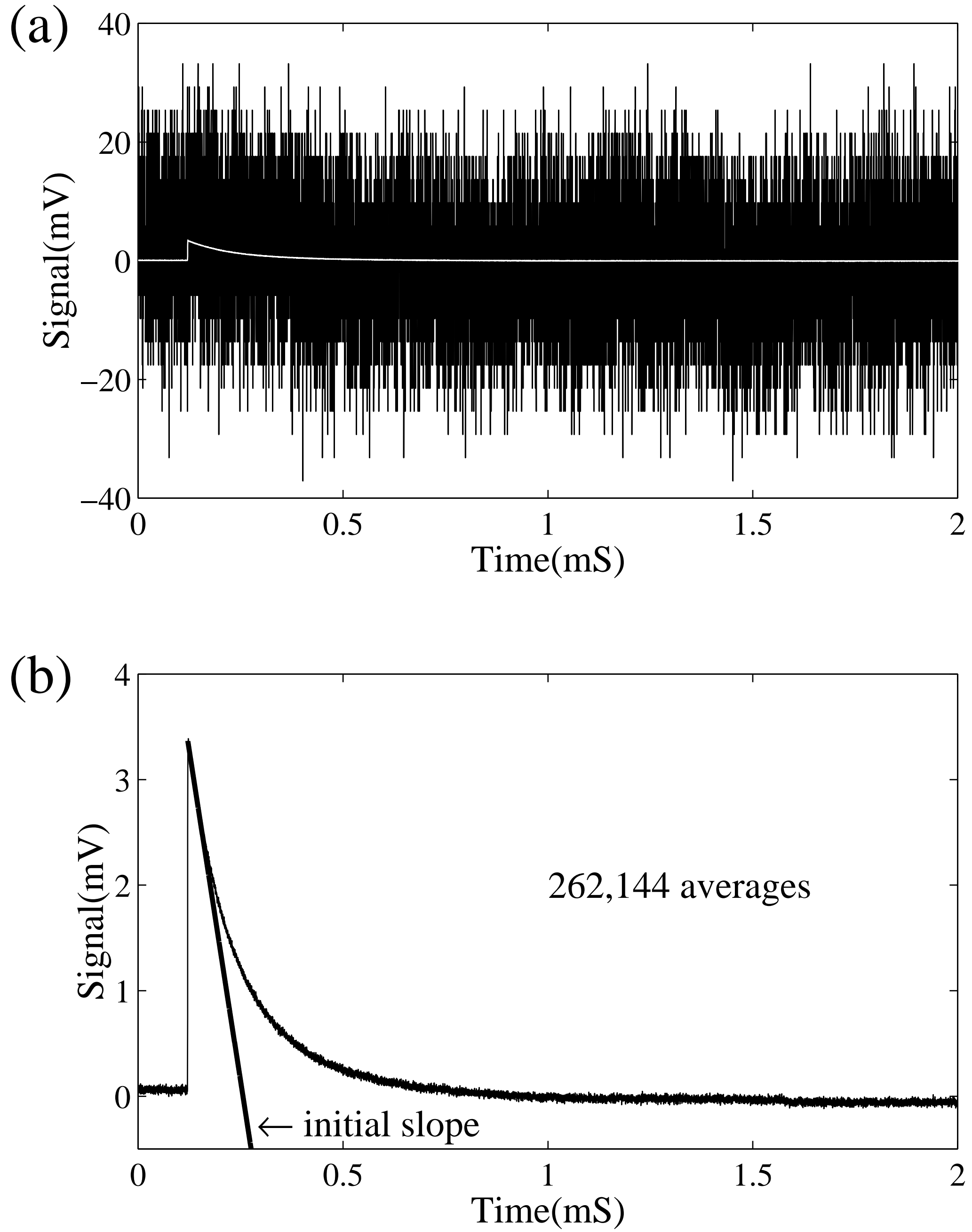

Figure 2-6: (a) The black curve is raw data recorded with no signal averaging when an excitation voltage step of 8 μV is applied only once. The white curve is obtained by repeating the voltage step 262,144 times and averaging the result to recover the signal from noise. (b) The white curve in (a) is re-plotted using a finer voltage scale. We extract the initial slope of the trace to obtain the tunneling current.

Even when electrons tunnel into localized states in the 2D plane, we have no trouble detecting the current because they repel electrons on the top plate. We call our technique "Time Domain Capacitance Spectroscopy" since we measure the electron tunneling process in real time and we set up the voltage across the tunnel barrier capacitively.

2.3.3 Data averaging

One of the main difficulties of this experiment is that it is a broad band measurement and we are susceptible to many types of noise. In most cases the signals are very small. The black curve in Fig. 2-6a shows the signal obtained if one applies a voltage step to the sample once and record the response using an oscilloscope. All the tunneling signal is buried in noise. To recover the signal, it is necessary to repeat pulsing the sample with voltage steps and average the time responses. After averaging 262,144 times, we recover the tunneling signal that we are interested in. We show the averaged trace as the white curve in Fig. 2-6 and plot the same trace using different vertical scale in Fig. 2-6b. We then extract the initial slope of the averaged trace to obtain the tunneling current.

Ordinary oscilloscopes do not have the data throughput to recover the signal from noise. After digitizing one trace, a typical oscilloscope needs 10 ms to 100ms to reset before it is ready for another trigger to digitize a new trace. Depending on the tunneling rate of electrons, our pulse width can be as short as 200 μs. If we use an ordinary oscilloscope for digitization, we will spend most of our time waiting for the oscilloscope to reset after each trace. Therefore we have to use a special signal averager (EG&G model 9826) in place of oscilloscopes to improve the efficiency of data acquisition.

The 9826 signal averager plugs into two adjacent ISA slots on a personal computer. It is capable of adding a new 8 bit digitization of the input signal to a 16 bit sum every 2 ns and will accept a new trigger within 600 ns of completion of the preceding sweep. It is thus possible to signal average more than 1000 times faster than conventional oscilloscopes. After the summation of 256 sweeps by the averager, the sum is then

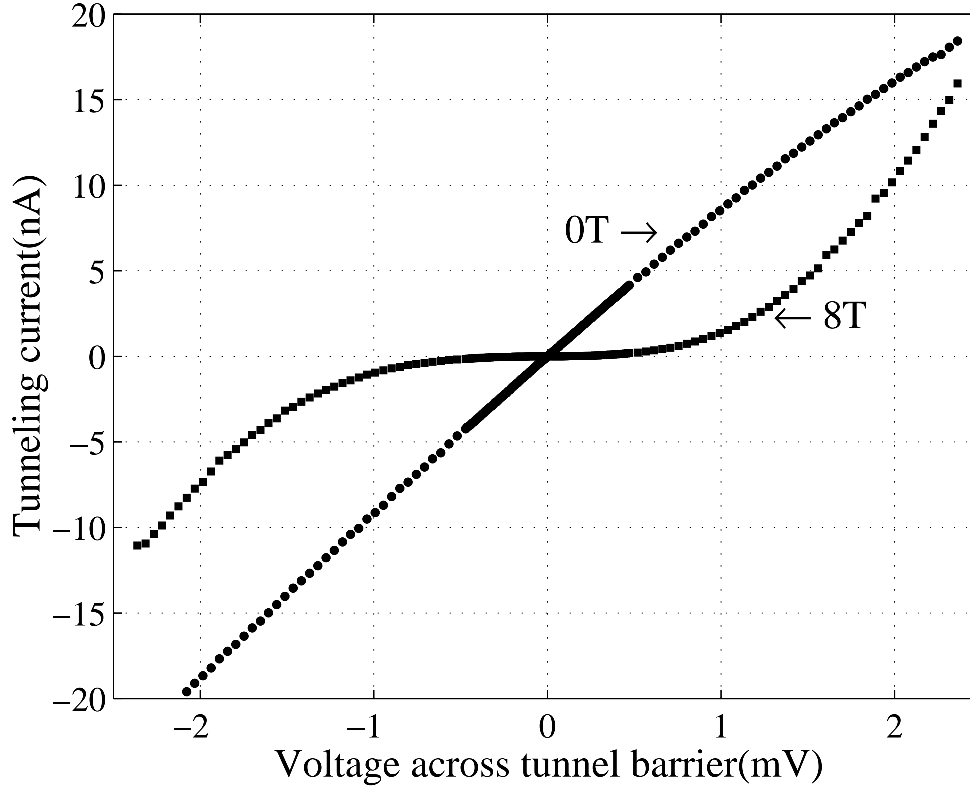

Figure 2-7: I-V characteristics for tunneling into the 2DEG at a density of $1.9 \times 10^{11} cm^{-2}$ and at a temperature of 25mK for B = 0T (circles)and B = 8T (squares).

transferred to the on-board buffer memory. Data in the buffer memory can be read into computer memory without interrupting the acquisition of a new averaged trace. Additional averaging is then performed by software to sum the traces in computer memory.

In Appendix B, we describe a "dithering" technique that increases the voltage resolution of the averager from 8 bits to 16 bits. Both the signal averager and the dithering scheme are crucial components of this experiment. We would not have been able to obtain the data in this thesis without them.

2.3.4 Typical I-V curves

Figure 2-7 shows typical I-V curves that we obtained. To obtain one point on an IV curve we apply voltage steps of certain amplitude many times and average the signal until we can extract its initial time derivative accurately. To get another point

on this IV curve, we need to apply a voltage step of different amplitude and repeat this process. We emphasize these are I-V curves obtained without making electrical contacts to the system we are studying.

At 0T, the I-V curve is linear or ohmic around zero-bias. When we increase the magnetic field to 8T, the tunneling current is clearly suppressed at small voltages compared to the zero field value. The I-V characteristic becomes non-linear. This deviation from ohmic behavior is due to the development of a gap at the chemical potential in the single-particle density of states created by electron-electron interactions in a magnetic field. We will describe a detailed study of this tunneling gap using TDCS in Chapter 4.

2.4 Schematic of Setup

In the last section, we described the basic concepts of TDCS. We will look at some technical details of TDCS in this section. Figure 2-8 shows the essential elements of the computer- controlled capacitance bridge. The electrical components inside the small dotted box are equivalent circuit elements representing the sample, as discussed in section 2.2 and Fig. 2-3. The double channel waveform generator applies voltage steps of opposite polarity to the top electrode of the sample and to one plate of the standard capacitor C_S. The other plate of C_S and the bottom electrode of the sample are electrically connected and the voltage V_b at this balance point b is fed into the gate of a high electron mobility transistor (HEMT). Through a 180 MΩ resistor R_{bias}, we establish the DC bias of the HEMT. This DC bias is kept constant throughout the measurement. We chose such a large resistance so that the RC time at the input of the HEMT is longer than the RC time for tunneling in our samples. Components inside the large dotted box, including the sample, C_S, the HEMT and R_{bias}, are placed within 1 cm of one another. The purpose is to reduce the stray capacitance at the HEMT input, as well as minimize 'ringing' in the circuit due to the sharp voltage steps we applied. During measurement, the components in the large dotted box are cooled to the base temperature of ∼50 mK in the mixing chamber of our cryostat.

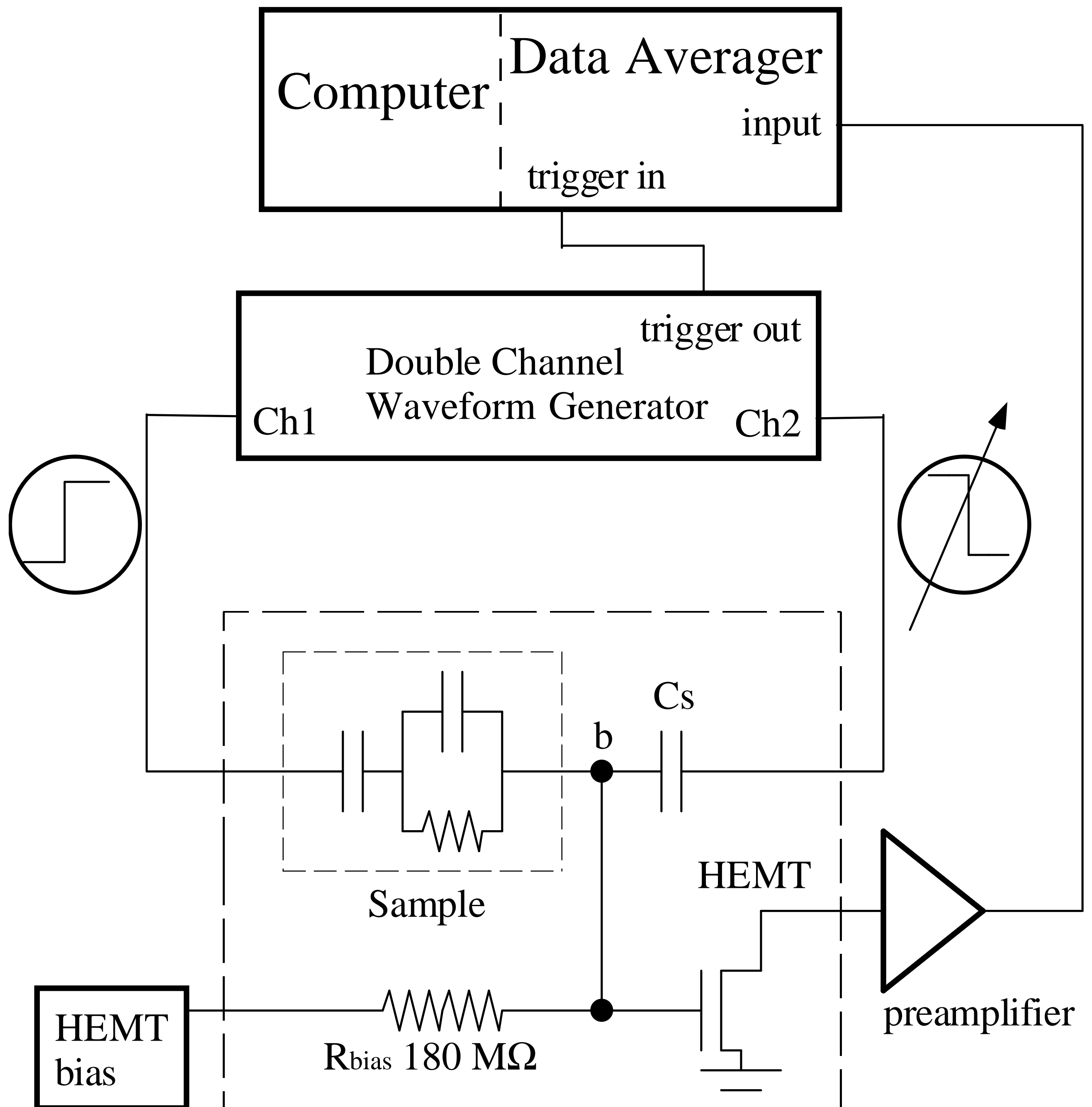

Figure 2-8: Basic schematic of computerized capacitance bridge. The electrical components inside the small dotted box represent the sample. The components inside the large dotted box are placed on the cryogenic probe together with the sample and are cooled to the base temperature of the dilution refrigerator during measurement.

A preamplifier located outside the cryostat further amplifies the output signal from the HEMT. We then record the preamplifier output using the signal averager mounted inside the computer. The signal averager is synchronized to the double channel waveform generator, which provides voltage steps of opposite polarity at precisely the same instant (within 1 ns) to the top electrode of the sample and the other plate of C_S. In section 2.4.1 we will describe the individual components of the double channel waveform generator. For each data point on an I-V curve, the computer sets the appropriate pulse amplitude of voltage excitation on both channels of the pulse generator. The averager records the corresponding tunneling signal from the sample. We then extract the initial slope of the time trace to deduce the current. For another point on the I-V curve, the computer sets the amplitude of voltage excitation to a different value and repeats the process.

2.4.1 Pulse Sequence

So far we considered the excitation voltage applied to the sample as sharp voltage steps. In practice, we apply a sequence of pulses repetitively to the sample. Figures 2-9a and b display a single period of the two pulse sequences of opposite polarity applied to the standard capacitor C_S and the sample respectively. Each period of excitation consists of four voltage steps. For $t < t_1$, the sample is at a specific density N_o set by the DC bias, with the 2DEG in equilibrium with the 3D electrode. At $t = t_1$, we apply the first voltage step. For $t_1 < t < t_2$, electrons tunnel into the 2D system, leading to a voltage change at the input of the transistor, as we described in sections 2.3.1 and 2.3.2. Figure 2-9d shows the response recorded by the data averager.

Immediately before $t = t_2$, the density of the 2DEG is higher than the original density N_o because additional electrons have tunneled into the 2DEG. The amount of deviation depends on the amplitude of the voltage step V_{sample} as well as the thermodynamic density of states on the 2DEG. At time $t = t_2$, we apply a second voltage step of opposite polarity to the first voltage. As a result, electrons tunnel out of the 2DEG back to the 3D electrode. The purpose of the second voltage step is to reset the 2D electron density back to N_o. At $t = t_3$ we apply the third voltage step

which induces electron to tunnel out of the 2DEG at the original density N_o. Similar to the voltage step at $t = t_2$, the voltage pulse at $t = t_4$ resets the 2DEG back to the original density N_o. We repeat this pulse sequence to recover the tunneling signal from noise through signal averaging, and then extract the initial time derivative of the signal at $t = t_1$ and $t = t_3$ to obtain the tunneling current.

2.4.2 Measuring Low Frequency Capacitance by Balancing the Bridge

In this subsection, we describe how we balance the capacitance bridge to obtain the low frequency capacitance of the sample using TDCS.

One of the reasons that we apply voltage steps of opposite polarities to the sample and standard capacitor C_S is to compensate for signals that are not related to tunneling. Figures 2-9c and d show an unbalanced trace and a balanced one respectively. For the unbalanced trace, the signal voltage decays to a non-zero value V_{offset} even after the tunneling process has completed. Balancing refers to the process of setting V_{offset} to zero by tuning the amplitude of the voltage step ($V_{standard}$) applied to C_S. Through balancing, the voltage range of the signal in fig. 2-9c is clearly reduced compared to fig. 2-9d. This allows us to operate the averager at a higher sensitivity.

The second reason for balancing the bridge is to extract the low frequency capacitance C_{low} of the sample. At a time $t >> \tau$ (where τ is the tunneling relaxation time) after application of the voltage step, the 2DEG has come into equilibrium with the 3D electrode. By adjusting the amplitude $V_{standard}$ while keeping V_{sample} fixed, we can null the voltage at the balance point b of the capacitance bridge for long time scales $t >> \tau$ when the tunneling process has completed:

$$\begin{aligned} C_S V_{standard} &= C_{low} V_{sample} \\ C_{low} &= \frac{V_{standard}}{V_{sample}} C_S \end{aligned} \quad (2.3)$$

Equation 2.3 follows simply from considering the sample and C_S as DC voltage di-

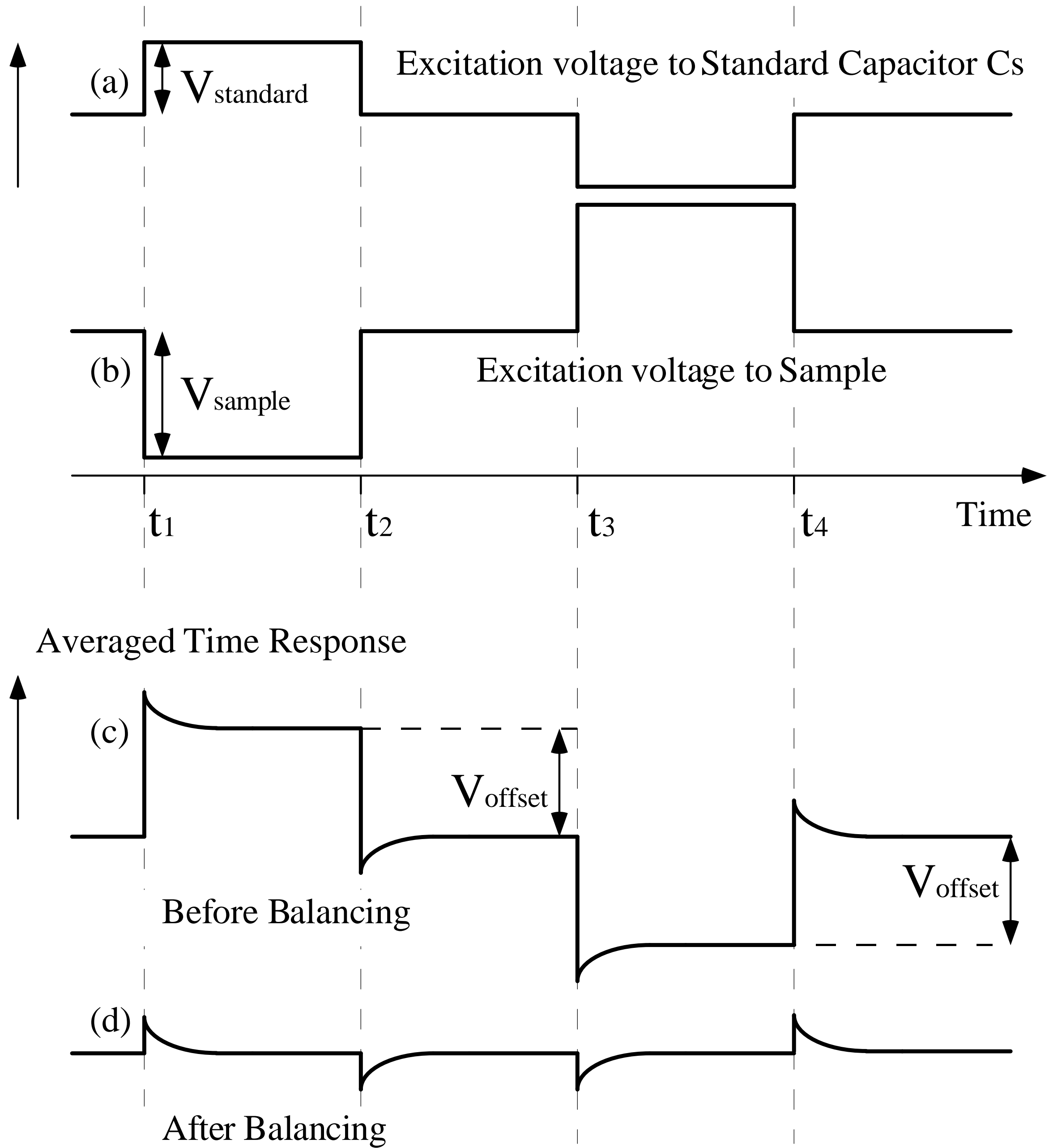

Figure 2-9: This figure shows excitation voltage of opposite polarity applied to (a) the standard capacitor and (b) the sample during one cycle of TDCS measurement. Electrons tunnel into and out of the sample respectively during the first and third pulses. The second and fourth pulses resets the 2D electron density to the initial value. In (c) we show a typical unbalanced recorded sweep. We balance the bridge by adjusting the step amplitude $V_{standard}$ to obtain the sweep in (d).

viders of the total voltage $V_{sample} + V_{standard}$ across them for $t >> \tau$. Hence we can deduce C_{low} directly from $V_{standard}$ required for balancing. The appropriate $V_{standard}$ is determined by the computer and the algorithm for achieving balance is similar to the one in Ref. [7] for balancing a computer controlled AC capacitance bridge.

Ashoori [7] calculated the relationship between C_{low} and the thermodynamic density of states (DOS) at the chemical potential of 2DEG. The essential physical picture is as follows. When the DOS of the 2DEG is zero, no electrons tunnel into the 2DEG when the voltage step is applied. In this limit, C_{low} is simply the geometric capacitance $\kappa A/(x_w + x_g)$ between the top and bottom electrode, where A is the area of the sample and κ is the dielectric constant of GaAs. In the other extreme case when the DOS of the 2DEG is infinite, the 2DEG completely screens the voltage step (for $t >> \tau$). In this case C_{low} equals the geometric capacitance $\kappa A/x_w$ between the top electrode and the quantum well.

Figure 2.10 shows C_{low} for one of our samples in a magnetic field of 3T. At the lowest gate biases (below 0V) the quantum well is completely depleted of electrons. We measure the capacitance $\kappa A/(x_w + x_g)$ between the top electrode and the bottom 3D substrate. As we increase the gate bias, electrons accumulate in the quantum well and there is a sharp rise in C_{low}. The rise in C_{low} occurs because electrons move closer to the top electrode. We now measure the capacitance $\kappa A/x_g$ between the quantum well and the top electrode. Beyond this step, the 2D electron density increases with sample bias and C_{low} displays minima corresponding to the development of the cyclotron gap between Landau levels where the thermodynamic DOS drops significantly.

Measurement of the low frequency capacitance C_{low} is important for characterizing our samples. It allows accurate determination of the density and the filling factor of our samples in a magnetic field.

2.4.3 Fitting Procedure

This section describes our fitting procedure to extract the tunneling current from the initial slope of a time trace. When the tunneling resistance R_{tunnel} is independent

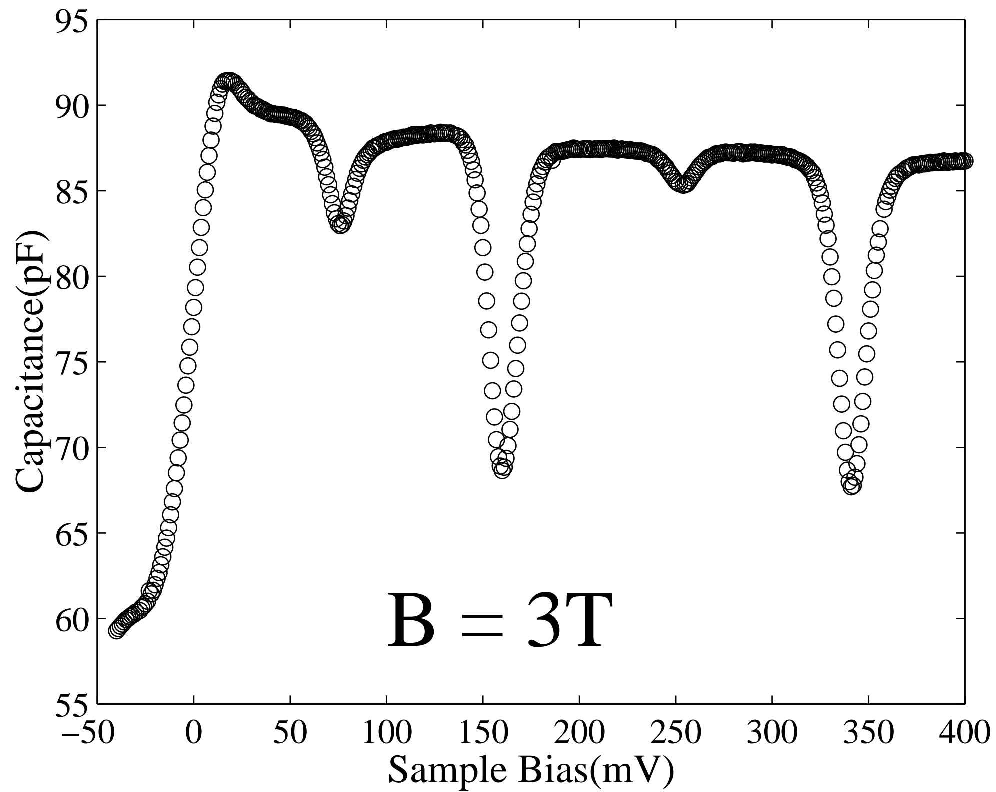

Figure 2-10: This figure plots the low frequency capacitance as a function of sample bias. Electrons start to accumulate in the quantum well at about 0 mV. When the chemical potential of the 2DEG falls between two Landau levels, C_{low} develops minima. The first minimum at 75 mV occurs when the first Landau level is filled with electrons of one spin direction. The second minimum at 160 mV occurs when the first Landau level is filled with electrons of both spin directions.

of voltage across it and behaves as a linear circuit element (for instance, in the zero magnetic field I-V curve in Fig. 2-7), the time trace is a pure exponential decay. However, we do not take the initial slope of the time trace directly. Instead we first subtract the baseline voltage so that the time trace decays to zero at long time scales. We then take the logarithm of the time trace. Figures 2-11a and b show a trace in linear and logarithmic voltage scale when R_{tunnel} is independent of voltage. The initial time derivative of the time trace is equal to the product of the initial voltage and the initial time derivative of the logarithm of the time trace:

$$\frac{dV}{dt}|_{t=0} = V(t=0)\frac{d\ln V}{dt}\ |_{t=0} \tag{2.4}$$

If the time trace decays exponentially:

$$\frac{dV}{dt}|_{t=0} = -V(t=0)\frac{1}{\tau} \tag{2.5}$$

Here, we define $1/\tau = -d\ln V/dt$ as the relaxation time of the decay. For a voltage-independent R_{tunnel}, τ is also independent of time. In this case, we can obtain the relaxation time by fitting to any part of the time trace. In practice, we deduce that R_{tunnel} is voltage independent if the relaxation time is constant.

Figures 2-11c and d show the drastically different time traces for a voltage dependent R_{tunnel} when a magnetic field of 4T suppresses tunneling at small excitation voltages. The relaxation rate $1/\tau$ decreases with time and we must use the initial relaxation rate to obtain the tunneling current. Typically we extract the relaxation rate when the time trace decays to a voltage between 96% and 86% of its initial value.

2.4.4 Summary

In this Chapter, we described the concept and some technical details of "time domain capacitance spectroscopy" (TDCS). TDCS measures the complete tunneling I-V characteristics into mesoscopic semiconductor systems such as 2DEG or quantum dots without making ohmic contacts to them. In the following chapters, we will use

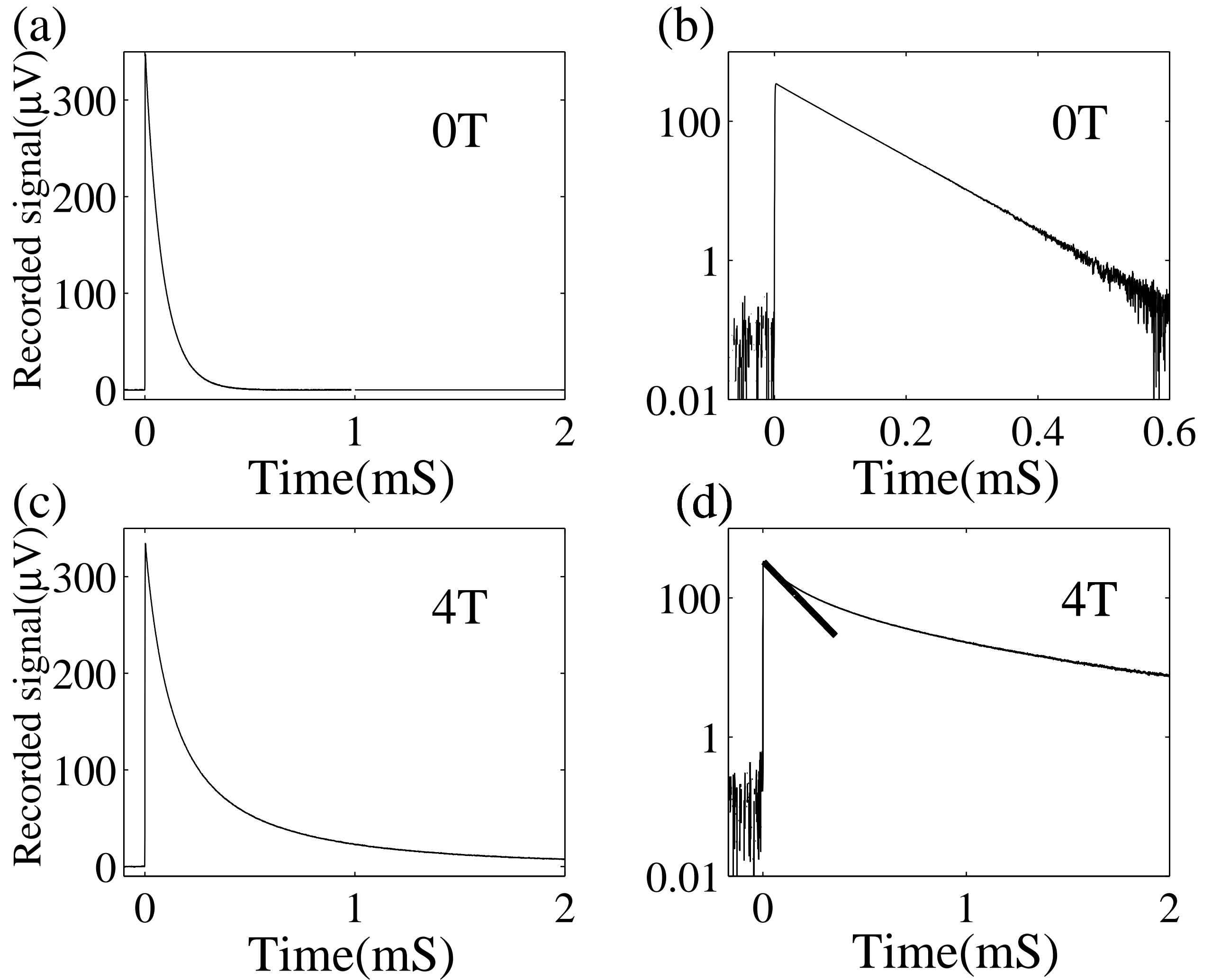

Figure 2-11: (a) Typical signal at the input of the HEMT at $B = 0T$, using 3.3 mV voltage steps. (b) Same signal in (a) plotted on a semi-log scale, demonstrating the pure exponential decay when the tunneling resistance is voltage-independent. (c) Signal at $B = 4T$ for a voltage dependent tunneling resistance. (d) Same signal in (c) plotted on a semi-log scale. The relaxation rate decreases as the signal decays. Note that the time scale is different from the plot in (b). The thick straight line is a linear fit to the initial part of the decay.

TDCS to measure tunneling into a 2DEG in various regimes.

Chapter 3

Zero-bias Coulomb Anomaly for Tunneling into disordered 2D Electronic Systems

In this Chapter, we use tunneling spectroscopy to study the effects of electron-electron interactions on the single-particle density of states (DOS) of a disordered 2D electron system.

For non-interacting electrons in a disorder-free 2D system, the wavefunctions are plane waves and the DOS is a constant function of energy. Even though inclusion of electron-electron correlations by the Fermi-liquid theory may lead to renormalization of the DOS, the DOS nevertheless remains a smooth function of energy and contains no singularities near the Fermi level.

An important assumption of Fermi-liquid theory is the spatial homogeneity of the system. The presence of disorder, such as impurities and defects, leads to scattering of the electrons and has a profound effect on the physical properties of the electronic system. When the degree of disorder is strong so that the Fermi wavelength is comparable to or less than the mean free path l ($k_F l \sim 1$, where k_F is the Fermi wavevector), the wavefunctions change their nature completely and become localized, a phenomenon known as Anderson localization [16]. For localized electrons, the inclusion of long-range Coulomb repulsion results in the Coulomb gap [5]: the vanishing

of the DOS at the Fermi level.

When the disorder is weak such that the mean free path is much larger than the Fermi wavelength, the wave function remains extended and electrons move along classical trajectories between collisions. In order words, electrons diffuse instead of propagate freely as plane waves. The diffusion constant decreases with increasing degree of disorder. As a result an electron stays longer in a certain region in space where it can interact with other electrons. Disorder leads to poorer screening and therefore enhances interaction effects among electrons. Altshuler, Aronov and Lee [6] treated the disordered Fermi liquid problem in 2D by performing a perturbation theory calculation to lowest order in the interaction strength, valid in the limit $k_F l \gg 1$ (or equivalently $E_F \tau \gg \hbar$, where E_F is the Fermi energy and τ is the scattering time). They predicted that interaction effects in a 2D disordered metal lead to the development of a logarithmic singularity in the single-particle DOS $n(E)$ near the Fermi energy:

$$\frac{\delta n(E)}{n(E)} = \frac{\hbar}{2\pi E_F \tau} \log(\frac{E\tau}{\hbar}) \tag{3.1}$$

This singularity in the single particle DOS results in suppression of tunnel conductance $G(V)$ into the 2D system at small voltages [17], a phenomenon commonly known as the zero-bias Coulomb anomaly in tunneling:

$$\frac{G(V) - G(V_o)}{G(V_o)} = \frac{e^2 R}{4\pi^2 \hbar} \log(\frac{V}{V_o}) \log(2k_s d) \tag{3.2}$$

Here, $V_o = \hbar/e\tau$, k_s is inverse screening length, d is the distance between the 2DEG and the source electrode from which electrons tunnel and R is the in-plane resistivity of the 2DEG. The extra log factor arises from screening by the source electrode. Image charges in the source electrode renders the interactions in the 2DEG dipolar at distances larger than d.

Several research groups [8, 9, 10, 11, 12, 13, 14] have performed tunneling measurements of quasi-2D disordered metal and semi-metal films since early 1980's and observed the predicted logarithmic dependence of tunneling conductance with voltage. Although the Coulomb anomaly for tunneling has been thoroughly studied in

metal films, to our knowledge there have not been any experiments demonstrating the logarithmic correction to the DOS in semiconductor 2D systems. The major difficulty in performing tunneling measurements of 2D systems is the requirement that the in-plane conductance must be much higher than the tunneling conductance. In addition to the in-plane conductance problem, in semiconductor 2D systems there is the difficulty of making separate electrical contacts to the 2D system and the source electrode providing the tunneling electrons, as we mentioned in Chapter 2. Eisenstein [15] used a selective gating technique to make separate contacts to two 2DEG's in GaAs. However, in these double quantum well structures, the main feature in the tunneling spectrum is a peak at zero bias due to the requirement of conservation of transverse (in-plane) momentum in tunneling.

Using TDCS that we described in Chapter 2, we measure tunneling from a 3D substrate to a 2DEG in GaAs at arbitrary low in-plane conductance without making an electrical contact to the 2DEG. Transverse momentum conservation for tunneling between the 2DEG and the 3D substrate only produces a smooth variation of the tunneling conductance with voltage [18]. This allows us to perform a comprehensive study of the singular, logarithmic corrections to the tunneling conductance near zero bias. We describe our results in this Chapter.

3.1 Origin of the Logarithmic Correction to the single particle DOS: Qualitative Picture

In this section, we present a qualitative picture for the logarithmic corrections to the single-particle DOS in 2D systems. One can refer to the calculation of the exchange contribution to the self energy by Altshuler, Aronov and Lee [6] for a rigorous derivation.

Consider a particle undergoing diffusion in 2D. There is a finite probability that it returns to the original position $r = 0$. In 2D, the probability that the particle has

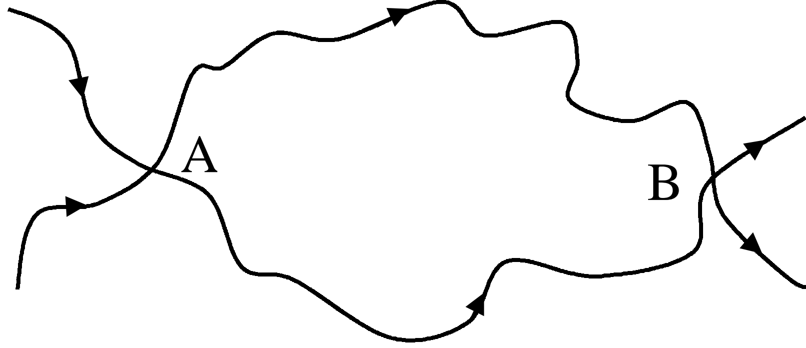

Figure 3-1: Two particles undergoing diffusive motion have a finite probability of a second encounter. This figure shows the trajectories of motion of two particles intersecting at point A and later at point B. If the time for the particles to go from A to B is small compare to the inverse of their energy difference, they will interfere.

traveled a distance r after a time t is:

$$P(r,t) = \frac{1}{4\pi Dt} e^{-r^2/4Dt} \tag{3.3}$$

where D is the diffusion constant. Now consider two particles with energy difference ϵ that interact at point A in Fig. 3-1. Since the particles undergo diffusive motion, there is a finite probability that they may encounter each other again, for instance, at point B in Fig. 3-1. An expression similar to Eq. 3.3 applies to the relative displacement between the two particles. Due to the uncertainty principle, the energy difference ϵ of the two particles cannot be resolved during a time shorter than $\hbar/\epsilon$. For interaction processes occurring within this time interval, the two states essentially have identical energies and will therefore interfere at point B, where their amplitudes instead of intensities add.

For simplicity, let us assume that there is a point-interaction between the two particles, characterized by a coupling constant C. Due to the interference effects, the effective coupling constant C_{eff} differs from the bare constant C by a factor of $(1+\alpha)$:

$$C_{eff} = C(1+\alpha) \tag{3.4}$$

where α is the probability that two particles will encounter each other again. To calculate α, let us consider particles originating from a region with the size comparable to the Fermi wavelength λ_F at the Fermi velocity v_F. The number of particles leaving the region in time interval dt is $N\lambda_F v_F dt$, where N is the density of particles in 2D. At a particular instant of time t, a fraction of these particles, proportional to $P(r=0,t)$, will encounter each other again. We obtain α by integrating this probability over time:

$$\alpha = \int_{\tau}^{\hbar/\epsilon} P(r=0,t)\lambda_F v_F dt \tag{3.5}$$

$$= \int_{\tau}^{\hbar/\epsilon} \frac{\lambda_F v_F}{4\pi D t} dt \tag{3.6}$$

$$\sim \frac{h}{2E_f\tau} \log \frac{\hbar}{\epsilon\tau} \tag{3.7}$$

where E_f is the Fermi energy of the 2D system. We obtain Eq. 3.7 from Eq. 3.6 using the following relations:

$$D = \frac{v_F^2 \tau}{2} = \frac{E_F \tau}{m_{eff}} \tag{3.8}$$

$$m_{eff} v_F = \frac{h}{\lambda_F} \tag{3.9}$$

where m_{eff} is the effective mass of electrons. The upper and lower limits of integration in Eq. 3.5 require some explanation. In Eq. 3.5, the lower limit of integration is the scattering time τ during which each particle on average scatters once. For time intervals shorter than τ, the particles undergo ballistic motion instead of diffusion so that Eq. 3.3 does not apply. They have a very small probability of interfering in a second encounter because on average each particle is scattered less than once. The upper limit $\hbar/\epsilon$ is the time interval during which the two electronic states have indistinguishable energies so they will contribute to the interference correction. Assuming that relative corrections to all physical quantities are proportional to α, we find that the corrections to the single-particle density of states take a logarithmic form in 2D:

$$\frac{\delta n}{n} \propto \frac{\hbar}{E_F \tau} \log \frac{\epsilon\tau}{\hbar} \tag{3.10}$$

We emphasize that the above picture is only a qualitative description intended to

give the readers some intuition on the logarithmic energy dependence in the single-particle DOS. Nevertheless it highlights the importance of the quantum mechanical nature of the electronic states in determining the physical properties of a diffusive system.

3.2 Samples

In Chapter 2, we described time domain capacitance spectroscopy (TDCS). TDCS enables us to measure the tunneling current into a 2DEG at arbitrary low in-plane conductance. We are able to measure, for the first time, the contribution of localized states to the tunneling current. Furthermore, TDCS measures the complete tunneling current-voltage characteristics without making an ohmic contact to the 2DEG.

Figure 3-2 shows the essential structure of samples used in TDCS measurement. The samples are GaAs/AlGaAs heterostructures grown by molecular beam epitaxy. In this chapter, we present data from two samples: sample A and sample m060296a. The substrate is n+ doped GaAs for both samples. First, we grow a GaAs spacer layer on top of the substrate. Then we grow an AlGaAs tunnel barrier, followed by a GaAs quantum well, which defines the 2D system. The AlGaAs blocking barrier is thick and prevents conduction between the 2D system and the GaAs top electrode. We introduce dopants in the AlGaAs to provide electrons for the quantum well. The AlGaAs regions in both samples have 30% aluminum concentration.

Sample A was grown by S. Wright and has been studied extensively using AC capacitance techniques [7, 19, 20, 21]. The concentration of silicon dopants in the degenerately n-doped substrate is $1 \times 10^{17} cm^{-3}$. The thickness of the layers, from bottom to top, are as follows: 30 $\AA$ GaAs undoped spacer, 160 $\AA$ AlGaAs undoped tunnel barrier, 150 $\AA$ GaAs undoped quantum well, 1550 $\AA$ AlGaAs blocking barrier and a degenerately n doped GaAs cap layer. In the AlGaAs blocking barrier, dopants are introduced in the region from 100 $\AA$ to 200 $\AA$ away from its lower boundary to provide electrons for the quantum well. A gold-germanium ohmic contact to the GaAs cap layer allows variation of 2D electron density from depletion to $6 \times 10^{11} cm^{-2}$. The

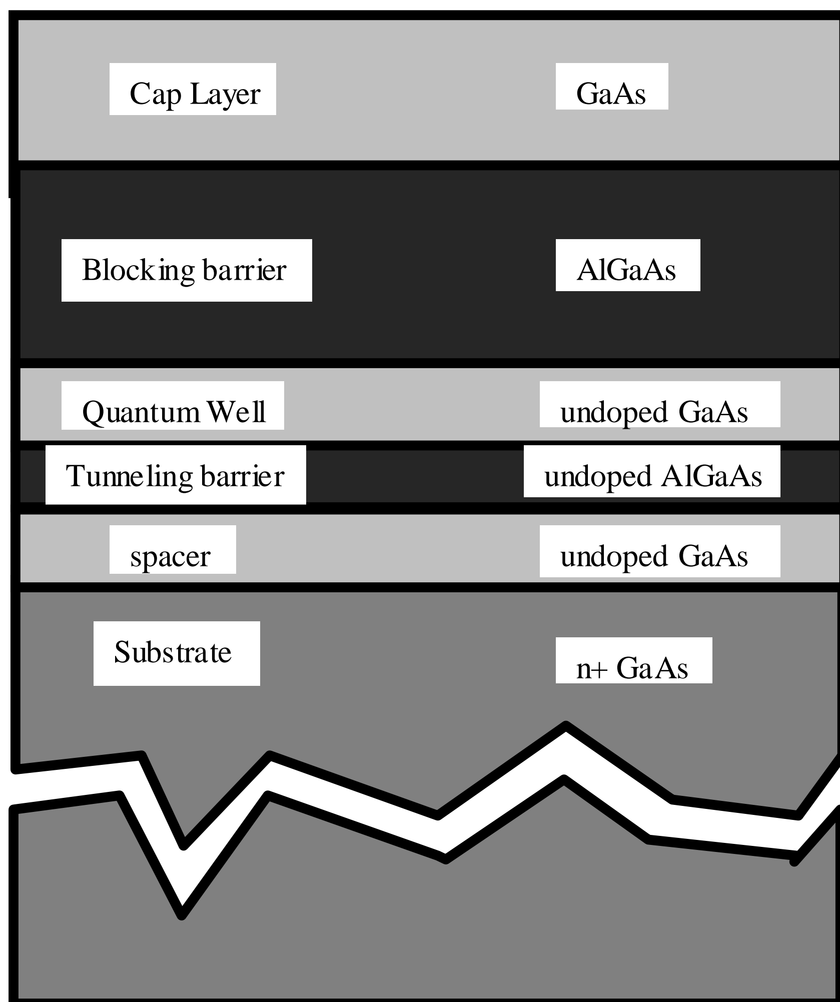

Figure 3-2: The essential layer structure of the samples.

circular mesa has a diameter of 400 μm.

Sample m060296A was grown by Prof. M. L. Melloch at Purdue University. The substrate has silicon dopant concentration of $5 \times 10^{17} cm^{-3}$. The thickness of the layers, from bottom to top, are as follows: 50 $\mathring{A}$ GaAs undoped spacer, 143 $\mathring{A}$ AlGaAs undoped tunnel barrier, 150 $\mathring{A}$ GaAs undoped quantum well, 550 $\mathring{A}$ AlGaAs blocking barrier and a 50 $\mathring{A}$ undoped GaAs cap layer. In the AlGaAs blocking barrier, dopants at a concentration of $5 \times 10^{17} cm^{-3}$ are introduced in the region from 200 $\mathring{A}$ to 350 $\mathring{A}$ away from its lower boundary to provide electrons for the quantum well. A chromium gold Schottky contact to the GaAs cap layer allows variation of 2D electron density from depletion to $3 \times 10^{11} cm^{-2}$. The circular mesa has a diameter of 300 μm.

Appendix C describes the fabrication process for the samples.

3.3 Experimental Result

In this section we describe our observation of the Coulomb anomaly for tunneling into a 2DEG in GaAs, measured with TDCS that we described in Chapter 2.

Figure 3-3 shows the tunneling conductance as a function of voltage for sample A. Through a DC bias applied to the top electrode, we change the density in the 2DEG by repelling or attracting electrons into the quantum well. The electron densities are determined by measuring the sample capacitance at low frequencies in a perpendicular magnetic field, as described in section 2.4.2 and Fig. 2-10. Minima in the capacitance develop when an integer number of Landau levels are filled with electrons. Since the degeneracy of the Landau levels is a known quantity, we can deduce the electron density in the 2D system by locating the sample bias at which the capacitance minima occur. We sweep the magnetic field back to 0T for the tunneling conductance measurement in Fig. 3-3. Unless otherwise specified, the magnetic field is maintained at 0T for data presented in this chapter.

In Fig. 3-3, the density for each successive curve from the top decreases by $1.5 \times 10^{10} cm^{-2}$. Around zero bias, there is clear suppression of tunneling conductance. This suppression becomes stronger as the electron density is decreased.

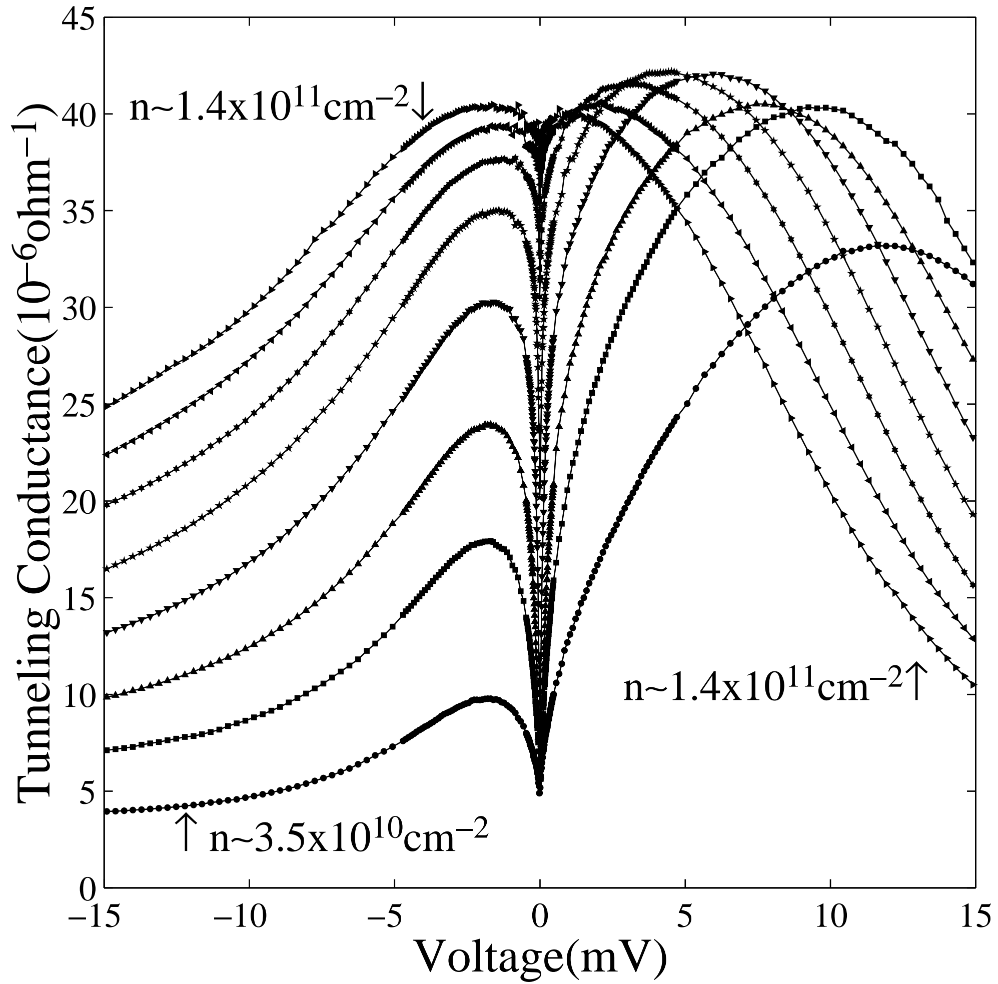

Figure 3-3: Tunneling conductance vs. voltage for different electron densities in sample A at a temperature of 30 mK. The electron density decreases by $1.5 \times 10^{10} cm^{-2}$ for each successive curve from the top. There is clear suppression of tunneling conductance at small voltages.

3.3.1 Explanation of the Asymmetry in the Conductance Curves

Before we proceed to demonstrate that the tunneling conductance suppression is logarithmic in voltage as predicted by theory of electron-electron interactions in disordered 2D systems, let us explain the features at large energies, namely the asymmetry of the conductance curves. For all densities shown in Fig. 3-3, the tunneling conductance decreases at large negative voltages ($< -3mV$). In a perfectly clean 2D system, the thermodynamic DOS is constant as a function of energy. In the presence of disorder, the thermodynamic DOS decreases gradually to zero rather than drops abruptly, forming a "band tail". This deviation of thermodynamic DOS from the constant value corresponds to electrons forming isolated islands in the disordered 2D system at low densities, decreasing the effective occupation area of the quantum well by electrons. The decrease in tunneling conductance at negative voltages simply reflects the "band tail" in a disordered 2DEG.

At large positive voltages, the tunneling conductance again decreases for a different reason. This decrease in tunneling conductance starts at lower voltages for data taken at higher densities. We account for this decrease by transverse momentum conversation for tunneling between the 2DEG and 3D electrode that was studied in detail by Lebens [18]. Consider the two systems in momentum space, where tunneling occurs between a 2D Fermi disk and a 3D Fermi sphere, with Fermi wavevectors k_{2D} and k_{3D} respectively. In our experiment, k_{3D} remains constant while k_{2D} increases as the voltage applied at the top electrode attracts electrons into the quantum well. When $k_{3D} > k_{2D}$ (Fig. 3-4a), there are states on the 3D Fermi sphere from which electrons can tunnel into the 2DEG while conserving both energy and transverse (perpendicular to the direction of tunneling) momentum. On the other hand, when the 2D electron density increases so that the 2D Fermi disk is larger than the 3D Fermi sphere (Fig. 3-4b), tunneling cannot take place if we require both conservation of energy and transverse momentum. In the presence of disorder which gives rise to scattering, such tunneling events can occur, albeit with a reduced probability, leading

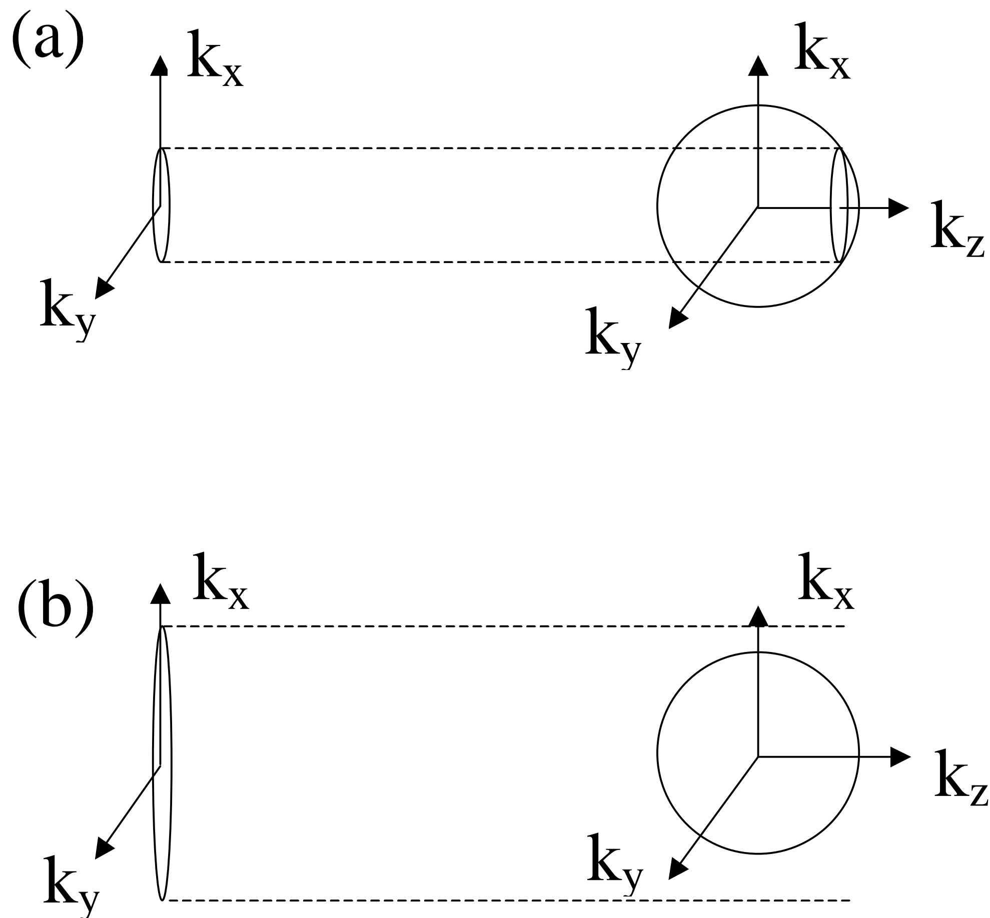

Figure 3-4: (a) When $k_{2D} < k_{3D}$, there are available states on the Fermi sphere with the same transverse wavevector as the states on the edge of the Fermi disk. (b) When $k_{2D} < k_{3D}$, there are no states on the Fermi sphere with identical transverse wavevector as the states on the edge of the Fermi disk. Tunneling cannot take place if we require both conservation of energy and transverse momentum.

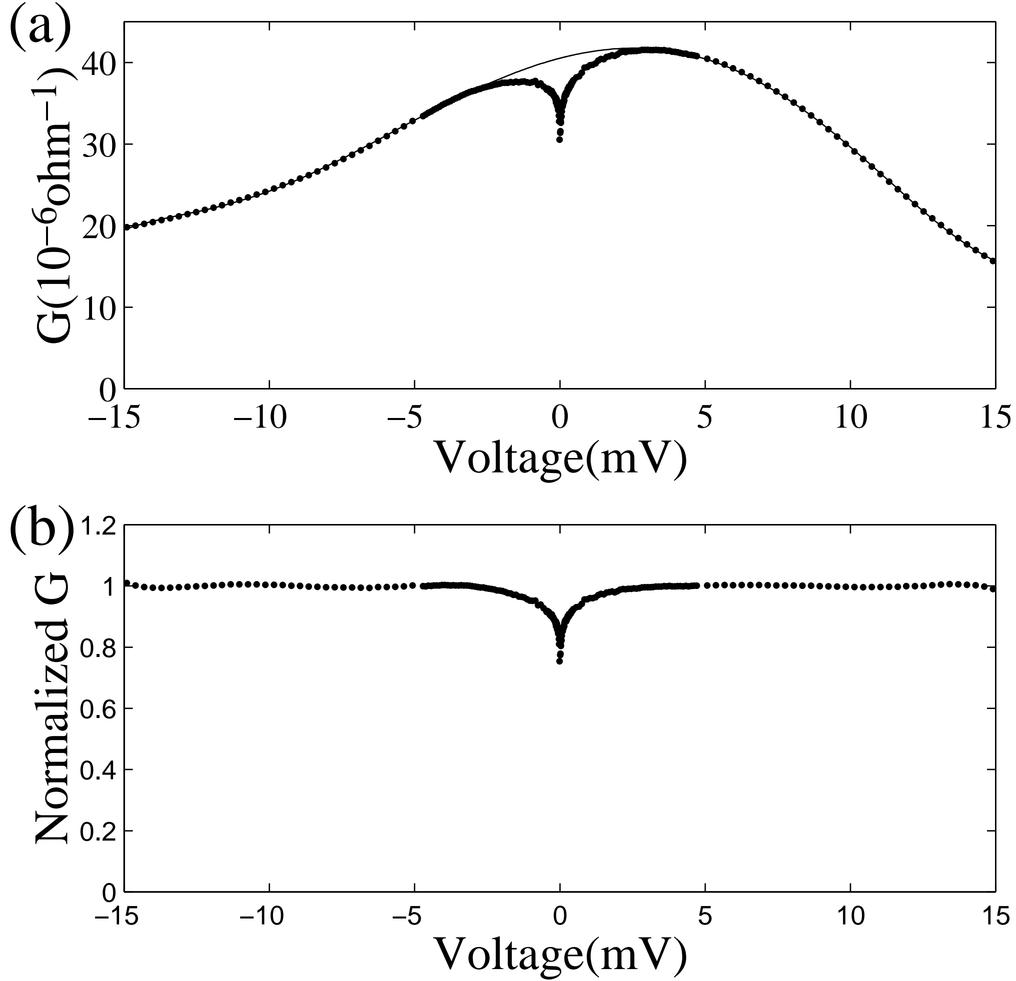

Figure 3-5: (a) The circles are tunneling conductance vs. voltage at $N = 1.12 \times 10^{11} cm^{-2}$. The line is an 8th order polynomial fit to data points at voltages $|V| > 3mV$. (b) Normalized conductance obtained by dividing the data points in (a) by the polynomial fit.

to the decrease in tunneling conductance at larger positive voltages.

3.3.2 Normalization Procedure and Logarithmic DOS Correction

In order to compare the suppression of tunneling near zero bias for different conductance curves, we need to eliminate the background conductance variations at large voltages. We do this by fitting a high order polynomial to the conductance data in Fig. 3-3 for voltages $|V| > 3mV$ where the tunneling suppression is negligible,

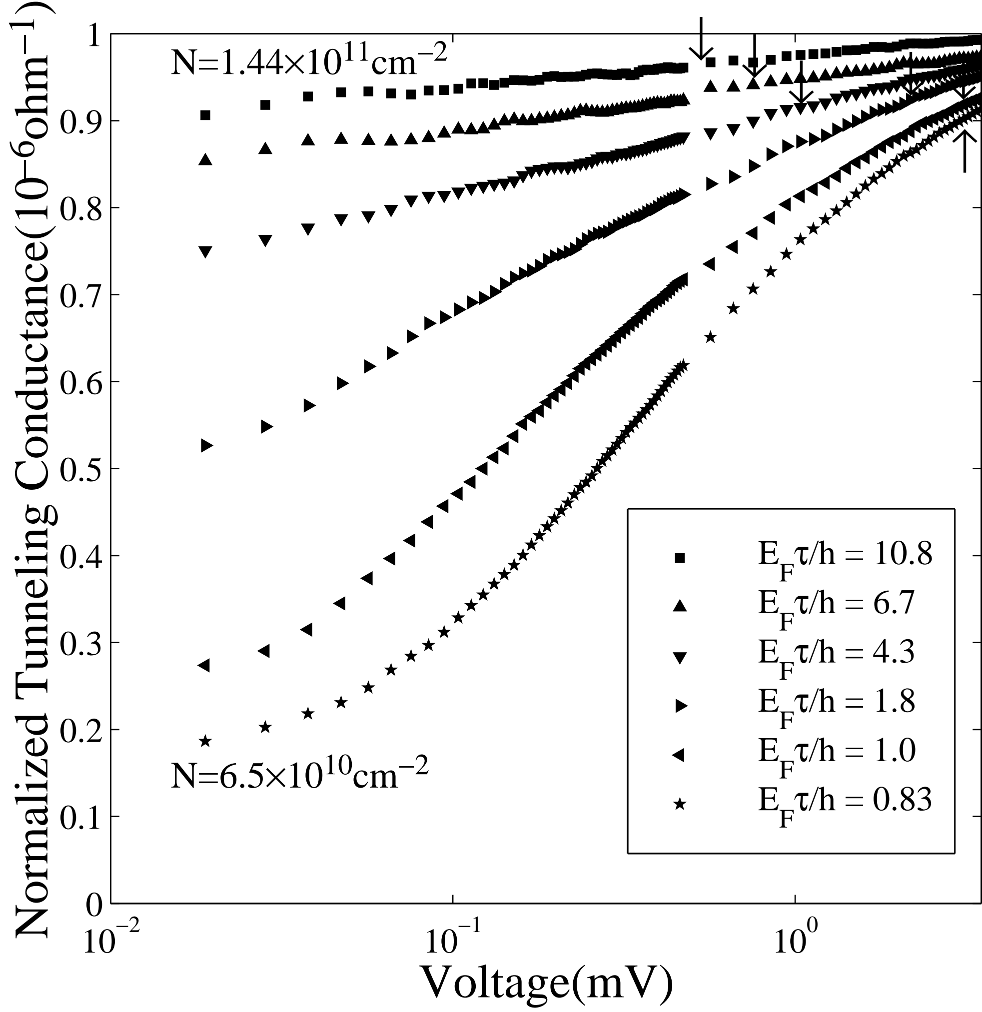

Figure 3-6: Normalized tunneling conductance vs. voltage on a logarithmic horizontal scale. The electron density decreases by $1.5 \times 10^{10} cm^{-2}$ for each successive curve from the top. The arrows indicate the voltage $V_o = \hbar/e\tau$ corresponding to the inverse scattering time for each density.

as shown in Fig. 3-5a. Since the Coulomb anomaly is a fractional correction to the conductance (Eq. 3.2), we divide the data points by the polynomial fit to obtain the normalized conductance displayed in Fig. 3-5b.

We carry out a similar procedure for each conductance curve in Fig. 3-3 and plot the normalized tunneling conductance on a semi-log voltage scale in Fig. 3-6. The tunneling conductance varies logarithmically for two decades in voltage as predicted

by the perturbation theory on a disordered Fermi liquid:

$$\frac{G(V)-G(V_o)}{G(V_o)} = \frac{e^2R}{4\pi^2\hbar}\log(\frac{V}{V_o})\log(2k_sd) \quad (3.11)$$

$$= \frac{\hbar}{4\pi E_F\tau}\log(\frac{V}{V_o})\log(2k_sd) \quad (3.12)$$

where $V_o = \hbar/e\tau$ corresponds to the inverse scattering time, while k_s is the inverse screening length:

$$k_s = \frac{2\pi e^2}{\kappa}\frac{dN}{d\mu} \quad (3.13)$$

Here κ is the dielectric constant for GaAs. In Eq. 3.12, the factor $\log(2k_sd)$ is due to screening from the bottom 3D electrode. For a 2DEG in GaAs the screening length is about 50 $\AA$ assuming the thermodynamic DOS $dN/d\mu$ has a constant value given by $m_{eff}/\pi\hbar^2$. The thickness of the tunnel barrier d is 160 $\AA$ in sample A. Thus the log factor has a value of ~2 in our samples. As we described earlier, the thermodynamic DOS $dN/d\mu$ decreases at low densities near the "band tail." According to Eq. 3.13, the screening length increases correspondingly. For the data in Fig. 3-6, the thermodynamic DOS decreases by about 30% at the lowest density, reducing the log factor in Eq. 3.11 by ~ 20%.

Equation 3.12 follows from Eq. 3.11 using Drude's formula for resistivity:

$$\frac{1}{R} = \frac{Ne^2\tau}{m_{eff}} \quad (3.14)$$

where m_{eff} is the effective mass of electrons in GaAs. As the electron density N decreases, the scattering time τ decreases due to less effective screening of impurities. Since both N and τ decrease, the in-plane resistivity increases and leads to stronger suppression of the tunneling conductance near zero bias.

From the slope of the conductance curves in Fig. 3-6, we extract the in-plane resistivity R using Eq. 3.11 and plot the result in Fig. 3-7a. As expected, the in-plane resistivity decreases with increasing electron density. However, we cannot compare R extracted from the above procedure with R directly measured by transport because there are no direct ohmic contacts to the 2DEG in our samples, as described in

Chapter 2. Nonetheless, previous experiments [8, 9, 10, 11, 12, 13, 14] have shown that the values of R obtained independently from tunneling and transport measurements on the same thin metal film agree very well. We also point out that in our experiment the logarithmic corrections to the tunneling conductance occur in the same range of in-plane resistivity as thin metal films.

Using Drude's result for in-plane resistivity (Eq. 3.14), we calculate the scattering time τ and plot it as a function of electron density in Fig. 3-7b. As we deplete the 2D system of electrons, the scattering time decreases due to the reduced effectiveness of screening. We also mark the corresponding voltage $V_o = \hbar/e\tau$ with arrows in Fig. 3-6 for each tunneling conductance curve. As we mentioned earlier, Eq. 3.12 is the result of a perturbation theory calculation on a disordered Fermi liquid to lowest order in $\hbar/E_F\tau$, valid in the diffusive regime when $\hbar/E_F\tau \ll 1$. The inset of Fig. 3-6 lists this important parameter $E_F\tau/\hbar$ for the conductance curves at different densities. At the lowest density of $6.5 \times 10^{10} cm^{-2}$ in Fig. 3-6, $E_F\tau/\hbar$ becomes smaller than unity and deviations of the tunneling conductance from logarithmic voltage dependence appear. We will return to this limit of low density and high in-plane resistance in section 3.5

3.4 Significance of measuring the Coulomb anomaly in semiconductor 2DEG

Even though there have been extensive studies of the logarithmic Coulomb anomaly in disordered films of metal and semi-metal [8, 9, 10, 11, 12, 13, 14], confirmation of its existence in 2D semiconductor systems is nevertheless important in a number of ways.

3.4.1 GaAs quantum wells define purely 2D systems

First, quantum wells in GaAs heterostructures define purely 2D electronic systems at typical measurement temperatures, in contrast to thin metal films that are quasi-2D. The major difference is in electron density. 2D electron systems in GaAs have much

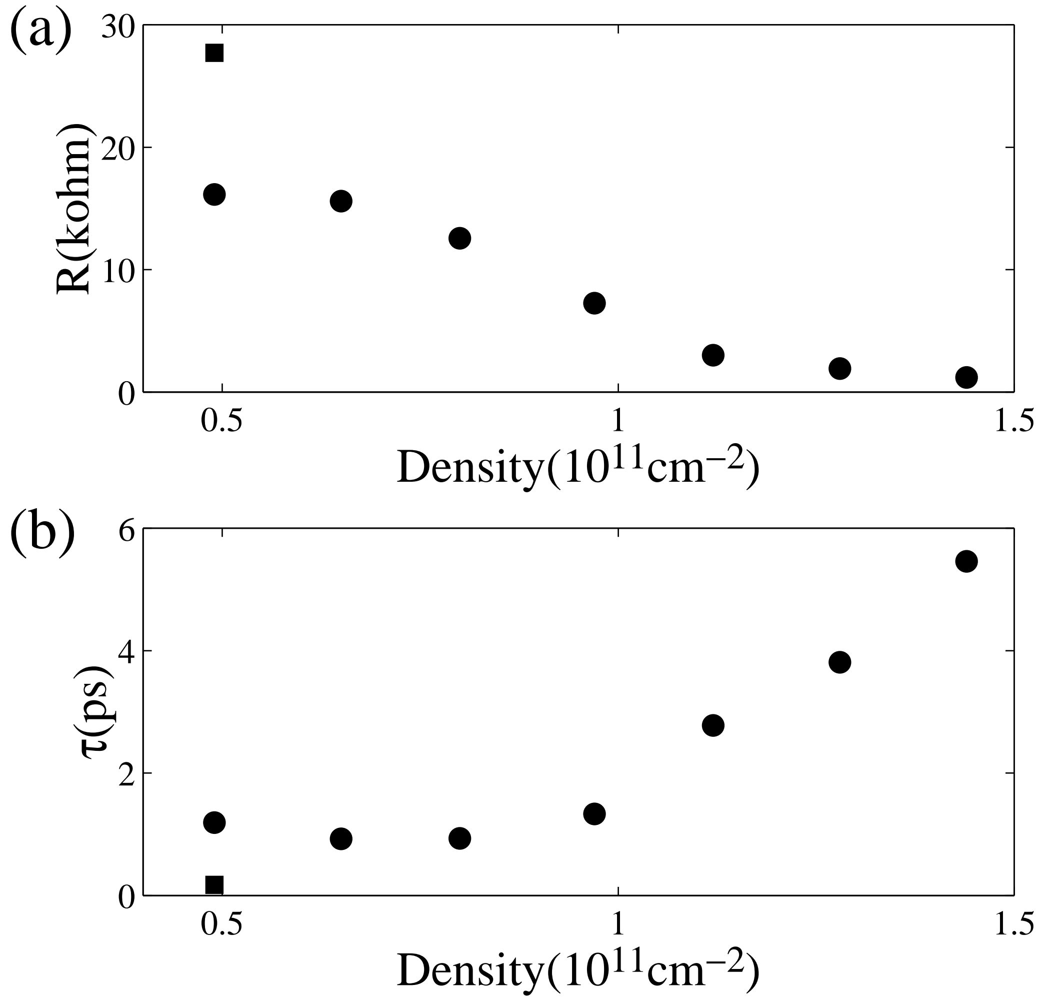

Figure 3-7: (a) in-plane resistivity R and (b) Scattering time τ vs. electron density. The circles are obtained by fitting the tunneling conductance curves with DOS corrections from the perturbation theory (Eq. 3.12). The square corresponds to fitting the conductance curves with a power law using the semi-classical result (Eq. 3.18).

lower densities compared to thin metal films. For a 150 $\AA$ GaAs quantum well, the energy separation between the first and second subband is about 50 meV, while the Fermi energy is only 3.6 meV at typical 2D electron density of $1 \times 10^{11} cm^{-2}$. Since we perform our measurement at a temperature of < 1 K (equivalent to 0.1 meV), we can ignore thermal activation of electrons to the second subband and regard the quantum well as a genuine 2D system. For a metal film of same thickness the electron density is more than a factor of 10,000 higher, leading to multiple subbands filled. Nevertheless, the films are quasi-2D provided one measures tunneling for energies less than $E_c = \hbar D/a^2$, where D is the diffusion constant and a is the film thickness. The reason is that for energies $E < E_c$, the particles diffuse a distance larger than the film thickness a during a time $t > \hbar/E_c$ and experiences the restricted dimension of the film, leading to quasi-2D behavior. On the other hand when $E > E_c$ the system undergoes a dimensional cross-over to 3D since the restricted dimension of the film has no effect on the particles in the time scale $t < \hbar/E_c$. This dimensional cross-over alters the voltage dependence of the tunneling conductance from logarithmic to square-root [8], which is characteristic of 3D diffusive interacting systems. Quantum wells in GaAs therefore provide more ideal 2D systems for testing the theory of electron-electron interactions.

3.4.2 Short Screening Length for 2DEG in GaAs

Another major difference between semiconductor 2DEG's and thin metal films is the magnitude of the screening length. The screening length in metal films is less than 1 $\AA$. This is much smaller than the thickness of the films, which ranges from 50 $\AA$ to 1000 $\AA$. The screening length sets a lower limit for the distance over which non-equilibrium charge accumulation can occur. Tunneling therefore probes the local DOS near the surface of metal films. In contrast, the Thomas-Fermi screening length in GaAs is about 50 $\AA$, comparable to the quantum well thickness of 150 $\AA$. Any non-equilibrium accumulation of charge introduced by tunneling is evenly distributed across the width of the quantum well. Observation of the logarithmic correction in semiconductors therefore provides evidence for the universality of electron-electron

interaction mechanisms in disordered systems with different physical properties.

3.4.3 DOS Corrections in the quasi-ballistic regime

Recall that the logarithmic corrections to the DOS follow from a perturbation calculation in the diffusive regime with expansion parameter $\hbar/E_F\tau$. At energies larger than $\hbar/\tau$ from the Fermi energy, which corresponds to time scale of interaction shorter than the scattering time τ, electron motion changes from diffusive to quasi-ballistic. Since the perturbation calculation by Altshuler, Aronov and Lee is not applicable in this quasi-ballistic regime, it was not clear whether there are corrections to the DOS at energies higher than $\hbar/\tau$ and if so, what the dependence of the correction on energy is.

From Eq. 3.12, the size of the logarithmic correction scales with $\hbar/E_F\tau$. The Coulomb anomaly in tunneling is therefore universal for 2D systems in different materials as long as they have the same $E_F\tau$. For disordered metal films, it is not possible to study the 2D quasi-ballistic regime since the dimensional cross-over from 3D to 2D occurs at a lower energy ($\sim$ 10 meV) than inverse scattering time $\hbar/\tau$ ($> 100meV$). In contrast, the Fermi energy E_F for 2D electron systems in GaAs is a factor of 1000 smaller. The scattering time τ is therefore longer by the same factor for a 2DEG in GaAs with $E_F\tau$ identical to a metal film, reducing $\hbar/\tau$ to a sufficiently low energy so that we can study the DOS correction in the energy range when the electron motion changes from diffusive to ballistic.

In Fig. 3-6, the arrows indicate the voltage $V_o = \hbar/e\tau$ extracted from the slope of the tunneling conductance at each density. When the electron density increases, the degree of disorder in the 2DEG is reduced through more efficient screening. As expected, V_o decreases as the electron density increases, reducing the voltage range where the diffusive regime is applicable. At a density of $1.44 \times 10^{11} cm^{-2}$ ($E_F\tau/\hbar = 10.8$), the logarithmic voltage dependence of tunneling conductance extends to more than a factor of 10 beyond $\hbar/e\tau$, clearly beyond the diffusive regime.

Recently, Rudin et al. [22] predicted that electron-electron interactions in this quasi-ballistic regime indeed lead to a significant correction of the DOS even at en-

ergies larger than $\hbar/\tau$. Rudin's calculation only accounts for the trajectory of an electron scattered by a single impurity, a valid assumption for interactions on time scales shorter than the scattering time τ. One might expect that interference effects we described in section 3.1 would not occur. Nonetheless, the potential of the impurity induces a modulation of electron density around it known as Friedel oscillation. Friedel oscillation occurs due to the abrupt drop in occupation number of the electronic states at the Fermi energy. No electrons are capable of screening the impurity potential at length scales smaller than the Fermi wavelength. The density modulation has period equal to half the Fermi wavelength and decreases in amplitude as inverse square of distance from the impurity. Electrons can be scattered by either the Friedel oscillation or the impurity potential itself. Multiple scattering can therefore occur even when the electron only encounters a single impurity in the time interval τ. The correction to the DOS arises from the interference of scattering on an impurity and on the Friedel oscillation it creates.

3.5 Breakdown of Logarithmic Voltage Dependence at Large Corrections

The logarithmic Coulomb anomaly in tunneling follows from a perturbative approach and should be valid as long as corrections to the original DOS are small. In Fig. 3-6, the tunnel conductance is suppressed by more than 70% near zero bias at low densities. When corrections to the DOS are so large, one expects the perturbation calculation to break down. When the argument of a logarithm approaches zero, it diverges to negative infinity. In fact, there are deviations from logarithmic voltage dependence of the tunneling conductance at small voltages for $E_F\tau = 1$ and 0.83 in Fig. 3-6.

A semi-classical calculation by Levitov and Shytov [23] extended the perturbation result to this limit when the tunneling suppression is strong. In this section, we will describe the semi-classical theory and compare it with our results.

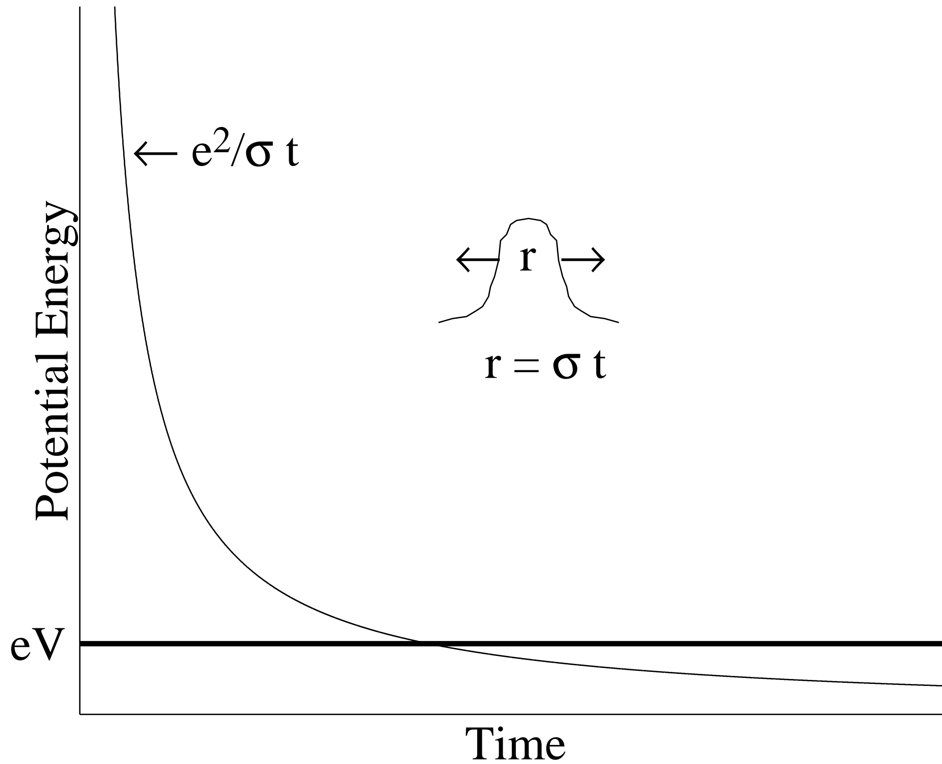

Figure 3-8: This picture illustrates the spreading of a charge distribution under the Coulomb barrier. The tunneling electron has energy eV with respect to the chemical potential of the system. As the size of the charge distribution increases linearly with time, the electrostatic potential energy decreases. The time that the system spends under the Coulomb barrier depends on the energy eV of the tunneling electron.

3.5.1 Semi-classical Theory of the Coulomb Anomaly

In the semi-classical picture by Levitov and Shytov [23], electrons traverse the tunnel barrier and then spread within the 2D system. Since the time that the electron spends under the tunnel barrier is very small compared to the spreading time, tunneling effectively injects an extra electron instantly into the 2DEG. Due to the repulsion from the other electrons, the tunneling electron has a large Coulomb energy and the system has to relax to accommodate the new electron.

Suppose the tunneling electron has energy eV where V is the voltage applied across the tunnel barrier. As charges spread to accommodate the new electron, the system is in a classically forbidden state under the Coulomb barrier (Fig. 3-8). The

Coulomb energy $E(t)$ of the system decreases with time in the following fashion:

$$E(t) \sim \frac{e^2}{r(t)} \sim \frac{e^2}{\sigma t} \tag{3.15}$$

where σ is the in-plane conductivity of the 2D system. Equation 3.15 follows from Maxwell's calculation [24] of the time dependence of the density and potential when a point charge is injected into a two-dimensional system. Maxwell's solution is that the potential in the 2D plane is equivalent to that of a point charge moving normal to the plane at a velocity $v = 2\pi\sigma$ and the size of the charge distribution grows as $r(t) \sim vt \sim \sigma t$.

Under the Coulomb barrier, the tunneling electron picks up extra action $S(t)$:

$$S(t) \sim \int_{\tau}^{t} E(t')dt' = \frac{e^2}{\sigma}\log(\frac{t}{\tau}) \tag{3.16}$$

The reason to choose the scattering time τ as the lower limit of integration is that for time shorter than τ, the spreading of the charges is ballistic and cannot be characterized by conductivity σ. Similar to the case when the electronic wavefunction decays exponentially under a tunnel barrier, the tunneling suppression factor due to the Coulomb barrier is:

$$\exp(-\frac{S(t \simeq \hbar/eV)}{\hbar}) = \exp(-\frac{e^2\log(\hbar/eV\tau)}{\hbar\sigma}) \propto V^{(\sigma_o/\sigma)} \tag{3.17}$$

where σ_o is the conductance quantum e^2/h. A power law dependence of the tunneling conductance on voltage follows:

$$G = AV^{\alpha} \tag{3.18}$$

whose exponent α depends on the ratio of the in-plane conductance σ to the conductance quantum σ_o. An exact expression for α in the presence of screening from the 3D electrode is [23]:

$$\alpha = \frac{\sigma_o}{\sigma}\frac{1}{2\pi}\log(2k_s d) \tag{3.19}$$

where d is the thickness of the tunnel barrier and $1/k_s$ is the screening length.

In the limit of small correction, the semi-classical calculation of the Coulomb anomaly is consistent with results from perturbation theory in following way. Let us rewrite Eq. 3.18 as:

$$\begin{aligned} G(V) &= A'(\frac{V}{V_o})^{\alpha} \\ &= A' \exp(\alpha \log(\frac{V}{V_o})) \\ &\simeq A'(1 + \alpha \log(\frac{V}{V_o})) \end{aligned} \tag{3.20}$$

The expansion of the exponential is valid when the conductance correction $\alpha \log(\frac{V}{V_o})$ is small. Hence we recover the logarithmic voltage dependence of tunneling conductance from the perturbation theory.

3.5.2 Fitting Power Law to Data at large tunneling suppression

Figure 3-9 shows on both linear and semilog scales the normalized conductance measured at electron density $5 \times 10^{10} cm^{-2}$. The dotted line is a logarithmic fit and the solid line is a power law fit. A power law (where the exponent $\alpha = 0.34$) clearly provides a better fit to the tunneling conductance over a larger voltage range. From the exponent of the power law fit, we calculate the in-plane resistance of the 2DEG to be 28 kΩ using Eq. 3.19.

According to Eq. 3.20, the exponent α of the power law should be identical to the prefactor of the logarithmic dependence from perturbation theory when the corrections are small. Even though a power law fits the data well, we are not able to simultaneously fit the data with a power law at low voltages and a logarithm a high voltages using the same α. In fact, α obtained from the power law fit and logarithmic fit in Fig. 3-9 have values of 0.34 and 0.2 respectively. The in-plane resistance and scattering times extracted by the semi-classical result and perturbation theory at this density are shown respectively in Fig. 3-7 as squares and circles.

One possible explanation for the discrepancy might be that at such low densities,

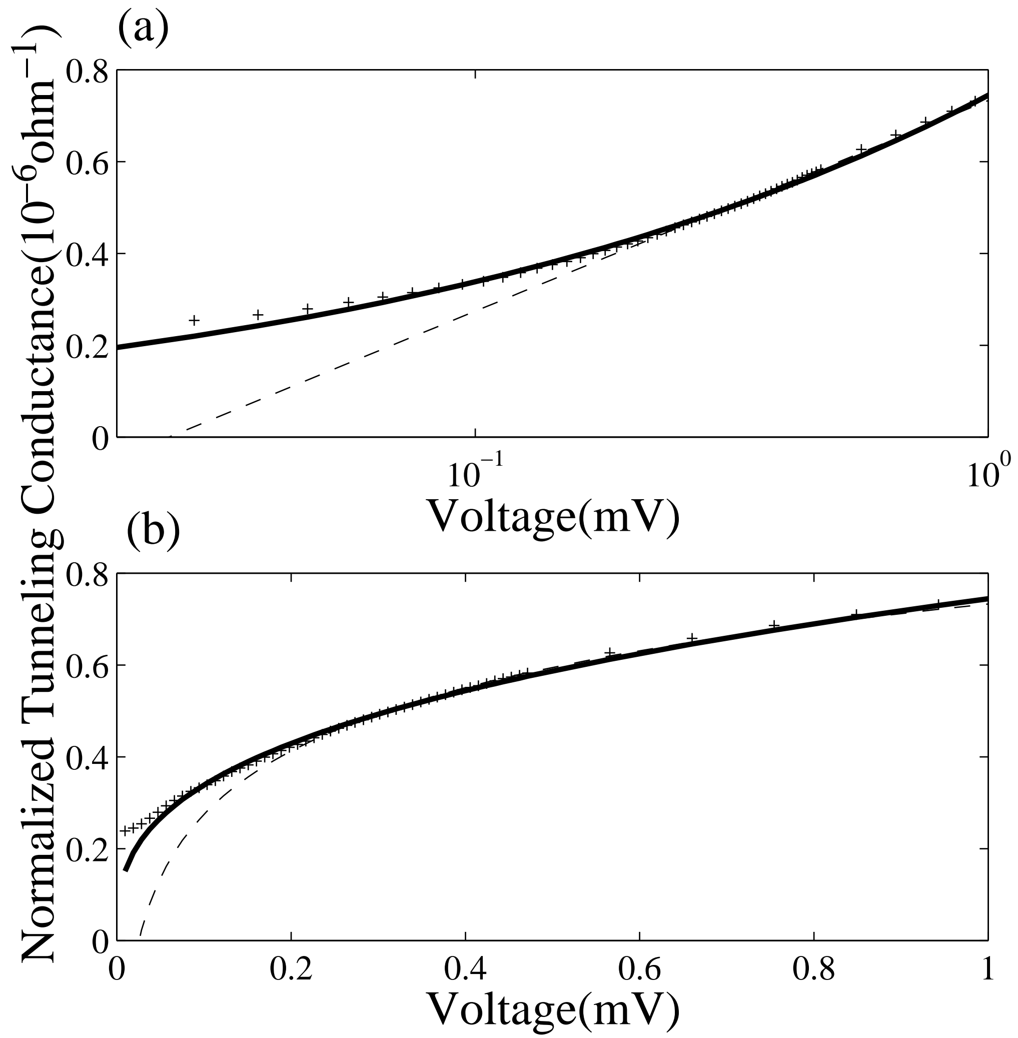

Figure 3-9: Normalized tunneling conductance plotted with (a) linear and (b) logarithmic voltage scales. The crosses are experimental data. The dotted line is a logarithmic fit to the data at $V > 0.3mV$ using Eq. 3.12 from perturbation theory, with $\alpha = 0.2$. The solid line is a power law fit using the semi-classical result (Eq. 3.18), with $\alpha = 0.34$.

the 2DEG might become islanded. Both the perturbation theory and semi-classical calculation requires a well-defined and homogeneous conductivity (over length scales larger than the mean free path of electrons). However, the parameter $E_F\tau$ (or equivalently, k_Fl, where k_F is the Fermi wavevector and l is the mean free path) has a value of ~ 0.83 for the data in Fig. 3-9. Thus the mean free path is of the same order as the Fermi wavelength and localization of the electronic states may occur. For localized electronic states, the main mechanism for electron transport is variable range hopping and a Coulomb gap [5] that depends linearly on energy (which we will discuss in detail in Chapter 4) develops in the single-particle DOS. Pikus and Efros [25] performed a numerical simulation of the DOS for screened Coulomb interaction among classical localized particles and demonstrated that a pseudo-gap in the DOS exists even in the presence of screening. Our tunneling conductance data in Fig. 3-9, which deviate from logarithmic voltage dependence, are likely a precursor of the Coulomb gap in the limit of strongly localized electrons.

3.6 Enhancement of tunneling conductance by weak magnetic field

In this section, we describe the effect of a weak magnetic field ($< 1T$) on the Coulomb anomaly in tunneling. As we will discuss in Chapter 4, the familiar effect of a magnetic field applied perpendicular to the 2D plane is the suppression of tunneling. Here we demonstrate that at low electron densities where the Coulomb anomaly is observed, a magnetic field has the opposite effect: it enhances the tunneling conductance.

3.6.1 Zero-bias conductance in a weak magnetic field

So far, data presented in this Chapter involve measurement of the tunneling conductance as a function of voltage across the tunnel barrier. Since a weak magnetic field only leads to small variations of the tunneling conductance, measurement of the complete tunneling I-V characteristics would require too much time for data averaging.

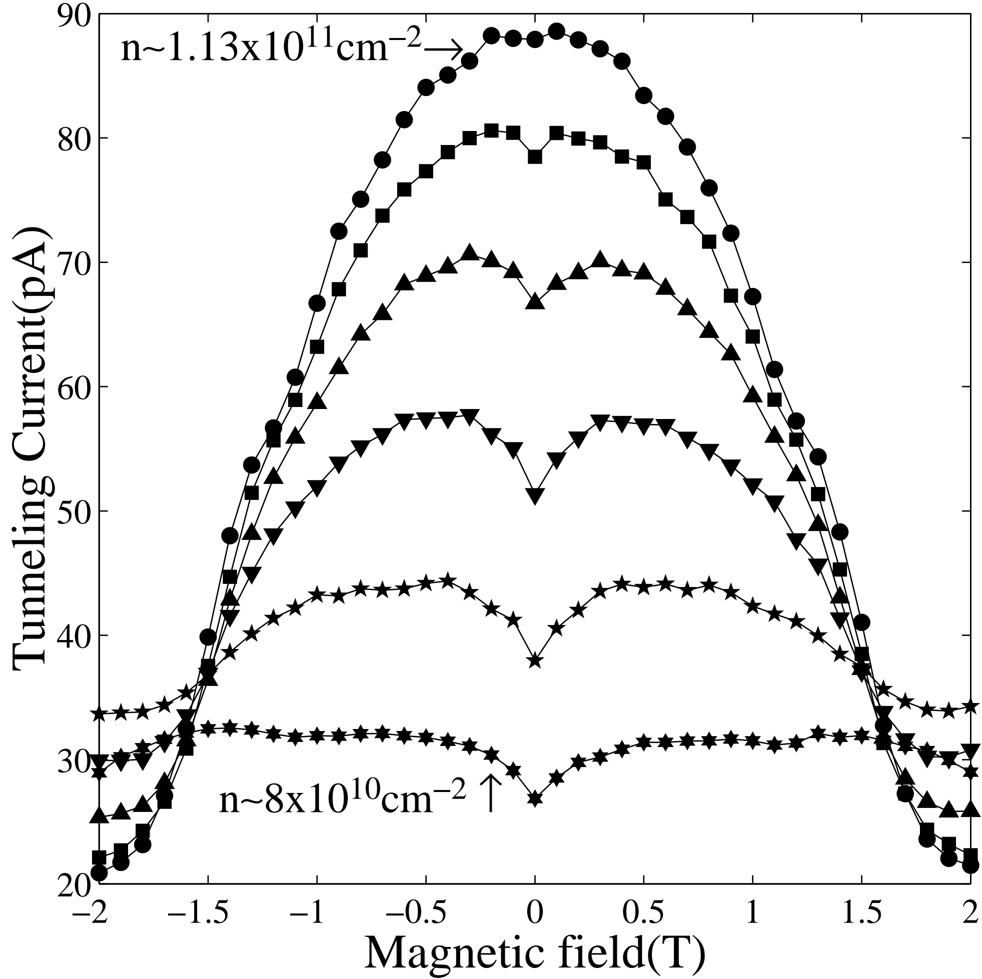

Figure 3-10: Zero-bias tunneling current vs. magnetic field in sample A using an excitation voltage of $2.2\mu V$ at a temperature of 25 mK. The electron density decreases by $7 \times 10^9 cm^{-2}$ for successive curves from the top.

As a result, we measure only the conductance at zero bias as a function of magnetic field and density for data shown in this section.

In Section 2.2, we described "zero-bias" tunneling measurements, which correspond to applying excitation voltages less than the temperature kT so that the tunneling conductance is not affected by non-linearity of the tunneling I-V. We performed the measurement at temperatures less than 100 mK, equivalent to voltages of less than $10\mu V$. Hence we measure the tunneling conductance at the bottom of the tunneling gaps shown in Fig. 3-3.

Figure 3-10 plots the zero bias tunneling current in sample A as a function of

magnetic field ranging from -2T to 2T. For successive curves from the top, the electron density decreases by $7 \times 10^9 cm^{-2}$. We determine the electron density by locating the magnetic field at which the $\nu = 2$ minimum in tunneling current occurs. For instance, the second curve from the bottom in Fig. 3-10 has the $\nu = 2$ minimum at 1.8 T, corresponding to electron density of $8.7 \times 10^{10} cm^{-2}$.

For the top curve at a density of $1.13 \times 10^{11} cm^{-2}$, the tunneling current decreases monotonically as the magnetic field increases. This suppression of tunneling current by a magnetic field corresponds to the formation of magnetic field induced energy gap, which we will discuss in detail in Chapter 4. For lower densities, a minimum in the tunneling current develops at zero magnetic field. In other words, a weak perpendicular magnetic field enhances the tunneling current when the electron density is low. The familiar effect of a magnetic field is the suppression of tunneling. Here we demonstrate that when the electron density is low a weak magnetic field has the opposite effect and instead enhances the tunneling conductance. The density range over which the enhancement occurs coincides with the regime in which there are logarithmic corrections to the tunneling conductance at zero magnetic field. To verify that the enhancement in tunneling conductance by magnetic field only happens in the presence of the Coulomb anomaly, we measure a sample with much higher mobility (the structure of which we will describe in Chapter 5). Due to the small degree of disorder in the high mobility sample, the Coulomb anomaly occurs at a density of $< 3 \times 10^{10} cm^{-2}$, a factor of 5 lower than the sample studied in this chapter. We found that in the high mobility sample, the tunneling enhancement occurs at the same density range as the Coulomb anomaly. This suggests that in general the tunneling anomaly at zero magnetic field and the tunneling enhancement by a weak field take place in the same density range.

3.6.2 Measurements in perpendicular and parallel fields

A magnetic field affects both the orbital motion and the spin of the electrons. One way to distinguish which of these two effects is responsible for the tunneling enhancement is by applying a magnetic field parallel to the 2D plane, since a parallel field only

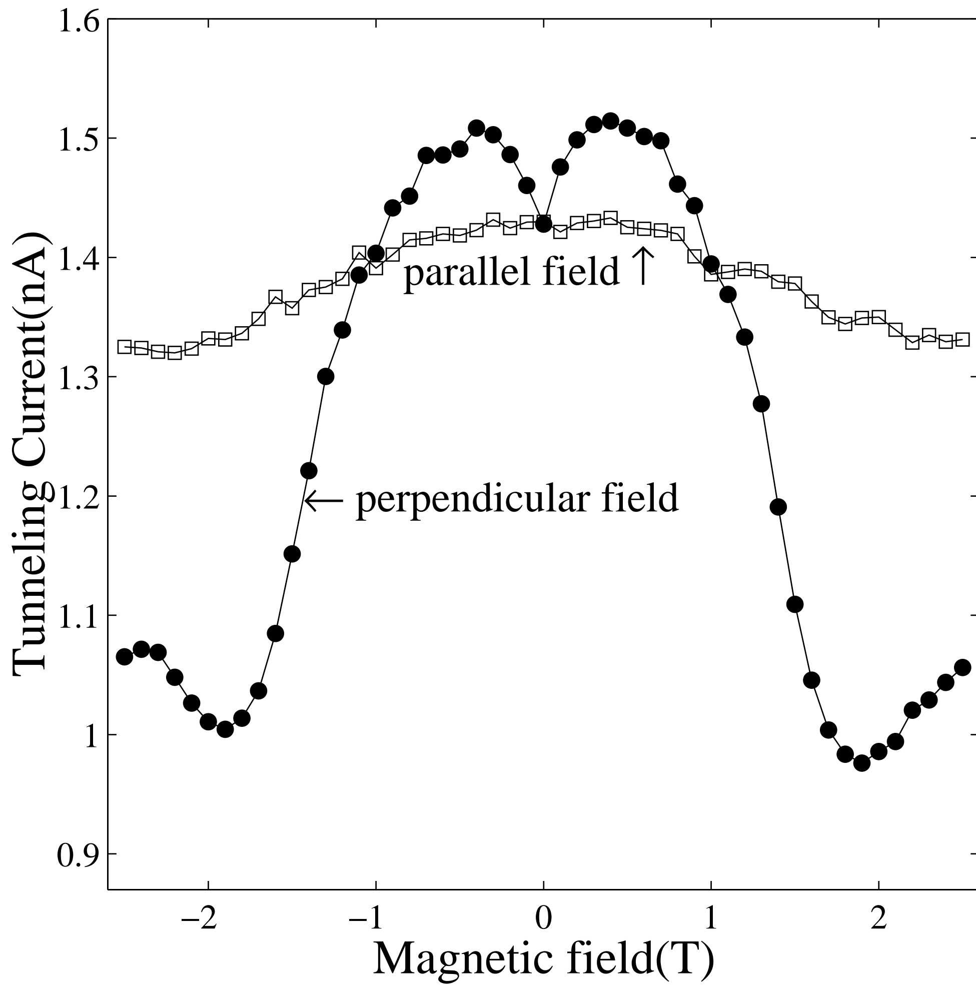

Figure 3-11: Tunneling current vs. magnetic field strength for perpendicular (filled circles) and parallel (hollow squares) magnetic fields for sample m060296A at electron density of $9 \times 10^{10} cm^{-2}$. There is tunneling enhancement only when the applied field is perpendicular to the 2D plane. The minimum at 2T corresponds to the formation of the $\nu = 2$ quantum Hall state.

couples to the spin of the electrons.

Experimentally it is much easier to rotate the sample rather than the magnetic field. In order to measure the tunneling current in both perpendicular and parallel magnetic field orientation, we mounted sample m062696A on a special probe which permits rotation of the sample by 90 degrees without thermally cycling the sample to room temperature. Figure 3-11 shows the data obtained. Data points in filled circles and hollow squares represent tunneling current as a function magnetic field applied perpendicular and parallel to the 2DEG respectively. Figure 3-11 demonstrates clearly that the enhancement in tunneling conductance only occurs in a magnetic field perpendicular to the 2D plane but not in a parallel field. This leads us to conclude that the enhancement is due to magnetic field effects on the orbital motions of the electrons. Nevertheless, there still are two such mechanisms that can lead to enhancement of the tunneling conductance through coupling to the orbital motions of the electrons. At present, we cannot conclude which mechanism is relevant in producing the enhancement. We describe both mechanisms in the following two sub-sections.

3.6.3 Weak localization effects on tunneling conductance

The enhancement of tunneling conductance is reminiscent of the effect of weak localization on the in-plane conductance of disordered 2D systems. Experiments on thin metal films [26] or silicon MOSFETs [27] demonstrated that due to the quantum mechanical interference effects, the in-plane conductance increases with the application of a small perpendicular magnetic field.

Weak localization arises from the wave nature of conduction electrons [26, 28, 29, 30]. Consider a particle undergoing diffusive motion in Fig. 3-12. It has a nonzero probability of being scattered back to its original position O. There is an equal probability for another partial wave to propagate in the opposite direction and follow exactly the same path, as indicated by the dotted arrow. This partial wave returns to the origin O with the same phase as the first partial wave. Therefore, in calculating the probability of particle being scattered back to the origin, the amplitudes rather

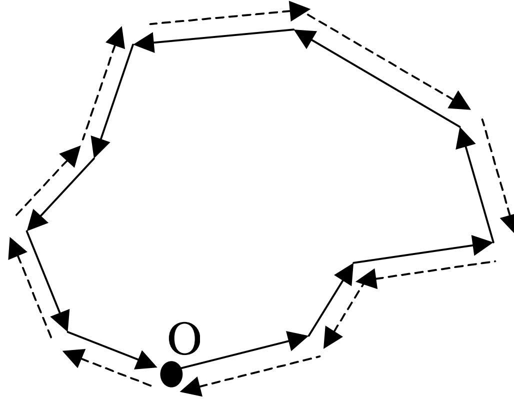

Figure 3-12: A particle undergoing diffusion has a finite probability of returning to its starting point O. The solid arrows represent one of the possible trajectories. The particle has an equal probability of taking the time-reversed path indicated by dotted arrows. The two partial waves returns to the origin O with the same phase, resulting in constructive interference.

than intensities of the partial waves add, leading to constructive interference. The probability of returning to the origin is twice as large as the classical case. This coherent backscattering leads to a reduction of the in plane conductance in 2D from its classical value. Recall that in section 3.1 we described the interference effect between two interacting electrons. For weak localization, the qualitative picture is similar except we consider partial waves of a single electron and neglect the interactions with other electrons.

A perpendicular magnetic field weakens or destroys the phase coherence between the two partial waves. When the partial waves enclose an area containing magnetic flux ϕ, the relative phase between the two partial waves changes by $(2e\phi/\hbar)$. Different diffusion paths enclose different areas. The interference for paths enclosing different areas can be either constructive or destructive in a magnetic field and the average cancels. Increasing the strength of the magnetic field affects the coherence of paths enclosing smaller areas.

A sufficiently strong magnetic field therefore restores the in-plane conductance back to its classical value. In other words, the perpendicular magnetic field enhances the in-plane conductance. However, weak localization by itself has no effect on the tunneling conductance. Even from the simple description above, we notice that local-

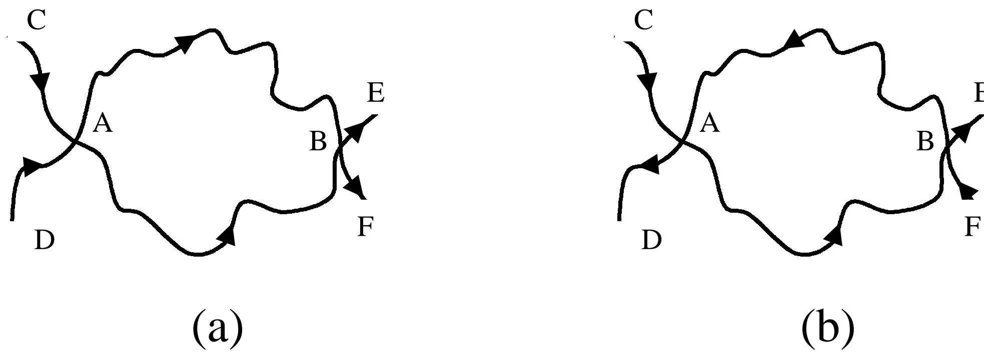

Figure 3-13: (a) Two particles undergoing diffusive motion. The trajectories intersect at points A and B where the particles interact. The arrows indicate the direction of motion. (b) In the Cooper interaction channel, the direction of one of the particles is reversed. The particles pass through points A and B in different order.

ization does not affect the energy of the diffusive electrons. In attempting to explain the enhancement in tunneling conductance by a magnetic field, it is necessary to consider a combination of interaction and localization effects.

In the perturbation calculation by Altshular, Aronov and Lee [6] for an interacting and disordered 2D system, the obvious way weak localization modifies the Coulomb anomaly is by increasing the in-plane resistance. Application of a weak perpendicular magnetic field removes this effect. This decreases the factor in front of the logarithmic correction in Eq. 3.11 and reduces the tunneling suppression. In the semi-classical calculation [23] that predicts power law IV, a lower in-plane resistance decreases the exponent in the power law, leading to higher equilibrium tunneling conductance at finite temperature.

3.6.4 Cooper channel interactions in a disordered 2DEG

A perpendicular magnetic field can also enhance the tunneling conductance by suppressing the Cooper channel of electron-electron interaction and reducing the Coulomb anomaly.

The Cooper channel refers to interaction between two electrons of similar energies but a small net momentum [17, 30]. Figure 3-13 provides a qualitative picture of

the Cooper channel interaction for a diffusive electronic system. In Fig. 3-13a, the two electrons diffuse respectively from point C to point E, and from point D to F. The trajectories cross at points A and B, where the electrons interact. Suppose one electron transfers energy $\hbar\omega$ to the other electron. If the time it takes for the electrons to travel from point A to point B is short compared with ω^{-1}, the phases of the transition amplitudes at point A and B are close to each other and will interfere constructively. This interference corresponds to the diffusion channel interaction and gives rise to the correction in the DOS. We introduced this qualitative picture earlier, in section 3.1.

For the Cooper channel interaction, one of the electrons travels in the reversed direction from point F to point D, as shown in Fig. 3-13b. The electrons move in opposite directions and have a small net momentum. Unlike the diffusion channel in Fig. 3-13a, the electrons therefore go through points A and B in different order. It would seem that since the electrons do not go through points A and B simultaneously, no interference can occur between interactions at the two points. Nonetheless, if the time to go from point A to point B is short compared to the inverse interaction energy, the time at which each particle passes through points A and B cannot be determined due to the uncertainty principle. In this case, there will be interference of the interaction amplitudes, leading to the Cooper channel interaction.

Figure. 3-13a becomes Fig. 3-13b if one particle travels in reversed direction, i.e. the time of one of the particles is reversed. The system must be invariant under time reversal for Cooper channel interaction to be substantial. Since a perpendicular magnetic field destroys time reversal symmetry, it also suppresses Cooper channel interaction. A perpendicular magnetic field therefore reduces the corrections to the DOS by destroying one of the interaction mechanisms, leading to an enhancement of the tunneling conductance.

The existence of both weak localization and Cooper channel interaction are contingent upon time-invariance. At present, we cannot determine which of the two effects is responsible for the enhancement in tunneling conductance we observed.

It would be instructive to compare the magnitude of the magnetic field enhance-

ment of tunneling conductance and in-plane conductance. Unfortunately, since there are no ohmic contacts to the 2DEG in our samples as we mentioned in Chapter 2, we cannot measure the in-plane conductance directly. From the prefactor of the logarithmic voltage dependence of the tunneling conductance (Eq. 3.11) in zero magnetic field, we deduce that the in-plane resistance ranges between 5 $k\Omega$ and 10 $k\Omega$ when the magnetic field enhancement of tunneling takes place. Weak localization typically increases the conductance by $2e^2/h$ (equivalent to 13 $k\Omega$). Such effect on the 2DEG in our samples produces about 30% decrease in the in-plane resistance. In Figs. 3-10 and 3-11, application of a perpendicular magnetic field only enhances the tunneling conductance by less than 10%. It would seem that the decrease of in-plane resistance due to weak localization is more than sufficient to explain the tunneling enhancement in a weak field. However, as we will discuss in Chapter 4, a strong magnetic field leads to the formation of an energy gap for tunneling into the 2D system. As a result, a perpendicular magnetic field produces two opposite and competing effects in the low density regime. At low magnetic fields, the tunneling enhancement that we described in this section dominates. As the magnetic field increases, the suppression effect of the tunneling gap takes over, as shown in Figs. 3-10 and 3-11 for magnetic fields higher than 1 T. Since the presence of the tunneling gap reduces significantly the tunneling enhancement we observe, we cannot conclude that the reduction of in-plane resistance by weak localization is adequate to explain the tunneling enhancement, even though the tunneling current only rises by $< 10\%$ in Fig. 3-10.

It might be possible to distinguish whether the tunneling enhancement is due to the Cooper channel interaction or a combination of weak localization and electron-electron interactions by measuring the excitation dependence of the tunneling conductance. Weak localization modifies the prefactor of the logarithmic correction in Eq. 3.11. Application of a perpendicular magnetic field suppresses weak localization and reduces the logarithmic corrections to the tunneling conductance at all excitations by the same factor. On the other hand, corrections to the tunneling conductance due to the Cooper channel interaction are expected to be restricted to small excitations [11, 17]. Measurement of the excitation dependence of the tunneling conductance at

various magnetic field strengths would certainly provide useful information in understanding the tunneling enhancement in weak magnetic fields.

3.7 Summary

In conclusion, we measure the Coulomb anomaly for tunneling into a disordered 2DEG and observe the logarithmic voltage dependence of the tunneling conductance for the first time in semiconductor 2D systems. The long scattering time for the 2DEG in GaAs enables us to study the DOS corrections at energies higher than the inverse scattering time in the quasi-ballistic limit. We demonstrate that the logarithmic correction to the DOS persists beyond the diffusive limit.

We also study the deviations to the logarithmic DOS correction in the limit $k_F l \simeq 1$ and find that a power law provides a better fit to the tunneling conductance. However, we do not have complete agreement with the semi-classical calculation that predicts a power law I-V for tunneling. In contrary to the theory, the exponent of the power law fit differs from the prefactor of the logarithmic fit at high voltages when corrections are small. We suggest that this may arise from inhomogeneity of the sample at low densities.

Furthermore, we find that a weak perpendicular magnetic field enhances the zero-bias tunneling conductance in the density range where the logarithmic Coulomb anomaly exists in zero magnetic field. At present, we cannot conclude whether a combination of weak localization and electron-electron interactions or the suppression of Cooper channel interactions is responsible for the enhancement.

Chapter 4

Linear Energy Gap for Tunneling into the 2DEG in perpendicular Magnetic Field

Characteristics of electrons tunneling into and out of a two dimensional (2D) system differ considerably from those of the three dimensional (3D) case. The distinction is especially pronounced when a magnetic field is applied in the tunneling direction (perpendicular to the plane in the 2D case). In the simplest picture (Fig. 4-1), such a magnetic field effectively localizes electrons in the 2D system. An electron tunneling into an energetically unfavorable position cannot readily move away and instead tends to move in circles. As a result, tunneling measurements of 2D systems in magnetic field display effects attributable to a "pseudogap" in the single-particle DOS at low injection energies [15, 19, 20, 21, 31, 32]. In contrast, for a 3D system the tunneling electron can move parallel to the field lines to evade being localized at a position of high potential energy and such a field-induced gap has not been detected.

This suppression of tunneling by a perpendicular magnetic field was first observed by Ashoori et al. [19] in the temperature dependence of "zero-bias" tunneling between a 2DEG and a 3D substrate. Eisenstein et al. [15] and Brown et al. [31] subsequently measured the current-voltage characteristics for tunneling between two 2D electron systems and find that the tunneling conductance is suppressed at small voltages.

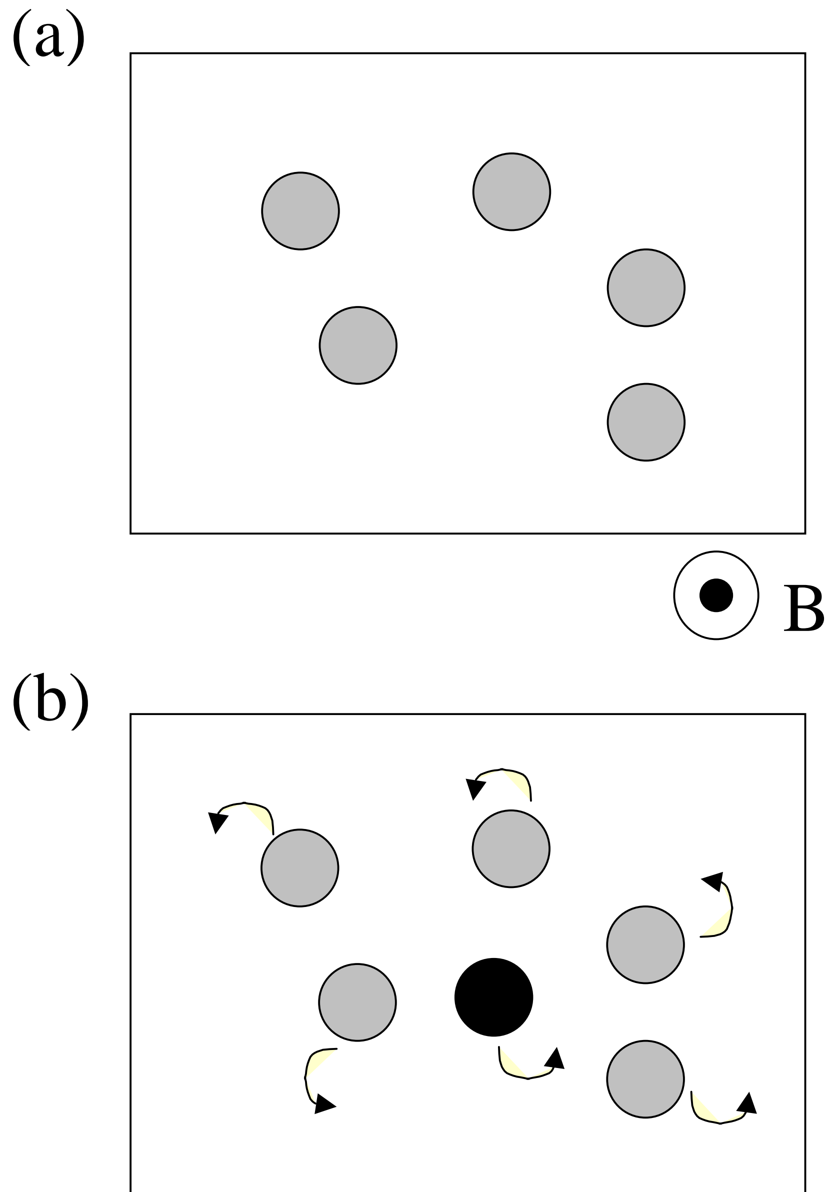

Figure 4-1: (a) Electrons in the 2D system arrange themselves in positions that minimize their energy with respect to both the disordered background and their mutual repulsion. (b) An extra electron injected into the system has a high Coulomb energy. Electrons can reduce this Coulomb energy by moving away from one another, but the magnetic field instead forces them to move in circles.

In this Chapter, we perform a detailed survey of the excitation dependence of the tunneling conductance into a 2DEG from a 3D electrode in a magnetic field and in the presence of disorder using Time Domain Capacitance Spectroscopy (TDCS) that we described in Chapter 2. In the low excitation regime, we find a behavior that is not predicted by any of the prior theoretical models for this system [25, 33, 34, 35, 36, 37, 38]. We find that the single-particle DOS has a universal linear dependence on energy near the Fermi energy for all field strengths and electron densities. Moreover, the slopes of this linear gap are proportional to the inverse of the magnetic field strength over a wide range of fields. We will describe a phenomenological model that fits to the main features of the magnetic field induced gap.

4.1 Samples

TDCS measures the complete tunneling current-voltage characteristics without making an ohmic contact to the 2DEG. We are able to measure for the first time the contribution of localized states to the tunneling current.

Figure 4-2 shows the essential structure of samples used in TDCS measurement. The samples are GaAs/AlGaAs heterostructures grown by molecular beam epitaxy. In this chapter, we present data from two samples: sample A and sample m060296a. The substrate is n+ doped GaAs for both samples. First, we grow a GaAs spacer layer on top of the substrate. Then we grow an AlGaAs tunnel barrier, followed by a GaAs quantum well, which defines the 2D system. The AlGaAs blocking barrier is thick and prevents conduction between the 2D system and the GaAs top electrode. We introduce dopants in the AlGaAs to provide electrons for the quantum well. The AlGaAs regions in both samples have 30% aluminum concentration.

Sample A was grown by S. Wright and has been studied extensively using AC capacitance techniques [7, 19, 20, 21]. The concentration of silicon dopants in the degenerately n-doped substrate is $1 \times 10^{17} cm^{-3}$. The thickness of the layers, from bottom to top, are as follows: 30 $\AA$ GaAs undoped spacer, 160 $\AA$ AlGaAs undoped tunnel barrier, 150 $\AA$ GaAs undoped quantum well, 1550 $\AA$ AlGaAs blocking barrier

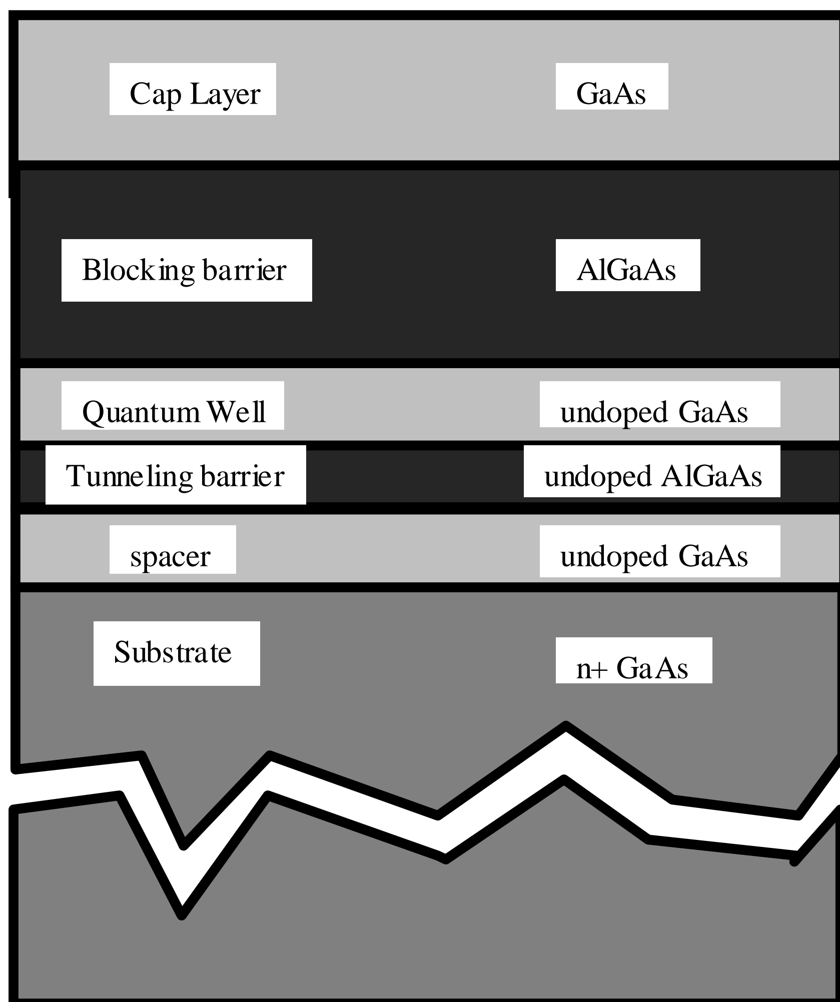

Figure 4-2: The essential layer structure of the samples.

and a degenerately n doped GaAs cap layer. In the AlGaAs blocking barrier, dopants are introduced in the region from 100 $\AA$ to 200 $\AA$ away from its lower boundary to provide electrons for the quantum well. A gold-germanium ohmic contact to the GaAs cap layer allows variation of 2D electron density from depletion to $6 \times 10^{11} cm^{-2}$. The circular mesa has a diameter of 400 μm.

Sample m060296A was grown by Prof. M. L. Melloch at Purdue University. The substrate has silicon dopant concentration of $5 \times 10^{17} cm^{-3}$. The thickness of the layers, from bottom to top, are as follows: 50 $\AA$ GaAs undoped spacer, 143 $\AA$ AlGaAs undoped tunnel barrier, 150 $\AA$ GaAs undoped quantum well, 550 $\AA$ AlGaAs blocking barrier and a 50 $\AA$ undoped GaAs cap layer. In the AlGaAs blocking barrier, dopants at a concentration of $5 \times 10^{17} cm^{-3}$ are introduced in the region from 200 $\AA$ to 350 $\AA$ away from its lower boundary to provide electrons for the quantum well. A chromium gold Schottky contact to the GaAs cap layer allows variation of 2D electron density from depletion to $3 \times 10^{11} cm^{-2}$. The circular mesa has a diameter of 300 μm.

Appendix C describes the fabrication process for the samples.

4.2 Linear Dependence of Tunneling conductance on Voltage

Figure 4-3 shows the tunneling conductance (I/V) of sample A plotted against the voltage across the barrier for magnetic field strengths of 0, 1, 2, 8 and 16 Tesla at a fixed electron density of $1.9 \times 10^{11} cm^{-2}$. This density is high enough so that the zero-bias tunneling anomaly described in Chapter 3 has receded at zero field. Application of a magnetic field reduces the tunneling conductance around zero bias. The suppression becomes deeper and wider as the field is increased. This field-induced tunneling suppression differs qualitatively from the logarithmic suppression described in Chapter 3 in the low density regime at zero field. Near zero bias, we find that the conductance has a universal linear dependence on the excitation voltage for all field strengths and electron densities. Moreover, an increase in the strength of the

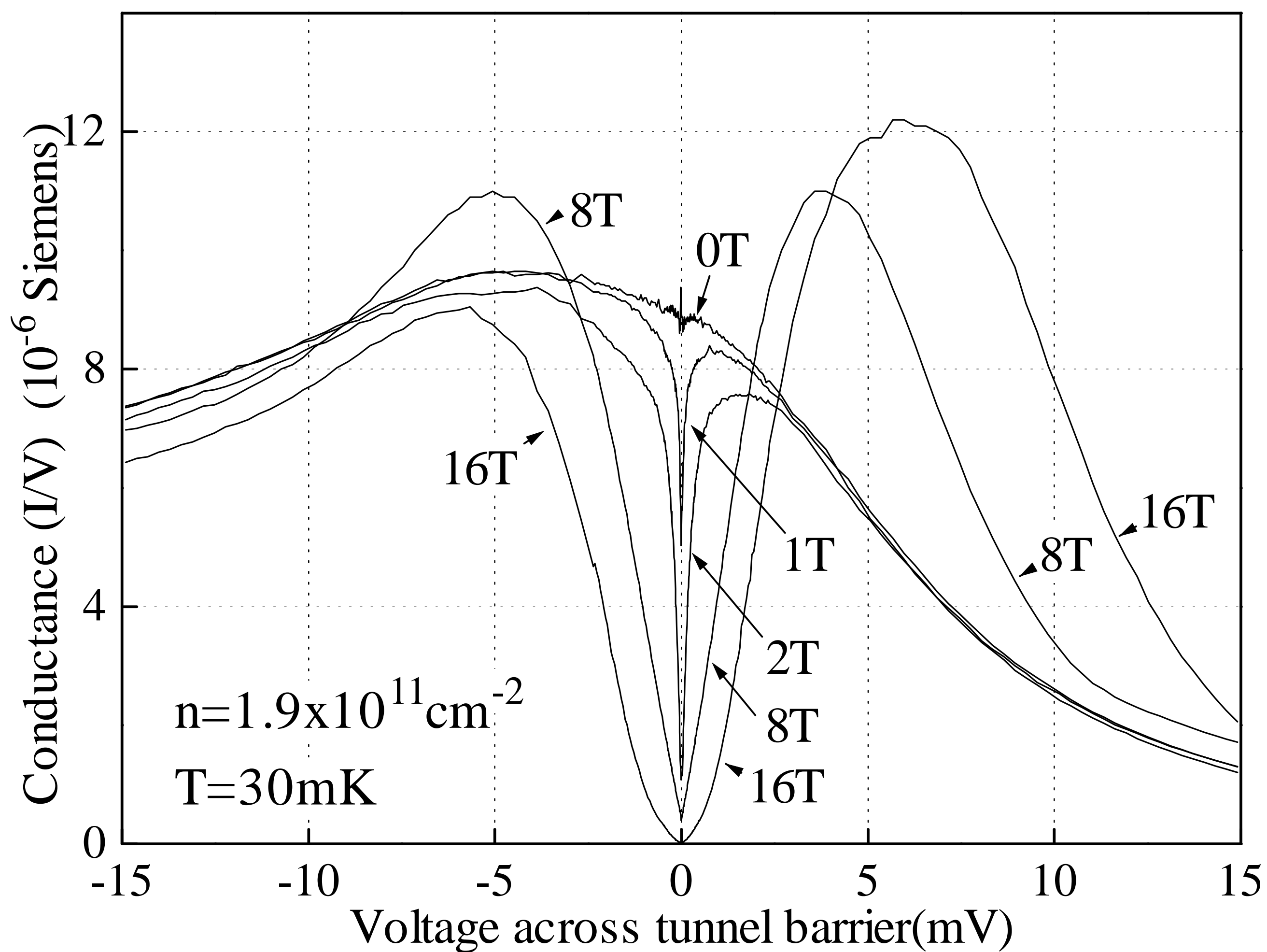

Figure 4-3: Dependence of the tunneling conductance of sample A on the excitation voltage across the tunnel barrier for different magnetic field strengths at 30 mK and a fixed density of $1.9 \times 10^{11} cm^{-2}$.

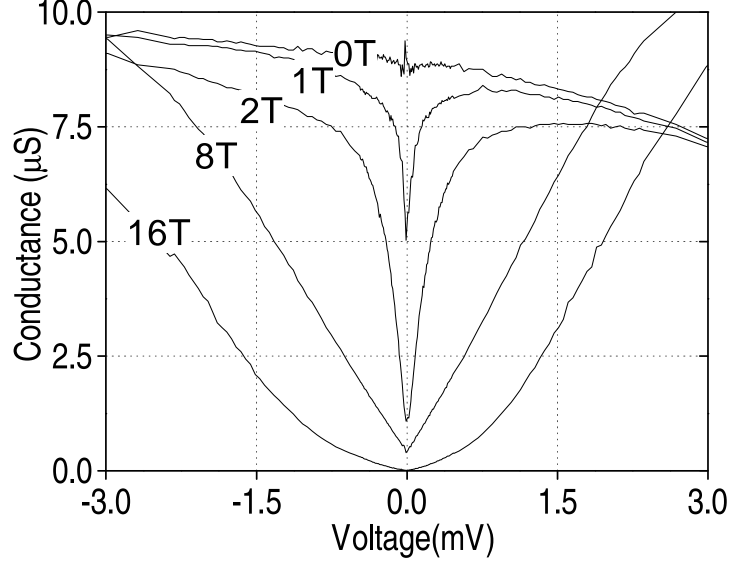

Figure 4-4: Dependence of the tunneling conductance of sample A on the excitation voltage across the tunnel barrier for different magnetic field strengths at 30 mK and a fixed density of $1.9 \times 10^{11} cm^{-2}$.

suppression is accompanied by a change in the curvature of the high excitation part of the conductance curves when the magnetic field is increased, as shown by Fig. 4-4.

Even though the conductance curves at high excitation appear rounded at high fields, the zero bias region remarkably remains linear in voltage, with both the magnitude and the slope significantly reduced. This singular behavior is illustrated by Fig. 4-5, which zooms in near the zero bias region of the conductance curves for different field strengths. Such a linear energy dependence of the single particle DOS is observed over the full range of densities in both sample A and sample m060296A except near depletion ($N \leq 5 \times 10^{10} cm^{-2}$).

To our knowledge, no existing model other than the 2D Coulomb gap [5, 25], which we will describe in section 4.4, predicts such a universal linear DOS at low energies for such a wide range of field strengths and densities as observed in our samples. However, contrary to expectations for a simple Coulomb gap the slopes of the observed linear gap are strongly field dependent. Figure 4-6 shows the slopes of the linear regions of the conductance curves plotted against inverse magnetic field strength. For filling factors $\nu < 1$, the data points fall onto a straight line extrapolating to a negative

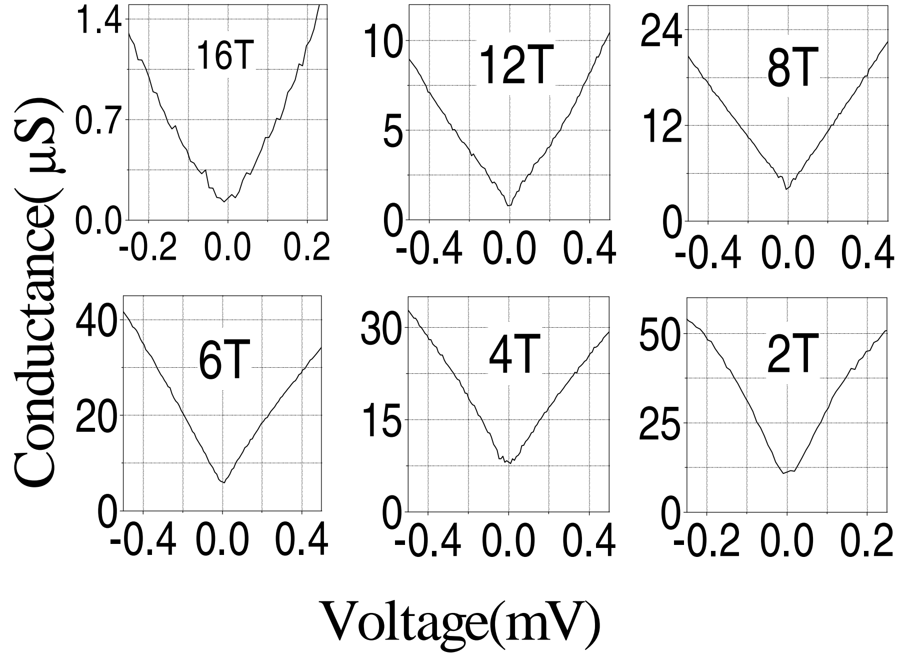

Figure 4-5: Tunneling conductance as a function of excitation voltage for 6 different magnetic field strengths. Different ranges are chosen to display the singular behavior near zero bias.

intercept on the vertical axis. For low fields, there are deviations from the straight line as ν varies between integer and non-integer values.

For different 2D electron densities, the conductance curves remain linear near zero bias. As a function of density, the slopes of the linear pseudogap exhibit minima at integer ν. For instance, at 8 Tesla the magnitude of the slope drops by a factor of 2 at $\nu = 2$ compared to $\nu = 1.5$. In Fig. 4-6, data points corresponding to integer ν are marked. These minima in the slope of the linear gap at integer ν might be attributed to a smaller background DOS between two Landau levels. Other than particulars associated with integer ν, our data display only a very weak overall density dependence. The dominant factor in determining the slope of the linear gap is the magnetic field strength.

For completeness, we also show data for a different sample. Figure 4-7 plots the tunneling conductance curves of sample m060296a grown in a different MBE machine. We observe the same linear voltage dependence of the tunneling conductance in this sample. Furthermore, the slope of the linear gap decreases with increasing magnetic

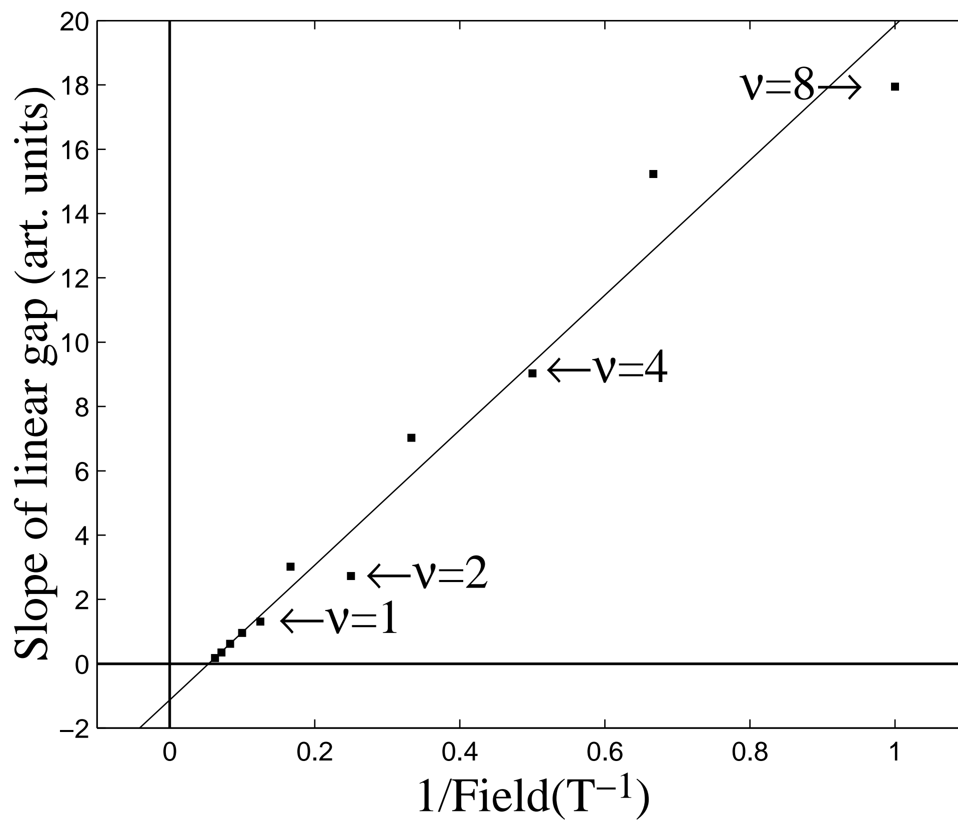

Figure 4-6: Slope of the linear gap vs. inverse field strength. The slope of the gap varies inversely with magnetic field with an offset.

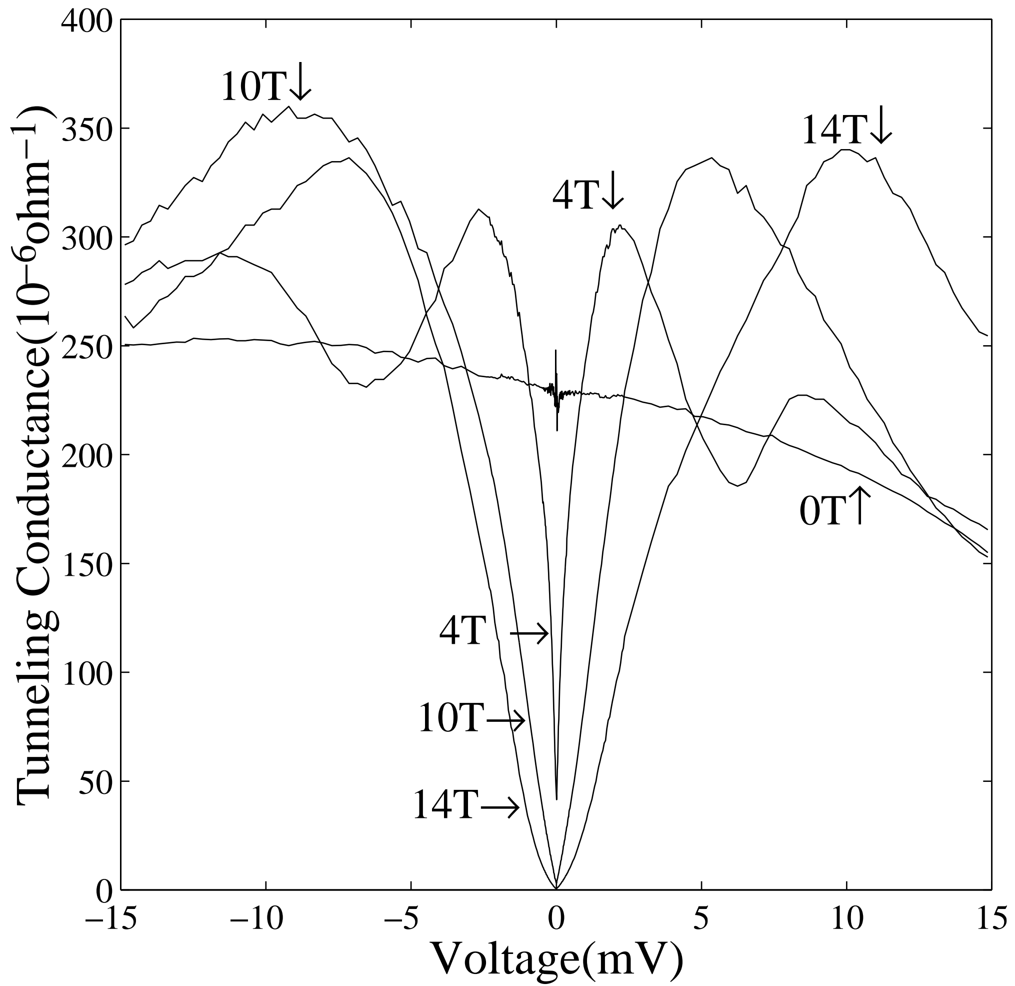

Figure 4-7: Dependence of the tunneling conductance of sample m060296a on the excitation voltage across the tunnel barrier for different magnetic field strengths at 30 mK and a fixed density of $2.9 \times 10^{11} cm^{-2}$. In addition to the zero bias suppression, the conductance curve at 4T and $\nu \sim 3$ shows minima at $\pm$6mV associated with Landau levels at higher excitations.

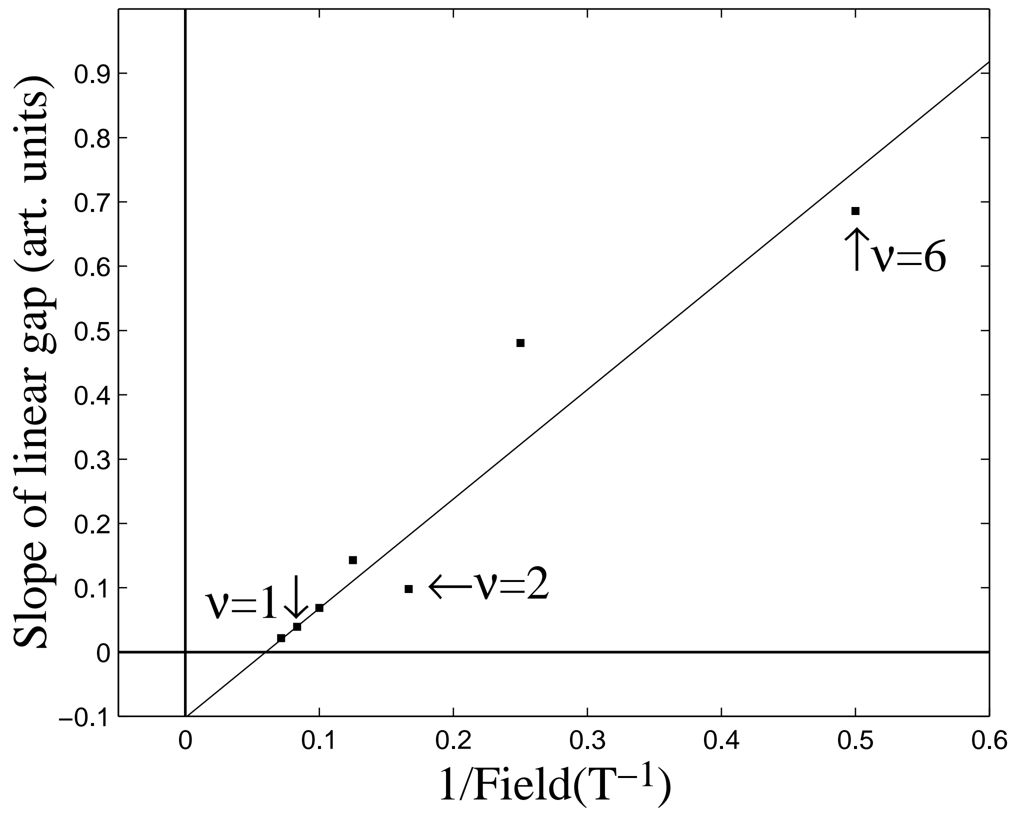

Figure 4-8: Slope of the linear gap vs. inverse field strength in sample m060296a. The slope of the gap varies inversely with magnetic field with an offset.

field in the same fashion as in the sample A as illustrated by Fig. 4-8. In Chapter 5, we will describe samples with much higher mobility. The tunneling conductance of these samples displays the same linear voltage dependence around zero bias at low magnetic fields (Fig. 5-3). However, the slopes of the V-shaped pseudogap decrease more rapidly with increasing magnetic field.

4.3 Comparison of TDCS data to tunneling data from double quantum wells

There have been two other experiments [15, 31] that investigated the effect of this magnetic field induced energy gap on tunneling I-V characteristics. The samples in these experiments consist of two 2DEG's with independent ohmic contacts. Both experiments focus on the dependence of the width of the tunneling gap on magnetic field and density. There have not been any reports of linear voltage dependence of the tunneling conductance at small voltages. In this section, we explain why previous experiments did not detect the singular behaviour of the gap near zero bias observed in our measurement.

In order to compare our data to results from previous double well experiments, we compute the I-V curves expected for tunneling between two 2D electron systems:

$$I \propto \int_0^{eV} n(E - eV)n(E)dE \tag{4.1}$$

Here both 2D systems are assumed to have identical tunneling density of states $n(E)$ deduced from our 2D-3D tunneling data from sample A at 16 Tesla in Fig. 4-3. Equation 4.1 resembles a convolution integral (except the upper limit of integration is eV instead of infinity). One can refer to Section 1.4 for a detailed discussion and derivation of Eq. 4.1. The basic idea is that tunneling can only take place when there is a filled state in one 2DEG and an empty state at the same energy in the other 2DEG.

The resulting I-V curve, as shown in Fig. 4-9, qualitatively resembles that from

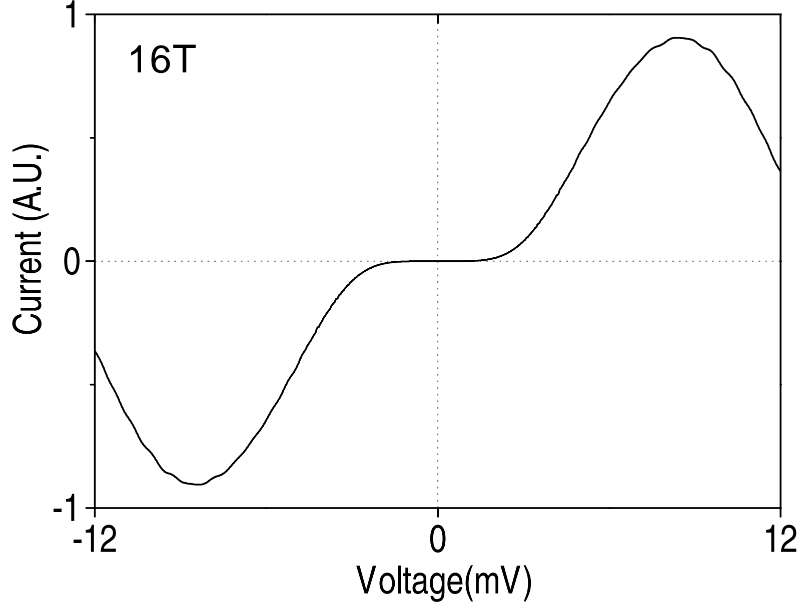

Figure 4-9: Simulated I-V curve for tunneling between two 2DEG's, assuming the tunneling DOS of each 2DEG develops the pseudo-gap deduced from our 16 T conductance curves in Fig. 4-3.

double well experiments [15, 31] with no singularities at zero bias. In our opinion, previous tunneling experiments did not resolve the linear tunneling gap as we did due to the convolution effects (Eq. 4.1) on the DOS in double-well systems.

4.4 Linear Coulomb gap with universal slope in 2D

In this section we describe the Coulomb gap [5] in the single-particle DOS of a system of classical point charges. The Coulomb gap has a linear energy dependence for 2D systems. It provides a good starting point in understanding our data.

Consider a 2D system of electrons in a disordered background potential. We assume that the electron concentration is so low that the average spatial separation is larger than the size of the wavefunction. Hence there is no overlapping of wavefunctions and we can treat the electrons as classical point charges occupying sites randomly distributed in space. The existence of a random background potential leads to a distribution in the energies of the sites as shown in Fig. 4-10a.

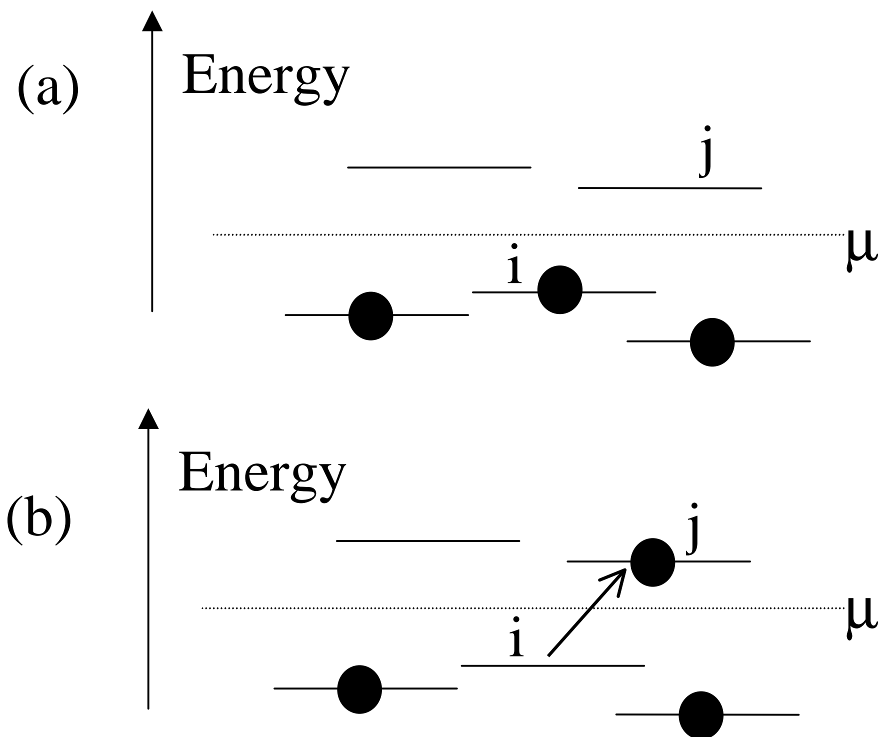

Figure 4-10: (a) Energy diagram for system of classical point charges in the ground state. Levels below the chemical potential μ are occupied. (b) If we transfer a particle from site i to site j the energy of the system increases.

In a tunneling event, we add an extra electron or remove one electron from the system. Suppose the energy of the system increases by E_j when we put an extra electron on to site j. If instead we take an electron away from site i the energy of the system decreases by E_i. To clarify the meaning of E_i and E_j, assume we put an electron reservoir close to this system. If the chemical potential in the reservoir is higher than E_j, an electron tunnels into the system onto site j. On the other hand, if the chemical potential in the reservoir is lower than E_i, an electron leave site i and tunnel into the reservoir.

In the next step, we will demonstrate that that there is a very low probability of finding a site with energy E_i if E_i is very close to the chemical potential. At energies further away from the chemical potential, the chances of finding a tunneling site increases. Let us imagine removing the tunneling reservoir and consider the system by itself. Suppose in the ground state, site i is occupied while site j is empty, as shown in Fig. 4-10a. In Fig. 4-10b we transfer an electron from site i to site j and the energy of the system changes. We can calculate this energy change in two steps. First we take the electron from site i to infinity. By definition the energy of the system changes by E_i. The system now has N-1 electrons. In the second step we put this electron from infinity back onto site j. This would have added energy E_j back to the system if site i were already occupied. Recall that E_j is defined as the energy added to the original N particle system if we put an electron onto site j. However, the system now has one electron missing from site i. As a result, we need to correct E_j by an amount $e^2/\kappa r_{ij}$, where κ is the dielectric constant and r_{ij} is the distance between the sites i and j.

Therefore, the energy change ΔE of moving an electron from site i to site j is:

$$\Delta E = \delta E(take\ i\ away) + \delta E(put\ on\ j) \quad (4.2)$$

$$= -E_i + (E_j - \frac{e^2}{\kappa r_{ij}}) > 0 \quad (4.3)$$

Since by definition our system was originally in the ground state before we perform this shuffling of particles, the energy change ΔE must be positive. Simple rearrange-

ment of terms leads to the following restriction on the distance between sites i and j of given energies:

$$r_{ij} > \frac{e^2}{\epsilon(E_j - E_i)} \tag{4.4}$$

The physical meaning of Eq. 4.4 is that if there are two sites very close in energy near the chemical potential, they have to be very far apart spatially so that their Coulomb repulsion is small. This imposes a limit on the number of states available for tunneling of electrons near the chemical potential. In two dimensions, the total number per unit area N of available tunneling states within an energy of E about the chemical potential is [5]:

$$N(E) = \frac{1}{r_{ij}^2} = \frac{\kappa^2 E^2}{e^4} \tag{4.5}$$

The derivative of the total number of states N with respect to energy gives the density of states $n(E)$:

$$n(E) = \frac{dN}{dE} = \frac{2\kappa^2 E}{e^4} \propto E \tag{4.6}$$

Therefore the Coulomb gap depends linearly on energy, with a slope determined solely by physical constants. In contrast the slope of the linear gap in our data depends inversely on field strength with an offset, suggesting that a simple Coulomb gap is inadequate in explaining the tunneling suppression in our experiment.

In tunneling experiments, there must be a nearby electrode to supply the tunneling electrons. This electrode screens the interactions in the 2DEG, rendering the interaction among the electrons dipolar. Pikus and Efros [25] showed that even for dipolar interactions, the gap in the single-particle DOS would survive for a classical disordered system of particles. However there are no predictions that the gap remains linear at low energies with its slope inversely proportional to magnetic field, as observed in our experiment. In order to explain our data, we approach the tunneling problem from a different viewpoint in which we directly incorporate the effect of screening instead of treating it as a perturbation. This model will be the subject of the next section.

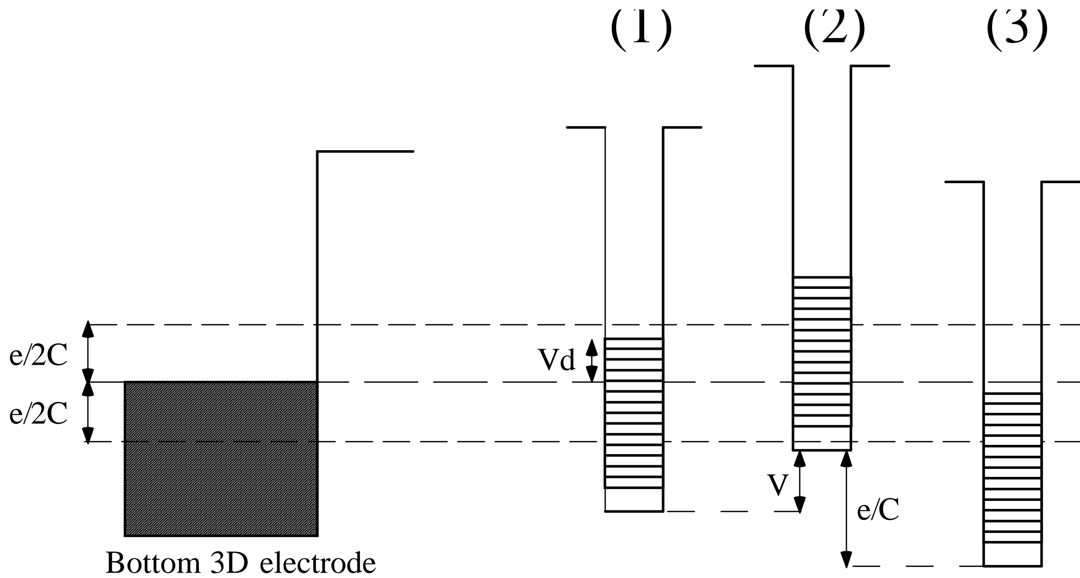

Figure 4-11: Energy diagram of the charge transfer process from the 3D electrode to a single puddle. (1) Zero applied voltage. Fermi energies of the 3D electrode and the puddle equilibrates to within e^2/C. V_d is the accidental separation of the two Fermi energies due to disordered background potential. (2) Application of a voltage step V rises the Fermi level of the puddle above the Coulomb threshold. (3) Electron tunnels to the 3D electrode and electrostatic potential of the puddle drops by e/C.

4.5 Coulomb Blockade Gap

While no existing theory explains our results, the main features of our data are consistent with predictions from a simple phenomenological model. This model is inspired by one previously developed for tunneling into a system of random sized metal particles [39]. In this picture, we model the 2D system as isolated puddles with uniform charging energies and random background offsets. Interactions among the puddles are neglected, in contrast to the Coulomb gap model. This assumption may be justified due to the presence of the nearby 3D conducting substrate which screens the interactions among the puddles.

Even with no applied voltage, the Fermi level of each puddle will not, in general, align with the Fermi level of the 3D bottom electrode. The energy of a puddle with capacitance C increases or decreases by e^2/C when an electron is added to or removed from the puddle. Thus the Fermi energies on the two sides of the tunnel

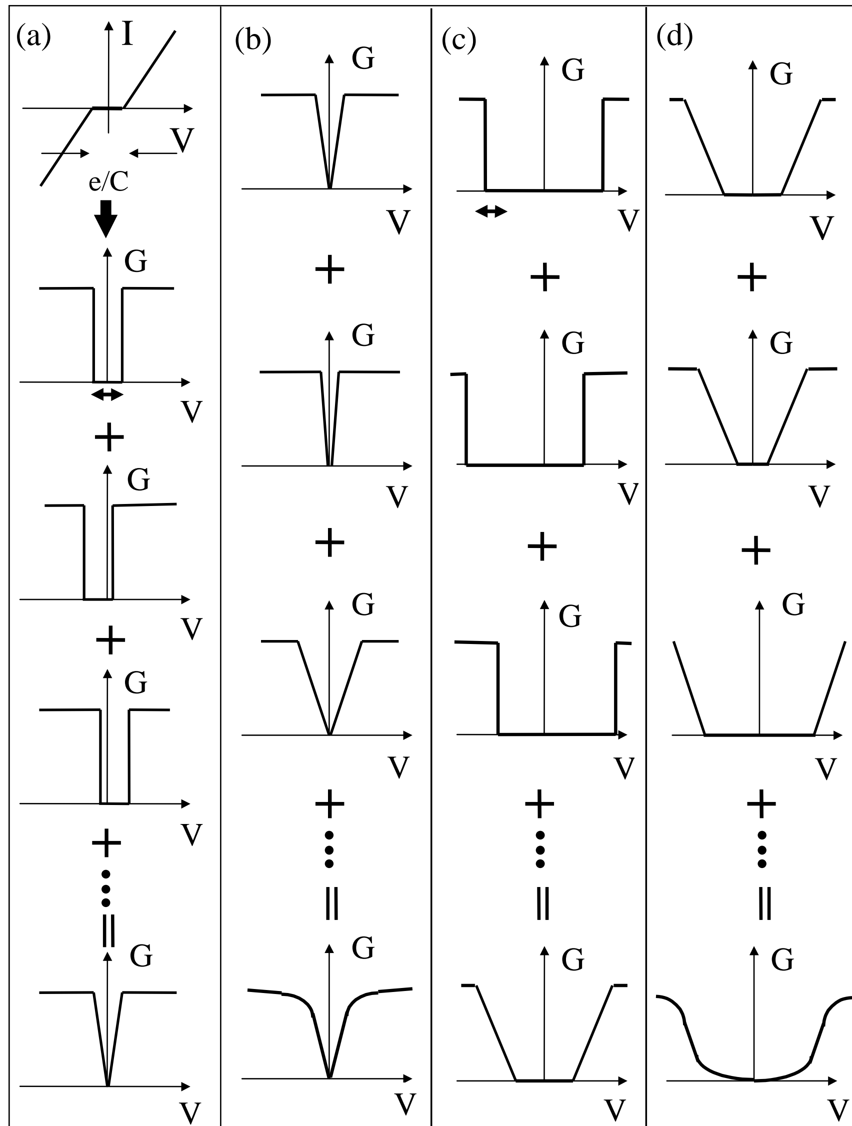

Figure 4-12: (a) From the top: I-V curve and the corresponding conductance curve of a single puddle. A random background voltage shifts the conductance curves along the voltage axis. The bottom figure shows the V-shape conductance curve resulting from summations of these randomly shifted conductance curves. (b) Puddles of different sizes produce conductance curves with different slopes, giving rise to an overall conductance curve shown at the bottom. (c) When the puddles becomes so small such that e/C becomes larger than the background offset voltage, the overall conductance will vanish near zero bias. (d) In this regime, when we take puddles of different sizes into account, the resultant conductance curve is U-shaped.

barrier are only equilibrated to within e^2/C of each other. The Fermi energies in these puddles are assumed to be uniformly distributed within this range due to, for instance, a random background voltage offset created by nearby dopants or impurities. Each puddle contributes a Coulomb blockade type I-V characteristic, leading to a conductance curve which is constant in voltage except for a region of width $e/2C$ randomly displaced from zero bias where the conductance vanishes (Fig. 4-12a).

To obtain the tunneling conductance into the whole system, we simply add the tunneling conductance of all puddles. As shown in Fig. 4-12b, summation of conductance curves from puddles with different voltage offsets generates a resultant conductance curve that is linear in voltage near zero bias. The slope of this linear gap is proportional to the capacitance C, while the width of the gap is inversely proportional to C. Since the capacitance C is proportional to the size of the puddles, our data can be explained if the average area of a puddle varies inversely with magnetic field strength. This model assumes that the high voltage conductance of an individual puddle is proportional to its area and the total area occupied by puddles is constant.

Another appealing feature of this "Coulomb blockade gap" model is that it can explain the different curvatures of the tunneling spectrum at high excitations and the negative offset of the slope vs. inverse field strength dependence shown in Fig. 4-6. When we take puddles of different sizes into account, the resultant DOS will be a superposition of linear gaps with different widths, preserving the linear behavior at zero bias but allowing for curvature at high excitations. In the limit when the range of random energy offsets is larger than the Coulomb blockade energy, puddles of various sizes all produce V-shaped conductance curves, albeit with different widths and slopes. Figure 4-12b shows that superposition of contributions from puddles of different sizes results in a conductance curve that is convex (negative curvature) in high excitation voltages while the V-shaped (linear) singular behavior is maintained near zero bias, as identified with our low field data.

When some of the puddles are so small that their Coulomb blockade energies exceed the range of the background offset energy, their conductance curve will no longer be V-shaped. In this regime, conductance contributions from puddles of a

particular size will have zero conductance at low bias up to a certain voltage beyond which the overall conductance rises linearly with voltage to the unsuppressed value, as depicted in Fig. 4-12c. Summing contributions for puddles of various sizes leads to the U-shape conductance curve in Fig. 4-12d, concave with respect to voltage at high biases. As long as there exist some puddles large enough with a V-shape conductance curve, the linear behavior of the overall conductance is preserved near zero bias, although with a much reduced slope.

We can carry this argument further to explain the finite magnetic field required to produce a zero slope in the DOS as extrapolated from our TDCS data. This happens when the puddles are small enough so that the Coulomb blockade energy of every puddle in the system exceeds the range of the background offset energies. It is not necessary to have an infinitely small puddle to achieve a zero slope for conductance near zero bias. This explains the non-zero intercepts on the horizontal axes if one extrapolates the data points in Figs. 4-6 and 4-8.

The above deductions are based on the assumption that larger puddles break up into smaller ones and that the mean area of the puddles shrinks linearly with increasing field strength. Electrons therefore charge parallel plate capacitors whose lateral dimension is proportional to the magnetic length. From the width of the gap in our data, we estimate that this proportionality constant is about 5. We do not yet have a clear answer to the question of what the puddles are and why they shrink as the magnetic field strength is increased.

While this simple picture of a Coulomb blockade gap may not provide a complete description of the system, it seems to be able to explain qualitatively most features in our data. A more thorough understanding of the tunneling suppression will require inclusion of interaction, charging effects and the quantum mechanical properties of the 2D electron system.

4.6 Conclusion

In this chapter, we studied the suppression of tunneling conductance by a magnetic field applied perpendicular to the 2D plane. We find that the tunneling conductance depends linearly on excitation voltage near zero bias for all electron densities and field strengths. The slope of this linear gap decreases as the magnetic field is increased. We proposed an interpretation of this behavior using a "Coulomb blockade gap" model which seems to capture most features in our data.

Chapter 5

Tunneling into Ferromagnetic Quantum Hall States: Observation of a Spin Bottleneck

The interplay between Zeeman coupling of electronic spins to an applied magnetic field and Coulomb interactions among electrons leads to remarkable spin configurations of quantum Hall systems. For instance, around quantum Hall filling factor $\nu = 1$, powerful exchange interactions align electron spins to form a nearly perfect ferromagnet [2]. Theorists predict that the elementary charge excitations of this $\nu = 1$ quantum Hall state consist of spin textures known as Skyrmions [3, 4]. The small value of the Zeeman energy compared to the Coulomb energy in GaAs gives rise to the appropriate conditions for the formation of Skyrmions.

In Chapters 3 and 4, we demonstrated the capability of tunneling experiments to probe electron-electron interactions. Given the measured and predicted richness of the spin properties of quantum Hall systems, we decided to explore whether tunneling could also prove useful for revealing effects of electronic spins [40]. Such study should be most interesting for the ferromagnetic quantum Hall states, but experimental data for tunneling in these regimes have been limited. The major obstacle is that the in-plane conductance of the 2D system drops to near zero around $\nu = 1$. As a result the tunneling charge cannot be collected and measured via conduction in the 2D plane, as

we discussed in Chapter 2. It is possible to use capacitance techniques to circumvent this problem [19, 20, 32]. However, complete characterization involves time-resolved measurements described here or measurements over broad frequency range that have not been previously performed on high mobility samples.

In this Chapter, we describe measurements of tunneling from a 3D electrode into a high mobility 2D electron system in a GaAs/AlGaAs heterostructure at $\nu = 1$. Using time domain capacitance spectroscopy (TDCS) that we described in Chapter 2, we detect the tunneling current into both localized and delocalized states. Here, we focus on the effects of electronic spins on tunneling by detecting the equilibrium tunneling of electrons in real time, instead of studying the tunneling pseudogap through measurement of non-linear I-V curves, as we discussed in Chapters 3 and 4. While it is well-known that Coulomb interaction of electrons suppresses tunneling near the Fermi energy, we have discovered that non-equilibrium spin accumulation also leads to a reduction of tunneling rates into spin-polarized quantum Hall states. We observe that the process of electron tunneling into ferromagnetic quantum Hall states differs qualitatively from tunneling into other filling fractions: electrons tunnel into ferromagnetic quantum Hall states at two distinct rates. Some electrons tunnel into the 2D system at a fast rate while the rest tunnel at a rate up to 2 orders of magnitude slower. We observe such novel double-rate tunneling only in spin-polarized quantum Hall states ($\nu = 1$, 3 and $\leq 1/3$) in samples of highest mobility. This effect does not appear at even-integer filling fractions. Our detailed study of the dependence of the two rates on temperature, magnetic field and tunnel barrier thickness indicates that slow in-plane spin relaxation leads to a bottleneck for tunneling and gives rise to the double tunneling rate phenomenon. To our knowledge, our work is the first experiment to demonstrate the effects of interactions among electronic spins on tunneling into quantum Hall systems.

We begin this chapter by giving an introduction to the ferromagnetic quantum Hall state at $\nu = 1$ and its elementary charge excitations.

5.1 Spin Physics for the $\nu = 1$ Ferromagnetic State

For electrons in free space, the cyclotron energy ($\hbar\omega_c$) and the Zeeman energy ($-g\mu_B B$) have the same magnitude in an applied magnetic field B, where $\omega_c = eB/m_e c$ is the cyclotron frequency, $\mu_B = e\hbar/2m_e c$ is the Bohr magneton, m_e is the rest mass of the electron and the g-factor has a value of 2. In GaAs, the Zeeman energy is much smaller than the cyclotron energy for two reasons. First, the effective mass for electrons in GaAs is about 15 times smaller the bare electron mass, hence increasing the cyclotron energy by the same factor. At the same time, spin-orbit interactions in GaAs modify the g-factor to a value of -0.44, further diminishing the Zeeman energy compared to the cyclotron energy. As a result of these two effects, the Zeeman energy in GaAs is 70 times smaller than the cyclotron energy.

As we described in Chapter 1, the density of states of a 2DEG in a perpendicular magnetic field consists of highly degenerate Landau levels separated by energy gaps. At filling factor $\nu = 1$, only the lowest spin-split Landau level is filled with electrons. Even for non-interacting electrons, one would expect a disorder-free 2D system to be spin-polarized. However, this reasoning is actually misleading because the $\nu = 1$ state is a highly correlated state, and the dominant energy at $\nu = 1$ is not the Zeeman energy but the Coulomb energy among electrons. It is the Coulomb exchange energy that is responsible for aligning the spins. For instance, in GaAs the Coulomb energy $e^2/\kappa l_B$ (where κ is the dielectric constant and l_B is the magnetic length) at a magnetic field of 5T is $\sim$80 times larger than the Zeeman energy. At $\nu = 1$, electrons gain exchange energy by aligning their spins and the 2D system develops spontaneous ferromagnetic order. Interaction effects among electrons significantly enhance the energy gap at $\nu = 1$ from the single-particle Zeeman energy. In fact, there have been theoretical predictions that the $\nu = 1$ quantum Hall state will survive even in the absence of the Zeeman interaction [3]. Experiments have verified this by tuning the g-factor of GaAs to zero through application of hydrostatic pressure to the sample [41, 42, 43].

Recently there have been substantial interest in the elementary excitations of

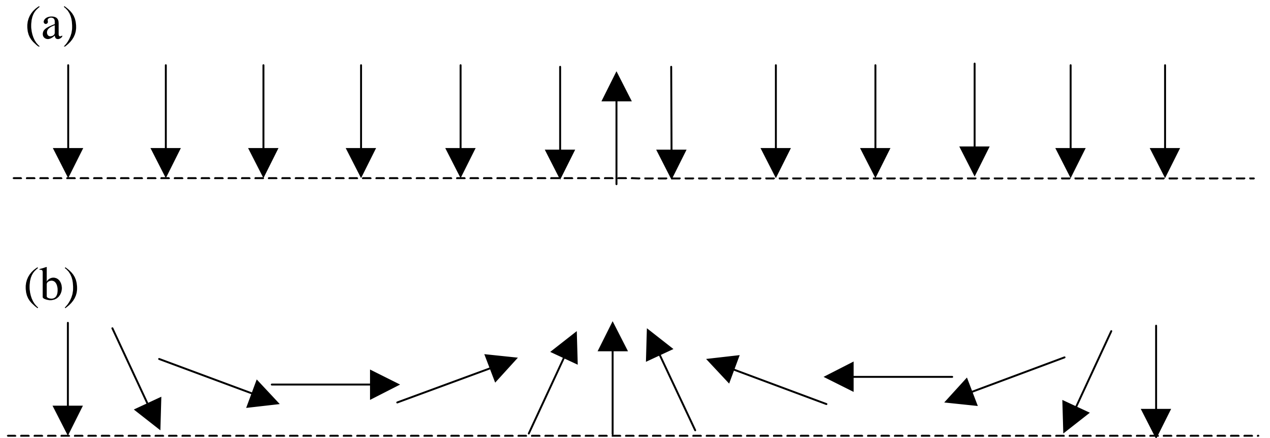

Figure 5-1: (a) An ordinary charge excitation for a filled spin-split Landau level consists of a single flipped minority spin. (b) When the Zeeman energy is small compared to the Coulomb exchange energy, the lowest energy charge excitation contains spin texture known as Skyrmions. Skyrmions consist of a radial spin distribution that is reversed at the center and gradually heals to the spin background. This saves on exchange energy because neighboring spins are almost aligned.

this $\nu = 1$ ferromagnetic state. Theorists [3, 4] predict that the lowest energy charge excitations at $\nu = 1$ consist of spin textures known as Skyrmions. It is again the small value of the Zeeman energy compared to Coulomb energy in GaAs that gives rise to the appropriate conditions for the formation of Skyrmions. We give a qualitative picture of Skyrmions for the $\nu = 1$ ferromagnetic quantum Hall state below.

At $\nu = 1$, the lowest Landau level is occupied by electrons with a single spin orientation. A naive way to create a charge excitation is to introduce a minority up-spin (Fig. 5-1a). This costs a considerable amount exchange energy because the spin of the extra electron is opposite to its neighbors. The system can save more energy by creating excitations that contain spin texture. In Fig. 5-1b the spin of electrons gradually changes from up in the middle to down at the periphery. By doing this, the system obviously has to pay extra Zeeman energy because more than one spin is flipped but since adjacent spins are almost aligned, this saves on the exchange energy. It is the competition between Zeeman and Coulomb energy that determines how many spins are flipped and the size of a Skyrmion excitation. In a system with

zero Zeeman energy, Skyrmions will be infinite in size. For finite Zeeman energy, Skyrmions have a certain size that is characterized by the number of reversed spins.

So far experimental results supporting the Skyrmion picture at $\nu = 1$ comes from three types of measurements. The earliest evidence involves measurement of the spin polarization of the 2DEG around $\nu = 1$. Nuclear spin resonance [44] and magneto-optical absorption experiments [45] have shown that the spin polarization of 2D electrons attains a maximum at $\nu = 1$ and falls off sharply on either side. Such observation is consistent with the notion that Skyrmions contain multiple flipped spins as described above. This rapid loss of spin polarization away from $\nu = 1$ provides the strongest evidence for the existence of Skyrmions.

Another type of experiment utilizes thermally activated transport to measure the energy gap for creating quasiparticles at $\nu = 1$. The objective of these experiments is to deduce the number of flipped spins that a quasiparticle carries by varying the Zeeman energy while keeping the exchange energy constant. Schmeller *et al.* [46] adjust the Zeeman energy through changing the component of magnetic field parallel to the 2D plane. The component of magnetic field perpendicular to the 2D plane is kept constant to maintain the exchange energy at fixed value. In a different experiment, Maude *et al.* [41] vary the Zeeman energy by tuning the g-factor through application of hydrostatic pressure to the sample. The third kind of experiment providing support for the Skyrmion picture involves heat capacity experiments [47, 48] which produced results consistent with the notion that Skyrmions crystallize into a regular lattice at filling factors slightly away from $\nu = 1$.

In this Chapter, we describe evidence of Skyrmion effects on tunneling into the $\nu = 1$ quantum Hall state. Tunneling experiments offer another approach for studying the effects of Skyrmions, independent of the various measurement techniques described above. We will demonstrate the capability of tunneling measurements in revealing the interactions among electron spins.

5.2 Samples

In this chapter, we will describe data from very high mobility samples grown by L. N. Pffeifer and K. W. West at Bell Laboratory. One of the reasons for the improvement in mobility compared to samples we measured in Chapters 3 and 4 is the modification in sample design described below.

Most GaAs heterostructures used to study the quantum Hall effect are modulation doped. In these samples there are dopants in the AlGaAs regions to provide electrons for the quantum well. Since the dopants are physically separated from the 2D electrons, modulation doping improves the sample mobility considerably. The fractional quantum Hall effect was first observed by Tsui, Stormer and Gossard [49] on such samples. These remote dopants nevertheless remain the major source of disorder.

In our new design, we eliminate this modulation doping. We can remove the dopants in AlGaAs without suffering from dramatic reduction of 2D electron density because electrons in the quantum well can be provided by the bottom 3D electrode when we apply a positive voltage on the top gate to attract electrons into the quantum well. Dopants still exist in our structure in the top and bottom n-doped GaAs electrodes. However, these dopants are surrounded by conduction electrons and are very effectively screened. Since we do not have ohmic contacts to our 2DEG, we cannot measure its mobility directly. Nevertheless, regular modulation doped samples by grown by Pffeifer and West consistently achieve mobilities of larger than $10^6 cm^2 V^{-1} s^{-1}$. We expect our samples to have even higher mobility due to the complete absence of unscreened silicon dopants in AlGaAs.

In this chapter, we will present data from four such samples with very high mobility. Apart from differences in tunnel barrier composition and thickness, the samples have essentially the same structure shown in Fig. 5-2a. The following sequence of layers is grown on n+ GaAs substrate: 6000 $\mathring{A}$ n+ GaAs, 300 $\mathring{A}$ GaAs spacer layer, AlGaAs/GaAs tunnel barrier, 175 $\mathring{A}$ GaAs quantum well, 700 $\mathring{A}$ AlGaAs (undoped) blocking barrier and 1.3 μm n+ GaAs cap layer. Samples p040297 and p092696 have AlGaAs/GaAs superlattice tunnel barriers of thickness 193 $\mathring{A}$ and 147 $\mathring{A}$ respectively.

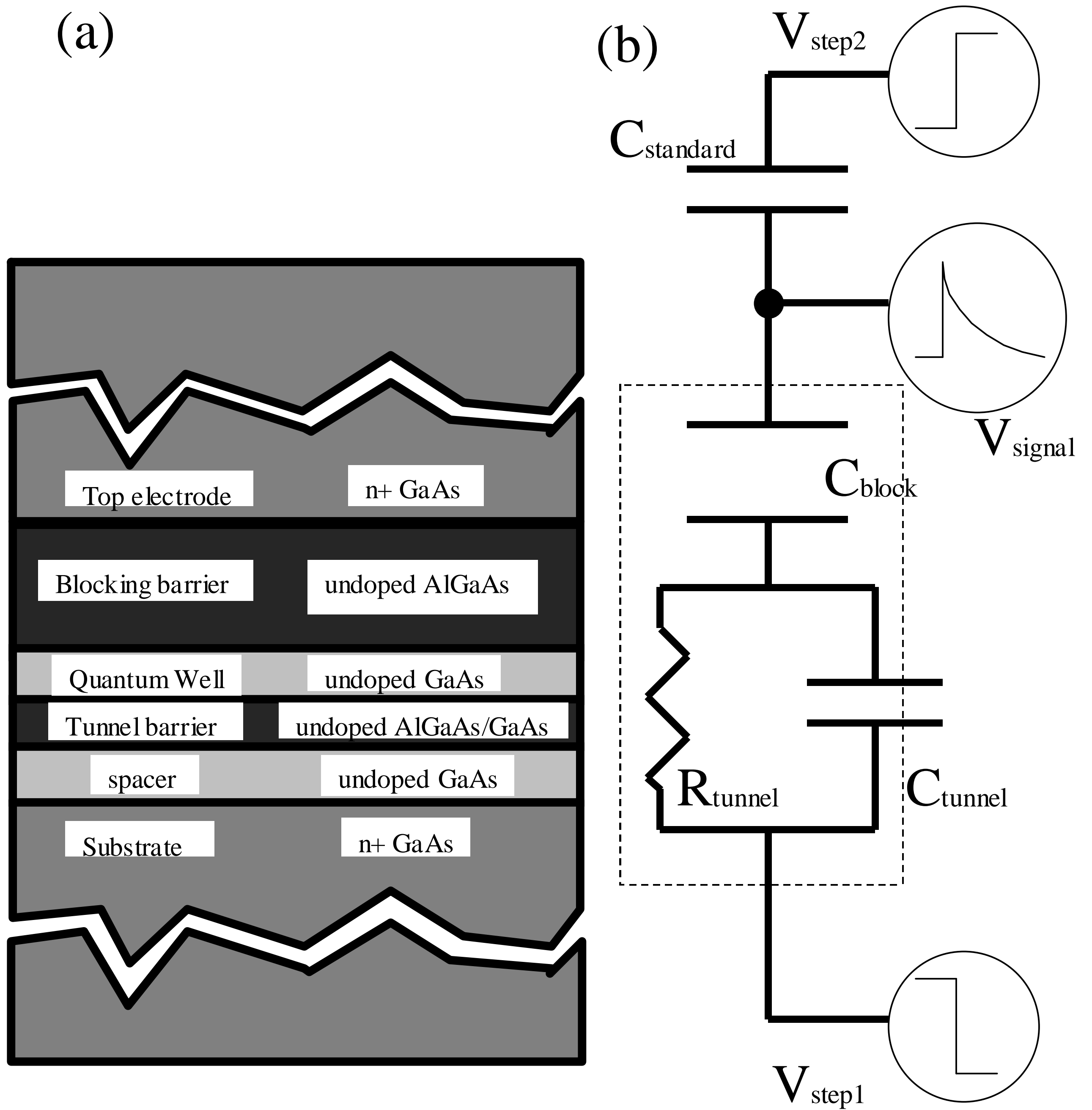

Figure 5-2: (a) The essential layer structure of the high mobility samples. (b) External circuit used to measure R_{tunnel}. The sample can be modeled by linear circuit elements (inside the dotted box) when the excitation voltage is smaller than kT.

For samples p031798 and p061998a, the tunnel barriers are made of 147 $\AA$ and 130 $\AA$ AlGaAs respectively. We performed our measurements on circular mesas with diameters of 300 μm for all four samples.

Appendix C describes the fabrication process for the samples.

5.3 Equilibrium Tunneling at $\nu = 1$

In Chapter 2 we described measurements of the single-particle density of states using "time domain capacitance spectroscopy" (TDCS). We use the same technique to study the high mobility samples. Figure 5-3 illustrates that in a magnetic field the tunneling conductance depends linearly on excitation voltage, similar to the behavior of the more disordered samples in Chapter 4. In this Chapter, we focus on "zero-bias" tunneling into the 2DEG measured by applying excitation voltages smaller than kT. The lowest temperature at which we took our data is about 60 mK. This corresponds to an excitation voltage of approximately $7\mu V$, which is a factor of 1000 smaller compared to the voltage axis in Fig 5-3. We therefore perform the measurement essentially at the bottom point of the linear energy gap. By keeping the chemical potential on the two sides of the tunnel barrier within kT of each other, we are not affected by non-linear or non-ohmic behavior of the I-V curves.

In this equilibrium tunneling regime [19, 20], we model the tunnel barrier by a capacitor C_{tunnel} shunted by a resistor R_{tunnel}, while a capacitor C_{block} represents the blocking barrier (Fig. 5-2b). Figure 5-2b also shows the capacitance bridge used to measure R_{tunnel}. Voltage steps of opposite polarity are applied to the top electrode of the sample and to one plate of a standard capacitor C_S. The other plate of C_S and the bottom electrode of the sample are electrically connected, and the voltage V_b at this balance point is amplified and recorded as a function of time. When the excitation voltage amplitude is smaller than kT, the tunneling resistance R_{tunnel} is independent of excitation voltage across the tunnel barrier. The equivalent circuit of the bridge consists of linear circuit elements and therefore we expect V_b to decay exponentially.

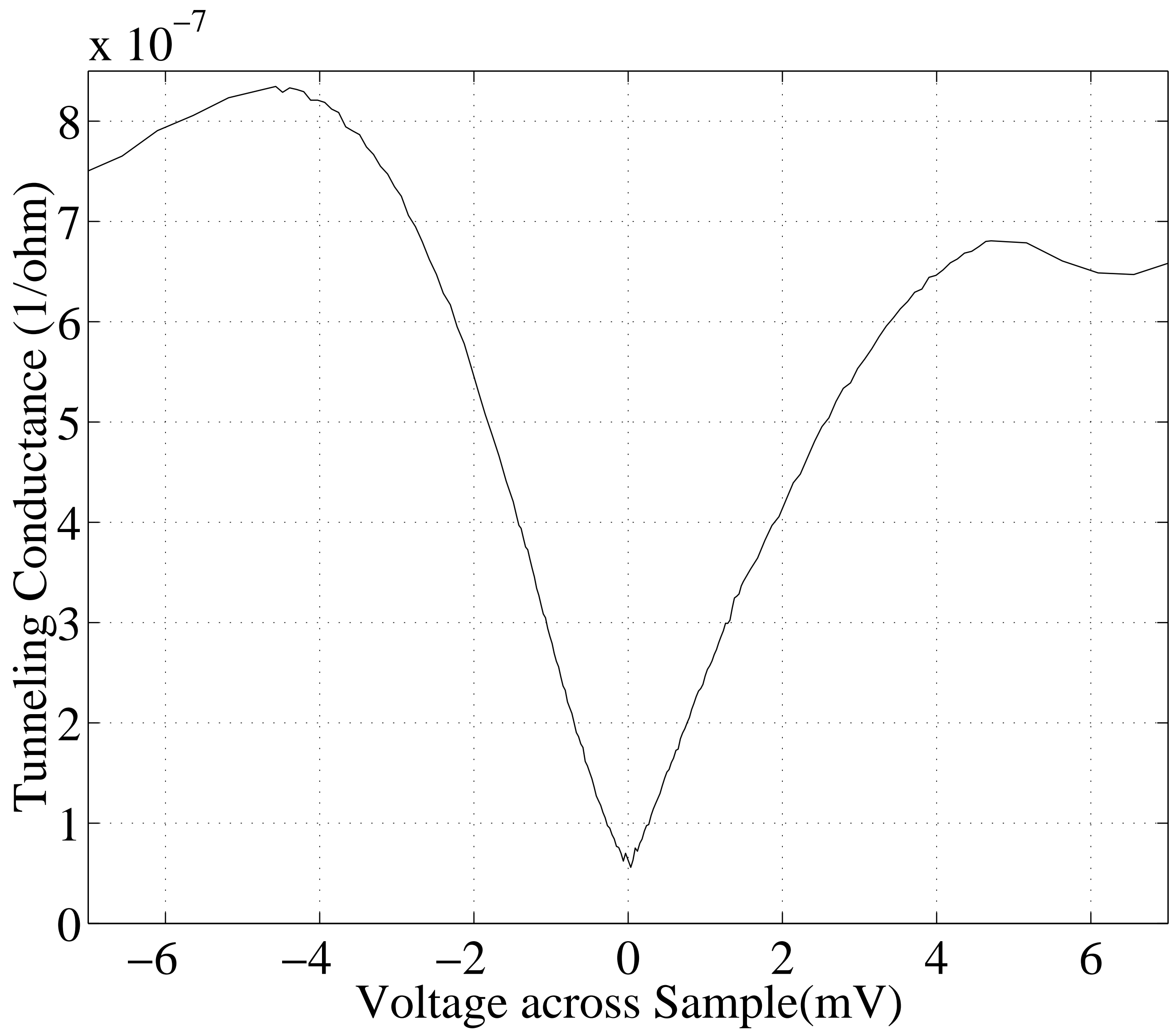

Figure 5-3: Linear dependence of the tunneling conductance on excitation voltage in a magnetic field of 1.5T for sample p031798. The filling factor is about 0.87.

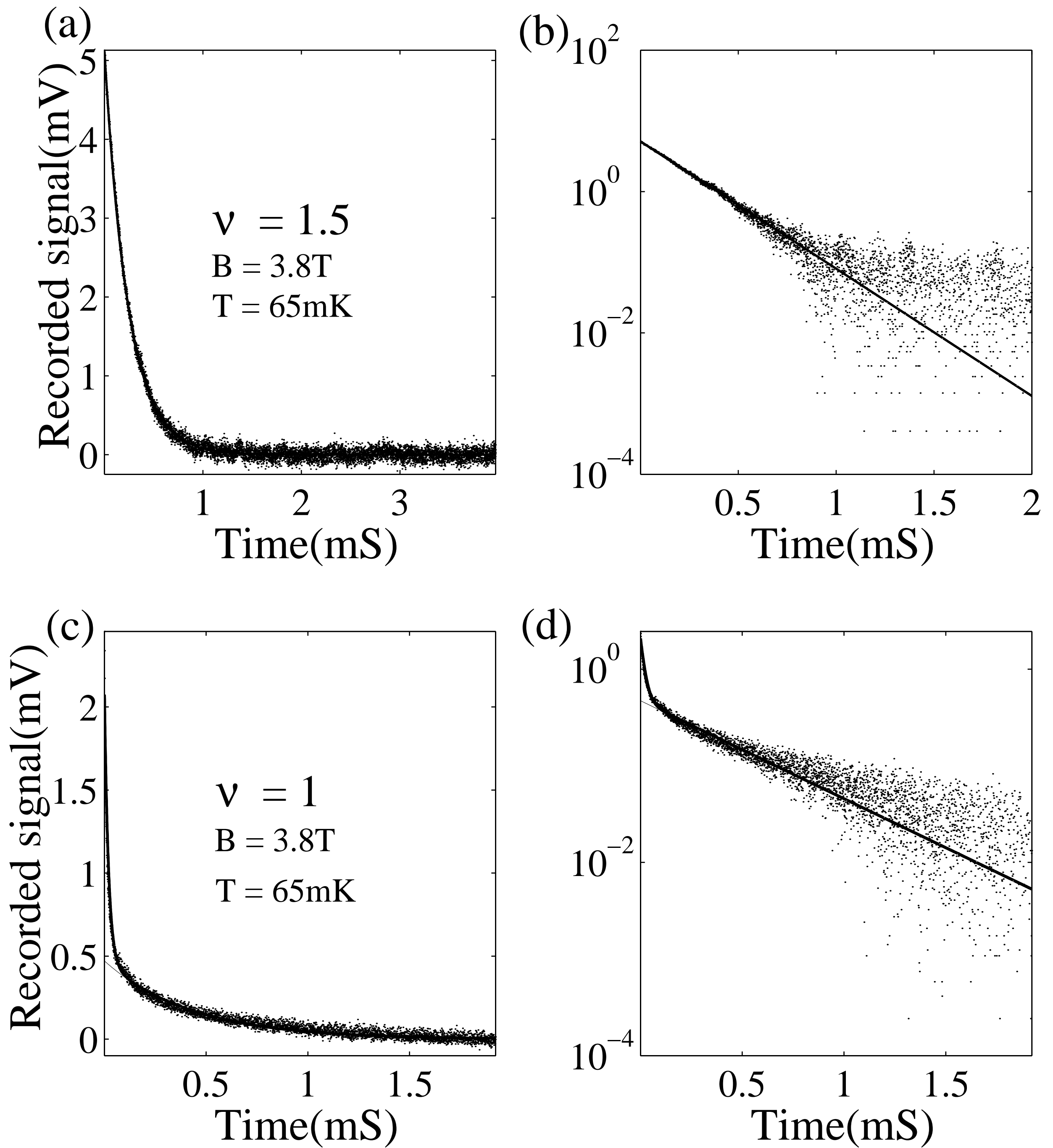

Figure 5-4: (a) Recorded signal decays exponentially at $\nu = 1.5$. (b) Same signal on a semilog scale. The line is an exponential fit to the data. (c) Recorded signal is non-exponential at $\nu = 1$. (d) Signal at $\nu = 1$ on a semilog scale. The thin line is an exponential fit to the slow decaying part of the time trace. The thick line is a fit to the data using Eq. 5.1.

Figures 5-4a and b plot the recorded voltage on linear and logarithmic vertical scales as a function of time at $\nu = 1.5$ and a field of 3.8 T. The signal decays exponentially for more than 2 orders of magnitude. In general, we observe such agreement with an exponential decay when ν is close to half integer. This indicates that for filling factors at which the 2DEG is compressible, electrons tunnel into the 2DEG at a single rate and the equivalent circuit model in Fig. 5-2 adequately describes the sample. Figures 5-4c and d show a drastically different recorded signal at $\nu = 1$. The decay is clearly non-exponential. We can fit it well with a sum of two exponential decays with different time constants (τ_1, τ_2) and prefactors (A_1, A_2):

$$V(t) = A_1 exp(-t/\tau_1) + A_2 exp(-t/\tau_2) \tag{5.1}$$

as shown in Figs. 5-4c and d. In other words, at $\nu = 1$ electrons tunnel from the 3D electrode into the 2DEG at two distinct rates. Some electrons tunnel at a fast rate while the rest tunnel at a significantly slower rate.

We emphasize that the measurement is performed by applying excitation voltage across the tunnel barrier (8.9 μV) comparable to the temperature (65 mK) and is therefore in the linear response limit of R_{tunnel}. This eliminates the possibility that the non-exponential relaxation at $\nu = 1$ is due to an excitation voltage-dependent R_{tunnel} caused by the magnetic field induced energy gap in tunneling [15, 19, 20, 21, 32] described in Chapter 4. To further verify that tunneling occurs in the linear response limit, we reduce the amplitude of the excitation voltage by 50%. The corresponding signal, apart from a reduction in magnitude by a factor of two, is identical to the original signal that is made up of a sum of two exponential decays with distinct time constants.

Figure 5-5 shows the dependence of relaxation rates on gate voltage for sample p061998a at a fixed magnetic field of 3.8 T. We change the filling factor by increasing the gate voltage to attract electrons from the 3D substrate into the quantum well. At each gate voltage in Fig. 5-5, we record a time trace similar to the ones in Fig. 5-4. For gate voltages at which we can fit the time trace by a single exponential decay as in

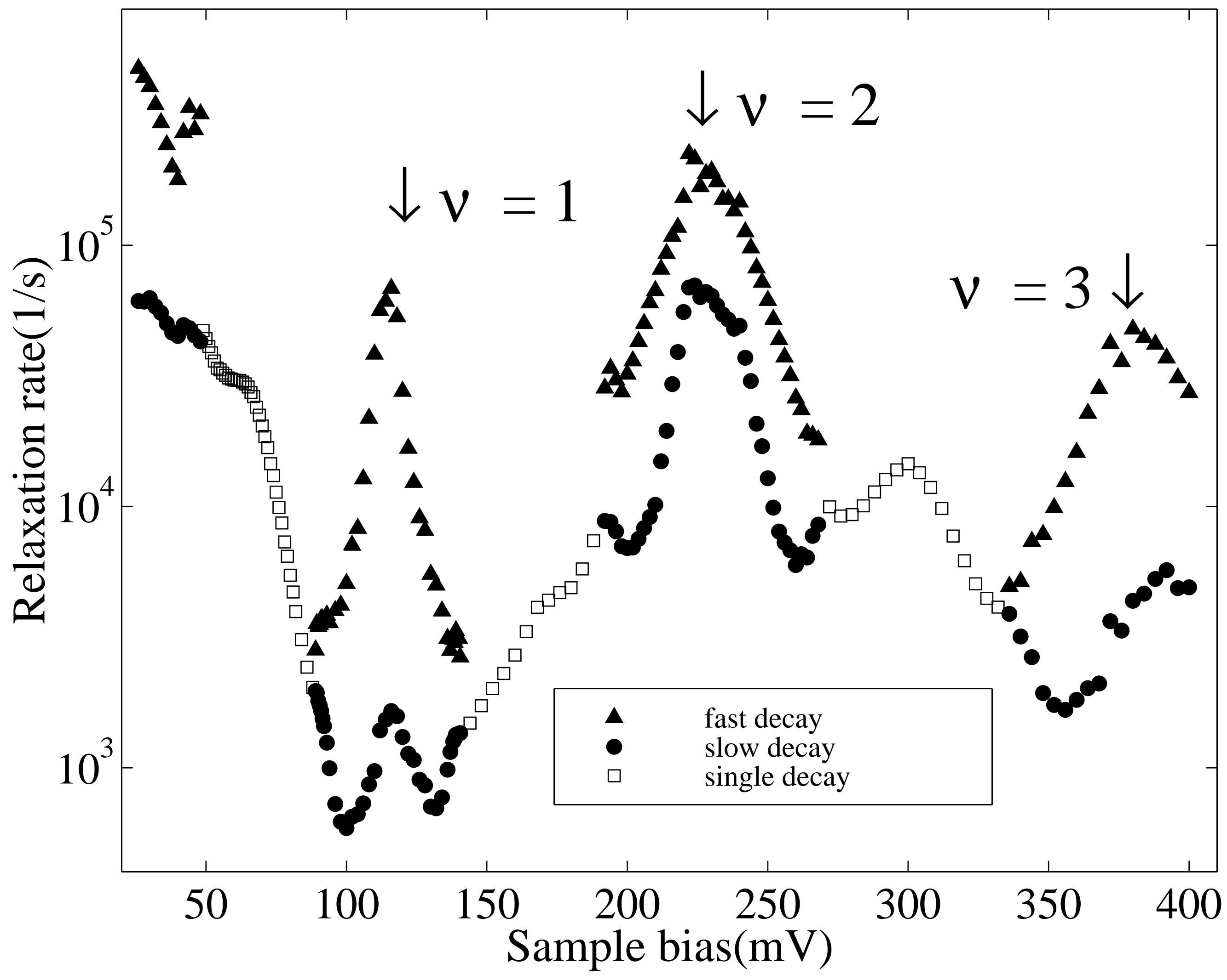

Figure 5-5: Dependence of the relaxation rate of the exponential decay on sample bias for sample p061998a at 3.8 T and 65 mK.

Figs. 5-4a and b, we plot the relaxation rate as a hollow square. When it is necessary to use a sum of two exponential decays (Eq. 5.1) to fit the signal as in Fig. 5-4c and d, filled triangles and circles represent the corresponding fast and slow relaxation rates ($1/\tau_1$ and $1/\tau_2$) obtained respectively. Figure 5-5 indicates that tunneling occurs at two distinct rates near integer Landau level filling factors, while electrons tunnel at a single rate when the 2DEG is compressible near half integer fillings.

5.4 Sample Inhomogeneity: Comparison between Tunneling at $\nu = 1$ and $\nu = 2$

At integer filling factors, the in-plane conductance vanishes as the electronic states at the chemical potential become localized. Inhomogeneity, such as monolayer fluctuations in the tunnel barrier thickness, gives rise to non-uniform tunneling rates into different lateral positions of the 2D plane. In Fig. 5-5, the two relaxation rates at $\nu = 2$ differ approximately by a factor of three and can be explained well by this argument. In contrast, the fast and slow relaxation rates at $\nu = 1$ differ by about a factor of 60. Relaxation rate differences of such magnitude cannot be explained by fluctuations in the tunnel barrier thickness. Moreover, it is unlikely that the 2DEG is more inhomogeneous at $\nu = 1$ than at $\nu = 2$. The ratio between the two relaxation rates also behaves differently around ν =1 and $\nu = 2$ as ν deviates from exact integer value. In Fig. 5-5, the ratio of the two rates remains almost constant around $\nu = 2$. On the other hand, this ratio increases as ν approaches 1, attaining a peak value of 60 at $\nu = 1$.

Figure 5-6 illustrates the difference between a time trace at $\nu = 1$ and $\nu = 2$. Both traces decay at a comparable rate initially (with time constants ~ 10 μSec), whereas only the $\nu = 1$ signal contains an additional slower decaying component with a time constant of about 600 μSec.

We note that the applied magnetic field suppresses the relaxation rates in Fig. 5-5 by as much as 4 orders of magnitude. With the magnetic field turned off, the

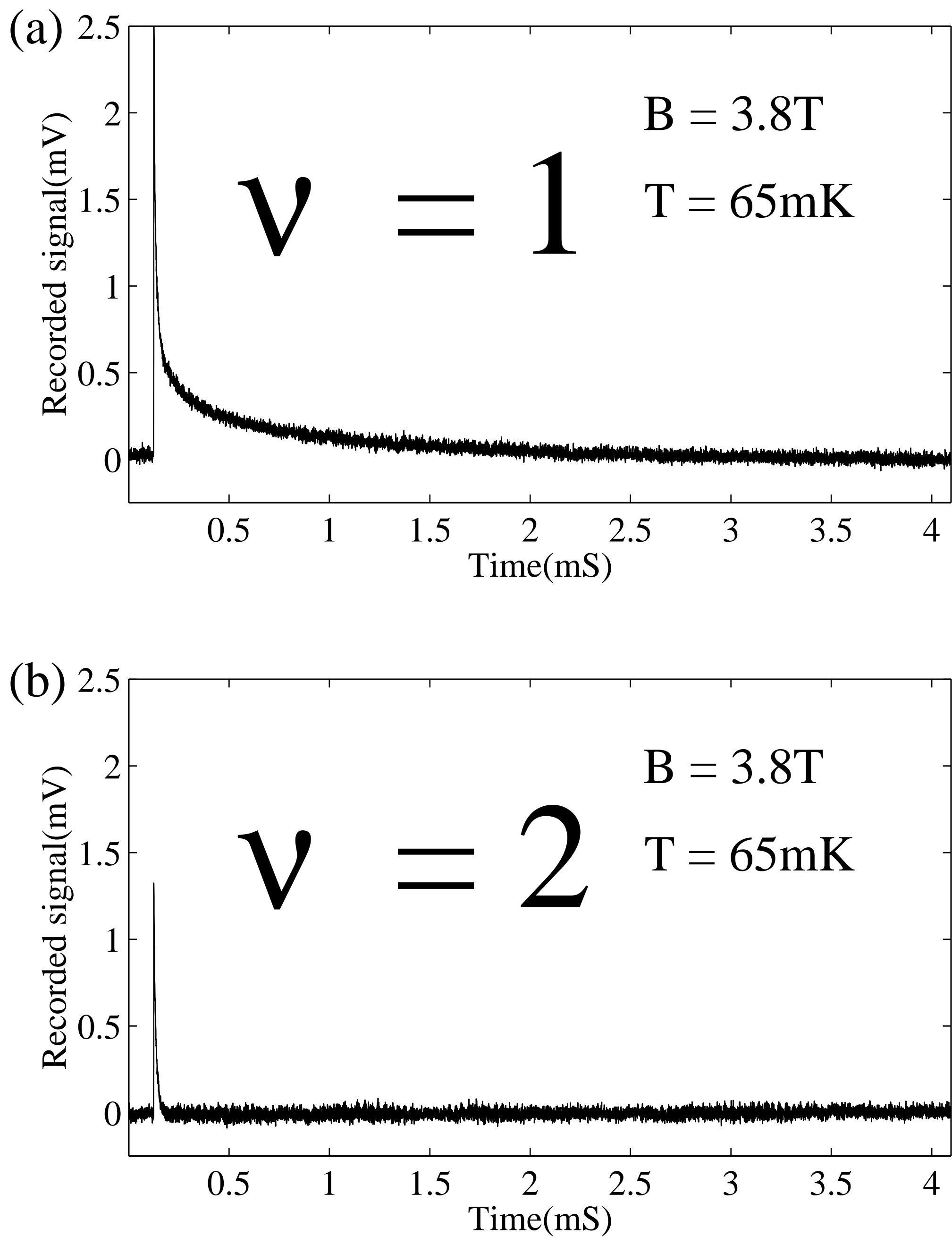

Figure 5-6: (a) Recorded signal at $\nu = 1$ contains a slow decay with time constant $\sim 600\mu s$ in addition to initial fast decay with time constant $\sim 10\mu s$. (b) Recorded signal at $\nu = 2$ does not have the slow decay component.

tunneling rate into the 2DEG in this sample is too fast for our range of detection. It is also noteworthy that the tunneling suppression increases in strength toward $\nu = 1$ while it is weakest for the localized states at $\nu = 2$. In this chapter, we focus on the double relaxation rate phenomenon at $\nu = 1$, which, unlike at $\nu = 2$, cannot be trivially explained by inhomogeneity of the sample.

5.5 Tunneling of Spin-up and Spin-down Electrons

The $\nu = 1$ and $\nu = 2$ quantum Hall states have the common characteristic that an energy gap exists at the chemical potential, albeit of different origins. At $\nu = 2$, the cyclotron gap arises from the effect of the magnetic field on the orbital motion of the electrons and is present even for a non-interacting 2D electron system. On the other hand, the existence of an energy gap at $\nu = 1$ is a many body phenomenon. The interactions among electrons lead to ferromagnetic order and the formation of an exchange energy gap. In our experiment, we measure equilibrium tunneling by applying excitation voltages at least 100 times smaller than the Coulomb energy. In an ideal 2D system without disorder at $\nu = 1$, there are no states at the chemical potential into which electrons can tunnel. Any tunneling current detected must arise from broadening of the Landau levels due to disorder.

Consider a 2D system with inhomogeneous density. When the bulk filling factor is one, regions with local density higher (lower) than the bulk density have filling fraction $\nu > 1$ ($\nu < 1$) into which electrons with minority (majority) spin tunnel, as shown in the middle picture in Fig. 5-7a. To our knowledge, theories do not presently predict that the tunneling rates of electrons with spin up and down are significantly different. While a difference in the tunneling rates for electrons with opposite spins can lead to observation of two relaxation rates in our experiment, we show below that this hypothesis is inadequate to explain our data.

Figure 5-8a plots the relaxation rate as a function of gate voltage at 5.7 T. Analogous to the data at a lower field in Fig. 5-5, tunneling occurs at two distinct rates around $\nu = 1$. In addition to the relaxation rates, we also show the prefactors of

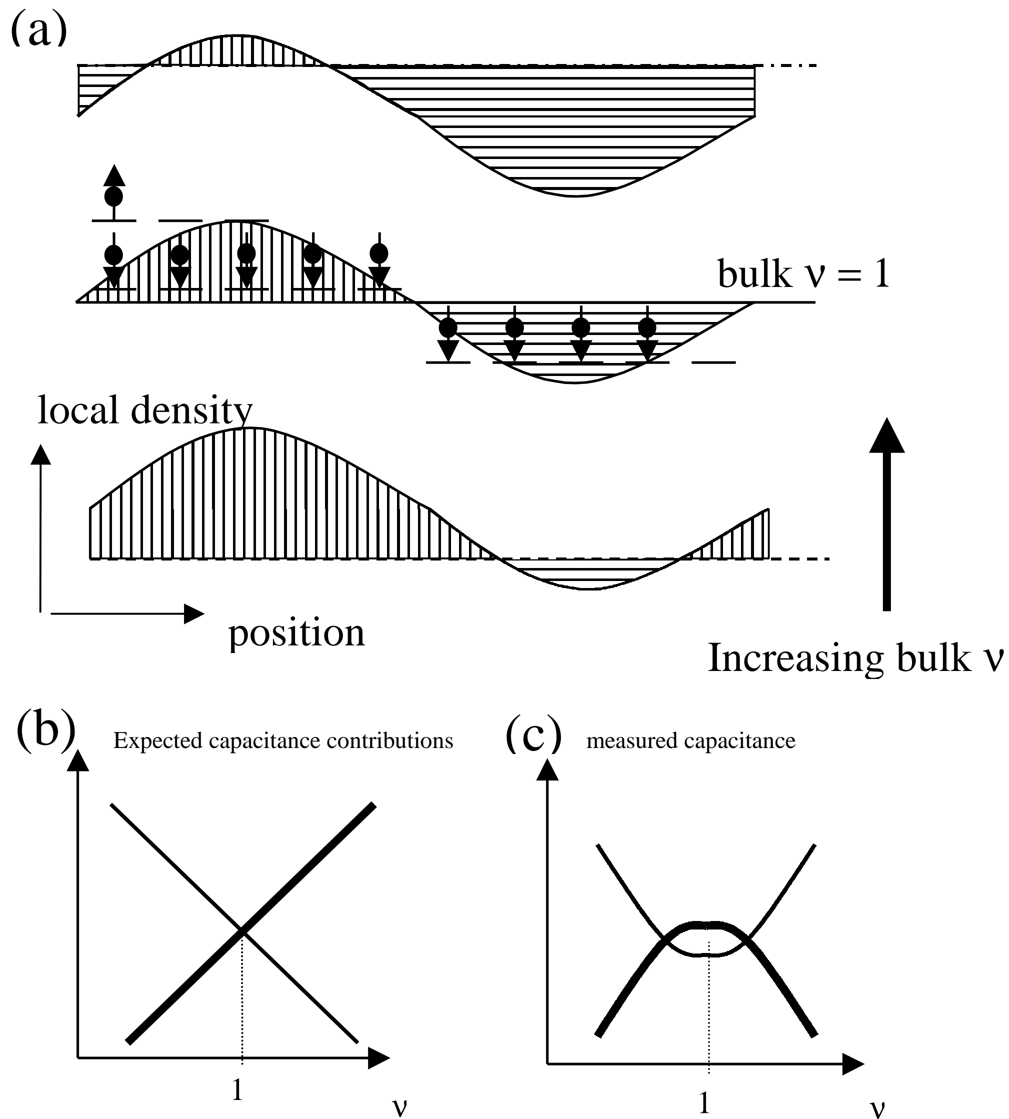

Figure 5-7: This figure illustrates the effect of density inhomogeneity on tunneling at $\nu = 1$. (a) The three diagrams represent the same 2D system with inhomogeneous density at increasing bulk filling factors from bottom to top. Up-spin electrons tunnel into regions with local $\nu > 1$ (shaded by vertical stripes) while down-spin electrons tunnel into regions with local $\nu < 1$ (shaded by horizontal stripes). (b) Expected capacitance contribution for up-spin and down-spin electrons if they tunnel into the 2D system at different rates. (c) Our observed capacitance contribution for the two tunneling rates (also shown in Fig. 5-8b) is inconsistent with this picture.

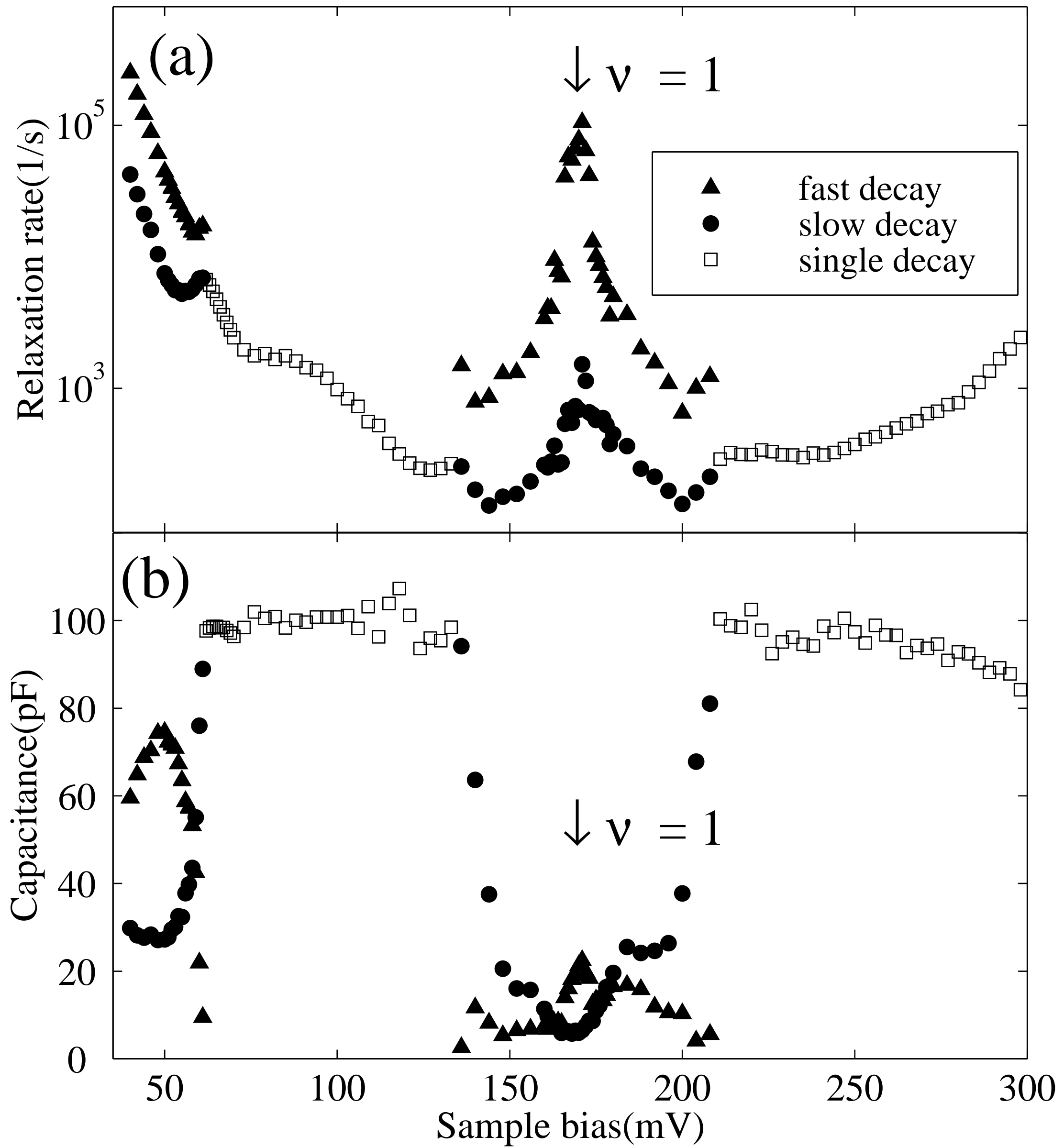

Figure 5-8: (a) Relaxation rate vs. sample bias for sample p061998a at 5.7 T. (b) Sample capacitance charged at the fast and slow rates vs. sample bias. The two capacitance contributions refer to the ratio of the charge tunneling at the fast and slow rates (proportional to A_1 and A_2 respectively in Eq. 5.1) to the constant excitation voltage (9 μV).

the exponential fits (A_1 and A_2 in Eq. 5.1 scaled by a constant factor) in Fig. 5-8b. Around $\nu = 1$, A_1 and A_2 are proportional to the amount of charge tunneling at the fast and slow rates respectively. For the slow decay, the prefactor (plotted as circles) has a minimum at $\nu = 1$ while the prefactor for the fast decay (plotted as triangles) instead has a maximum. Consider a 2D system with inhomogeneous density at bulk filling factor $\nu = 1$. As the bulk density is increased, the fraction of regions with local filling factor $\nu < 1$ decreases monotonically and vice versa for regions with local $\nu > 1$ (Fig. 5-7a). If electrons with majority and minority spins tunnel at different rates, we expect the prefactors of the fast (slow) decay to be an increasing (decreasing) function of bulk density around $\nu = 1$ (Fig. 5-7b), in contrary to Fig. 5-8b. Therefore the observation of two relaxation rates at $\nu = 1$ cannot be trivially explained by a difference in the tunneling rates for electrons with majority and minority spins.

5.6 Energy Scale of the Double-rate Phenomenon

Figure 5-9 shows the temperature dependence of the two relaxation rates at $\nu = 1$ for three magnetic field strengths. At each magnetic field, we adjust the density to maintain the filling factor at $\nu = 1$. Both the slow and fast rates have rather weak temperature dependence at low temperature for all three magnetic fields. The weak temperature dependence of the slow relaxation rate persists up to a temperature beyond which the slow relaxation rate speeds up significantly and the double tunneling rate phenomenon recedes. In other words, electrons tunnel at two distinct rates at $\nu = 1$ only at low temperatures. The onset of strong temperature dependence shifts to a higher temperature as the magnetic field is increased. From Fig. 5-9, we identify the characteristic temperature T_C at which the slow rate rises to a value equal to the geometric mean of the two tunneling rates at the lowest temperature (as indicated by the arrows) and plot it as a function of magnetic field for samples p061998a and p040297 in Fig. 5-10. The characteristic temperature T_C rises almost linearly as we increase the magnetic field. In this range of magnetic field, T_C ($\sim$450 mK at 4.5 T) sets an energy scale that is much smaller than the Coulomb energy and

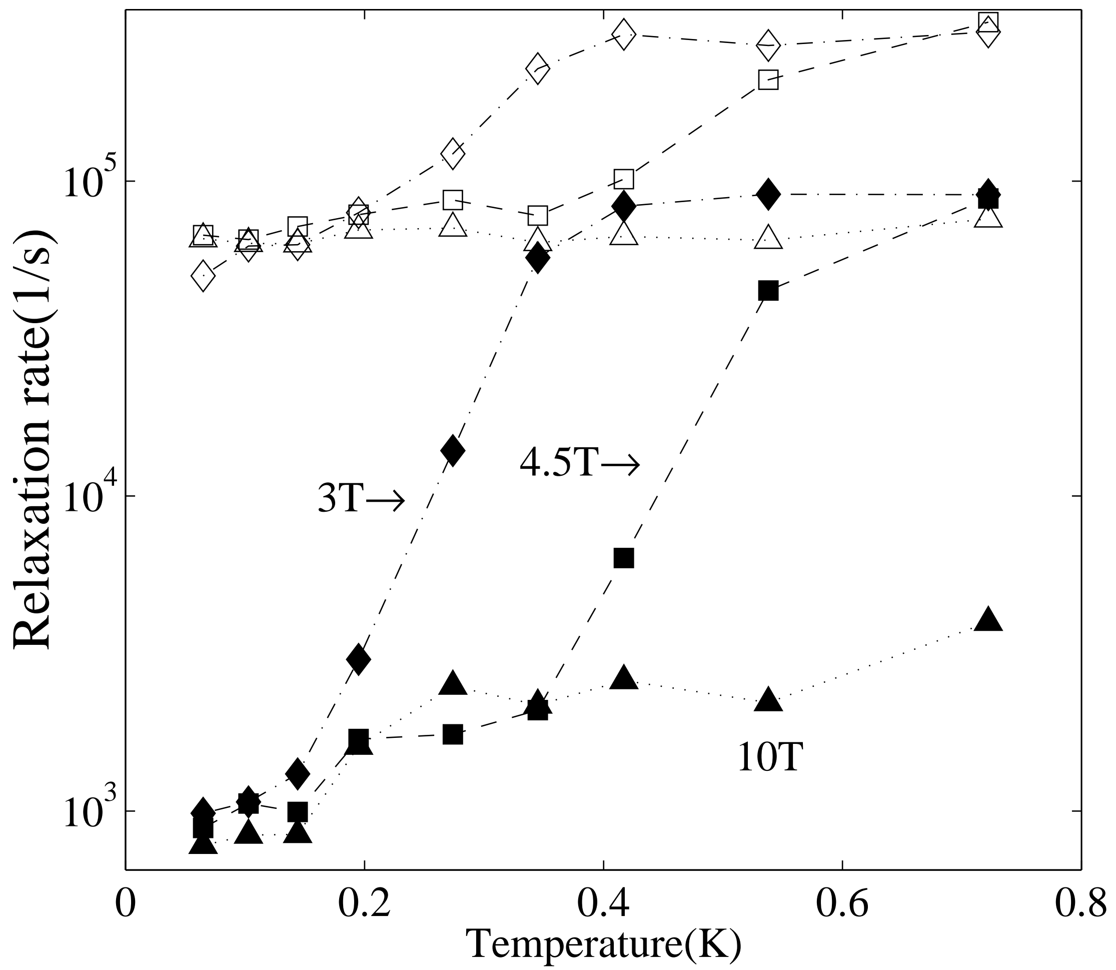

Figure 5-9: Temperature dependence of the fast (hollow) and slow (filled) relaxation rates for sample B at $\nu = 1$ for 3 T (diamonds), 4.5 T (squares) and 10 T (triangles).

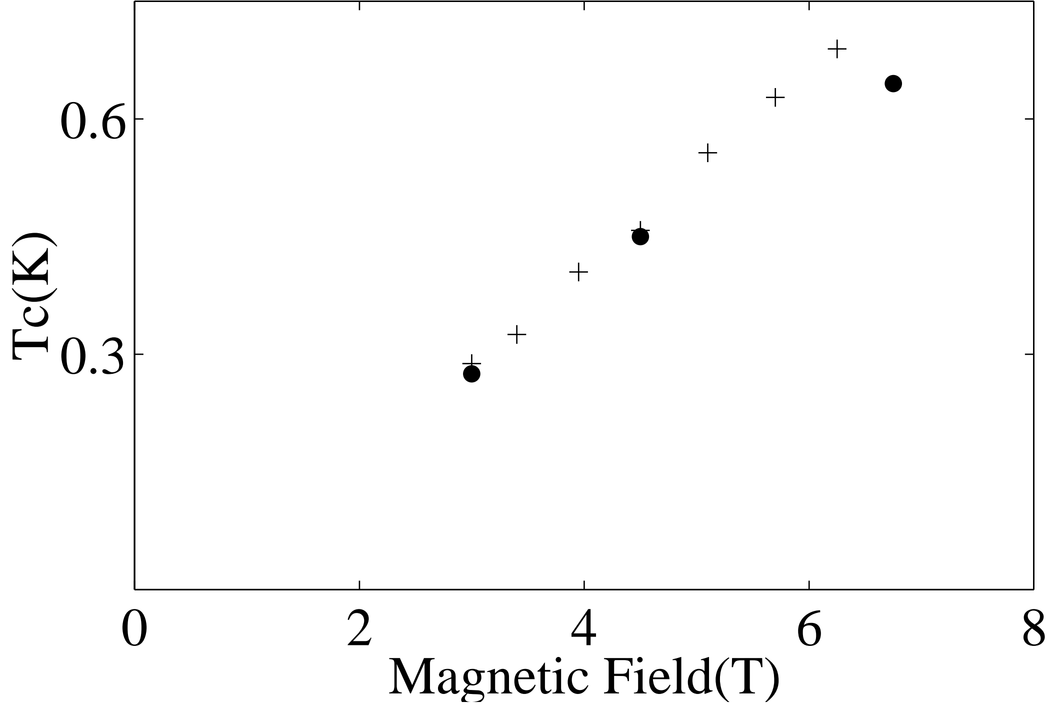

Figure 5-10: Characteristic temperature T_C vs. magnetic field for sample A (crosses) and sample B (circles). T_C is defined as the temperature at which the slow rate rises to a value equal to the geometric mean of the two tunneling rates at the lowest temperature in Fig. 5-9.

the cyclotron energy (106 K and 90 K at 4.5 T respectively). The only obvious energy scale comparable to T_C is the Zeeman energy (1.3 K at 4.5 T). In other words the development of the exchange energy gap at $\nu = 1$ is not a sufficient condition for tunneling to occur at two rates. The temperature must also be lower than the Zeeman energy. For instance, at a field of 4.5 T and temperature of 1 K, a minimum in the capacitance of the 2DEG is clearly observable at $\nu = 1$ (Fig. 5-11a), indicating the existence of the exchange energy gap. However, as Figs. 5-11b and c show, electrons no longer tunnel at two rates at this temperature and magnetic field. In most circumstances, the relevant energy scale associated with the $\nu = 1$ quantum Hall state is the Coulomb energy among electrons. It is the Coulomb exchange energy that keeps the system ferromagnetic. However, in order for electrons to tunnel at two rates, the temperature not only have to be lower than the Coulomb energy, but also lower than the Zeeman energy. This, along with the fact that the double rate phenomenon does not occur at even filling factors, strongly suggests that spin effects are crucial in

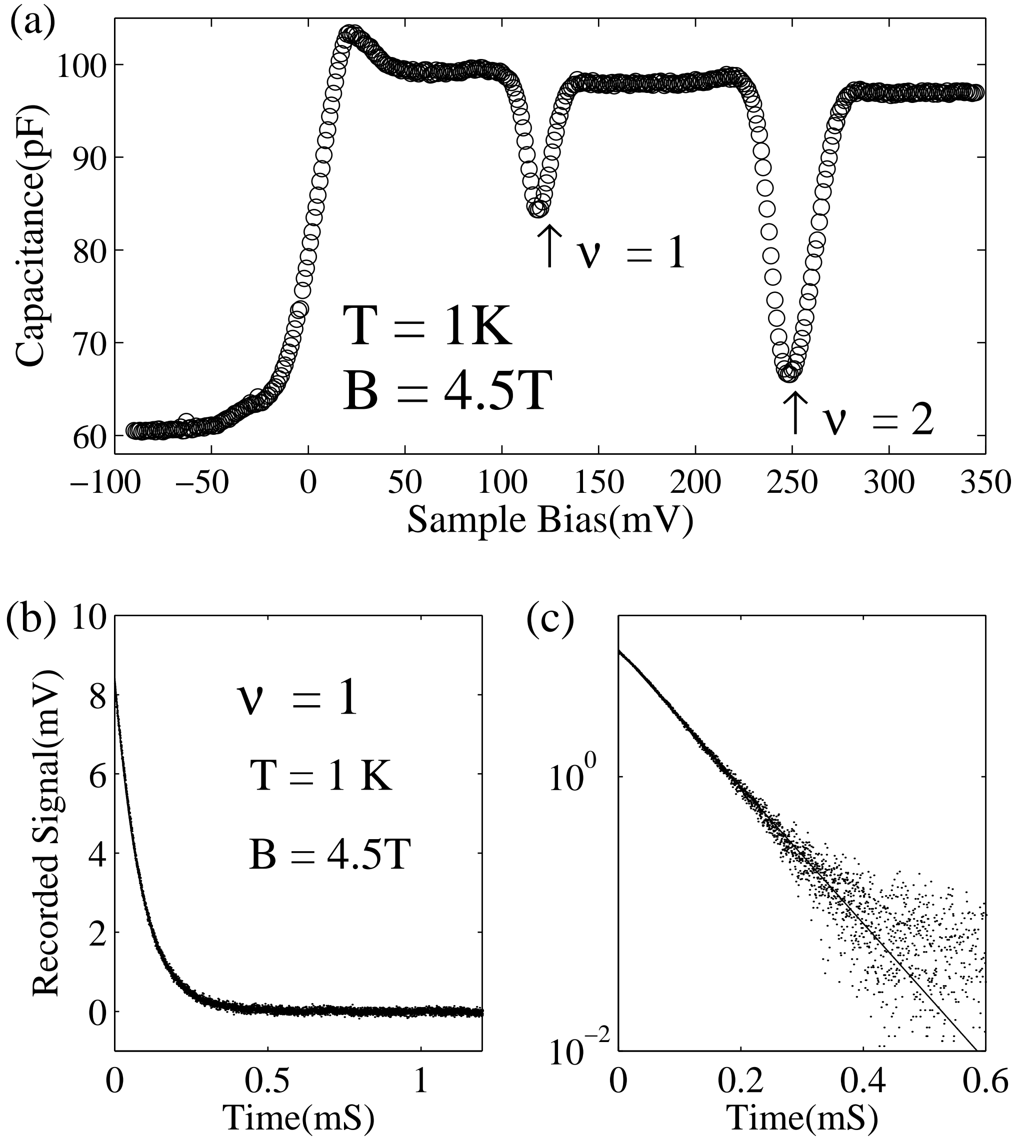

Figure 5-11: (a) At a magnetic field of 4.5 T and a temperature of 1K , there is a clear minimum in sample capacitance at $\nu = 1$, indicating the existence of the exchange energy gap. (b) and (c) Recorded signal at the same temperature and field at $\nu = 1$ on linear and semi-log scale, which shows that tunneling occurs at a single rate at this temperature.

explaining why tunneling occurs at two rates at $\nu = 1$.

5.7 Phase Separation vs. In-plane Relaxation

Possible explanations of the double tunneling rate phenomenon at $\nu = 1$ can generally be classified into two approaches. In the first approach, electrons are assumed to tunnel into the 2D system at a fast rate. The system then undergoes certain form of relaxation, possibly spin related, within the 2D plane at the slow rate. Through the spin relaxation, the 2D system is able to accept more electrons tunneling from the 3D electrode giving rise to a second, slower tunneling rate. Unlike the fast tunneling rate, the slow relaxation is expected to have no dependence on the thickness of the tunnel barrier. A second approach considers the $\nu = 1$ system bifurcating into separate regions into which electrons tunnel at different rates. In contrast to the first scenario, the ratio of the two tunneling rates should remain constant as the tunnel barrier thickness is varied.

In order to differentiate between these two possibilities, we measure the relaxation rates for samples grown in the same MBE machine with various tunnel barrier thickness. Figure 5-12 plots results from three samples (p040297, p061998a and p092696) with different barrier thickness. Each plot corresponds to result for a different sample. For each sample, we show the tunneling rate at $\nu = 1/2$ and $\nu = 1$. At $\nu = 1/2$, we observe a single relaxation rate in all samples. The relaxation rate increases by more than 3 orders of magnitude as the tunnel barrier becomes more transparent. At $\nu = 1$ the fast rate depends on the tunnel barrier thickness in the same manner. In contrast, the slow rate at $\nu = 1$ is relatively insensitive to the thickness of the tunnel barrier, varying by less than a factor of 10 even when the $\nu = 1/2$ relaxation rate changes by a factor of 1000. In sample p040297, the relaxation rate at $\nu = 1$ is faster than the rate at $\nu = 1/2$. However, in sample p092696, the opposite is true. The relaxation rate at $\nu = 1/2$ is slower than at $\nu = 1$. This provides strong evidence that the slow tunneling rate at $\nu = 1$ is largely due to relaxation within the 2D plane.

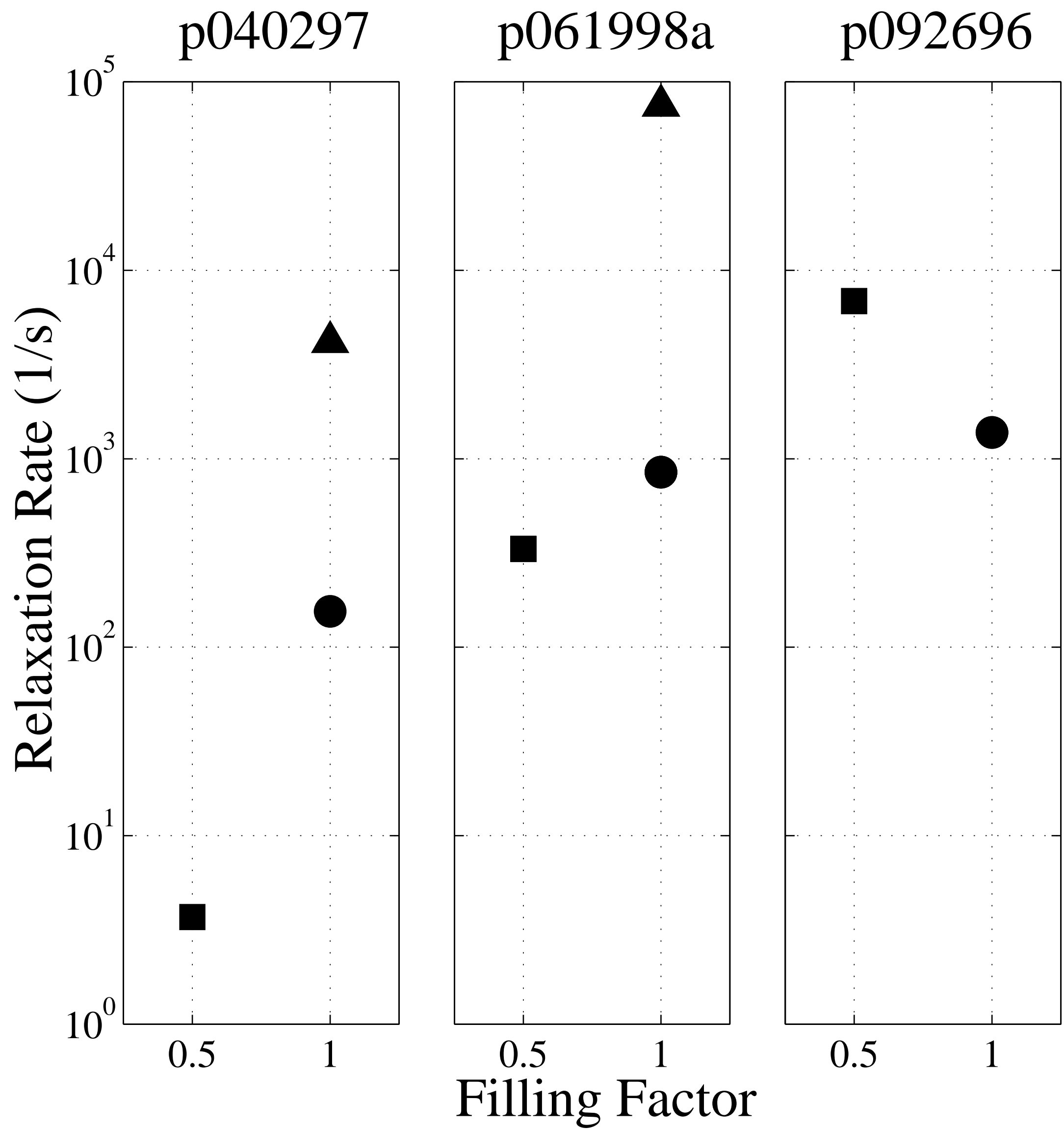

Figure 5-12: Relaxation rates at 6.6T for samples with different tunnel barrier thickness at $\nu = 1/2$ and at $\nu = 1$. At $\nu = 1/2$, we observe a single relaxation rate in all three samples. At $\nu = 1$, the fast and slow rates are plotted as triangles and circles respectively. For sample p092696, the fast relaxation rate is out of our detection range.

5.8 Spin Bottleneck for Tunneling

Before we continue with discussion of our results, let us summarize here the characteristics of the double tunneling rate phenomenon:

- We detect two distinct relaxation rates that differ by up to a factor of 60 for tunneling into ferromagnetic quantum Hall states at $\nu = 1, 3$ and $1/3$, but not at $\nu = 2$.
- The temperature must be lower than the Zeeman energy $g\mu_B B$ in order to observe the slow tunneling rate.
- The slow tunneling rate is insensitive to variations in tunnel barrier thickness.

Since the slow tunneling rate only appears in spin-polarized quantum Hall states at temperatures lower than the Zeeman energy, we describe it as arising from a "spin bottleneck" in which in-plane spin relaxation must proceed before additional electrons can tunnel into the system.

In Chapters 3 and 4 we discussed suppression of tunneling rate due to non-equilibrium charge accumulation. Here we discovered that non-equilibrium spin accumulation can also reduce tunneling rates into a 2D system under the appropriate conditions.

One example of in-plane relaxation that might be relevant is the formation of Skyrmions around $\nu = 1$, which we described at the beginning of this chapter in section 5.1. For a perfectly uniform system precisely in the $\nu = 1$ ferromagnetic state, tunneling injects a single minority spin (Fig. 5-1a) because the thickness of the tunnel barrier ensures that electrons tunnel as single entities. Since this is not the lowest energy excitation, over time the 2D system can lower its energy by flipping more spins to create Skyrmions (Fig. 5-1b). Because the energy of the 2D system is lowered by Skyrmion formation, more electrons tunnel from the 3D electrode to keep the chemical potentials on the two sides of the tunnel barrier aligned. When the time scale for spin relaxation is long, the intermediate stage forms a bottleneck and temporarily prevents more electrons from tunneling. The slow relaxation time

of ∼1 ms is comparable to electron spin relaxation times measured in a recent NMR experiment [50].

5.9 MacDonald's Model for Tunneling at $\nu = 1$

In this section we discuss a formalism proposed by MacDonald [51] to describe tunneling into the $\nu = 1$ quantum Hall state. MacDonald finds that the double tunneling rate phenomenon occurs only in the presence of non-equilibrium spin accumulation, the magnitude of which depends subtly on the interplay of spin-dependent tunneling conductances, thermodynamic density of states and spin relaxation rates.

5.9.1 General Formalism

MacDonald defines separate chemical potentials $\mu_\uparrow$ and $\mu_\downarrow$ for the 2D spin-up and spin-down subsystems respectively. This is a valid assumption if the spin relaxation time is much longer than other scattering times, as in the case for ferromagnetic quantum Hall states. The following equations describe the spin-partition of current:

$$\begin{aligned} \dot{Q}_\uparrow &= -\mu_\uparrow G_\uparrow + (\mu_\downarrow - \mu_\uparrow) G_s \\ \dot{Q}_\downarrow &= -\mu_\downarrow G_\downarrow + (\mu_\uparrow - \mu_\downarrow) G_s \end{aligned} \tag{5.2}$$

where Q_σ and G_σ are respectively the number of spin-σ electrons in the 2D system and the tunneling conductance for spin-σ electrons (to simplify notation, we set the electronic charge e to one). G_S describes spin relaxation between electrons of opposite spins. Here μ_σ is measured with reference to the chemical potential in the 3D electrode.

Another set of capacitance equations relate the chemical potentials to accumulated charges:

$$\begin{aligned} \mu_\uparrow &= -V_0 + (C^{-1})_{\uparrow\uparrow} Q_\uparrow + (C^{-1})_{\uparrow\downarrow} Q_\downarrow \\ \mu_\downarrow &= -V_0 + (C^{-1})_{\downarrow\uparrow} Q_\uparrow + (C^{-1})_{\downarrow\downarrow} Q_\downarrow \end{aligned} \tag{5.3}$$

where V_o represents the electrostatics contribution from charges external to the 2D system. The inverse capacitance matrix contains an electrostatic contribution proportional to the thickness of the tunnel barrier and a quantum mechanical contribution arising from the finite thermodynamic DOS as well as correlations in the 2DEG:

$$(C^{-1})_{\sigma\sigma'} = \frac{1}{C_g} + \frac{1}{A}\frac{d\tilde{\mu}_\sigma}{dN_{\sigma'}} \tag{5.4}$$

where $C_g = \kappa A/x_w$ is the geometric capacitance between the quantum well and the 3D electrode, A is the cross-sectional area of the 2D electron system, κ is the dielectric constant, x_w is the distance between the 3D electrode and the quantum well, $\tilde{\mu}_\sigma$ is the spin-σ chemical potential of the 2DEG relative to the conduction band edge and N_σ is the number density for spin-σ electrons.

For non-interacting electrons, quantum contributions to the off-diagonal elements of the inverse capacitance matrix vanish:

$$\frac{d\tilde{\mu}_\sigma}{dN_{\sigma'}} = \frac{\delta_{\sigma\sigma'}}{n_\sigma} \tag{5.5}$$

where n_σ is the density of states for spin σ. $\delta_{\sigma\sigma'}$ equals 1 if $\sigma = \sigma'$ and equals zero otherwise.

In general, $d\tilde{\mu}_\sigma/dN_{\sigma'}$ is non-zero for $\sigma \neq \sigma'$ for an interacting system. For instance, at filling factor $\nu = 1$, creation of a Skyrmion consisting of 3 flipped spins requires the addition of 4 minority spins together with the removal of 3 majority spins. Spin-up and spin-down electrons must be added to the system according to a certain ratio in order to form Skyrmions, giving rise to non-zero $d\tilde{\mu}_\uparrow/dN_\downarrow$. One can refer to Ref. [51] for the procedure to calculate $d\tilde{\mu}_\uparrow/dN_\downarrow$.

To proceed, we rewrite Eq. 5.2 and 5.3 in matrix notation:

$$\dot{\mathbf{Q}} = \mathbf{G}\mu \tag{5.6}$$

$$\mu = -\mathbf{V_0} + \mathbf{C^{-1}Q} \tag{5.7}$$

from which we can eliminate μ to obtain:

$$\dot{\mathbf{Q}} = -\mathbf{G}\mathbf{V_0} + \mathbf{G}\mathbf{C^{-1}}\mathbf{Q} \tag{5.8}$$

$$= -\mathbf{G}\mathbf{V_0} + \mathbf{B}\mathbf{Q} \tag{5.9}$$

where $\mathbf{B} = \mathbf{G}\mathbf{C^{-1}}$. The boundary conditions for this set of first order coupled differential equation are:

$$Q_{\uparrow}(t=0) = Q_{\downarrow}(t=0) = 0 \tag{5.10}$$

In our experiment, this corresponds to the fact that immediately after we apply the voltage step, no extra charge has been transferred into the 2D system yet. Solving Eq. 5.9 with the above boundary conditions yields the current due to spin σ:

$$\dot{Q}_{\sigma}(t) = I_{\sigma,+}\exp(-t/\tau_{+}) + I_{\sigma,-}\exp(-t/\tau_{-}) \tag{5.11}$$

In general, the current consists of two components with different relaxation rates τ_{+}^{-1} and τ_{-}^{-1} that are the eigenvalues of matrix $\mathbf{B}$:

$$\frac{1}{\tau_{\pm}} = \frac{B_{\uparrow\uparrow} + B_{\downarrow\downarrow}}{2} \pm \left[(\frac{B_{\uparrow\uparrow} - B_{\downarrow\downarrow}}{2})^2 + B_{\uparrow\downarrow}B_{\downarrow\uparrow} \right]^{1/2} \tag{5.12}$$

Using Eq. 5.7, one can also obtain the instantaneous chemical potentials of the spin-up and spin-down subsystems:

$$\mu_{\sigma}(t) = -V_0 + \mu_{\sigma,+}[1 - \exp(-t/\tau_{+})] + \mu_{\sigma,-}[1 - \exp(-t/\tau_{-})] \tag{5.13}$$

where $\mu_{\sigma,\pm} = \sum_{\sigma'} C^{-1}_{\sigma,\sigma'} I_{\sigma',\pm}\tau_{\pm}$. The two spin subsystems are in equilibrium at both the beginning and the end of the tunneling process but are in general, out of equilibrium at intermediate times. Non-equilibrium spin accumulation occurs when the chemical potentials for the spin-up and spin-down electrons are not equal:

$$\mu_{\uparrow}(t) - \mu_{\downarrow}(t) = (\mu_{\downarrow,-} - \mu_{\uparrow,-})(\exp(-t/\tau_{-}) - \exp(-t/\tau_{+})) \tag{5.14}$$

To obtain Eq. 5.14 from Eq. 5.13, we made use of the relation $\mu_{\uparrow,+}+\mu_{\uparrow,-} = \mu_{\downarrow,+}+\mu_{\downarrow,-}$. This follows from the fact that the chemical potentials of the two spin subsystems (given by Eq. 5.13) equilibrate at $t \to \infty$.

5.9.2 Coupling of the Two spin subsystems through $dN_\uparrow/d\mu_\downarrow$ and $dN_\downarrow/d\mu_\uparrow$

As we mentioned earlier, this formalism incorporates correlation effects by the terms $dN_\uparrow/d\mu_\downarrow$ and $dN_\downarrow/d\mu_\uparrow$ in the off-diagonal elements of the inverse capacitance matrix. In fact, non-zero $dN_\uparrow/d\mu_\downarrow$ and $dN_\downarrow/d\mu_\uparrow$ are essential for explaining the double tunneling rate phenomenon we observed. In this subsection, we show that in the absence of interactions in the 2D system that couple the spin-up and spin-down subsystems, non-equilibrium spin accumulation will not occur even if the spin flipping rate is very slow and/or the density of states for the two spin subsystems are significantly different.

If we ignore correlations contributions $dN_\uparrow/d\mu_\downarrow$ and $dN_\downarrow/d\mu_\uparrow$ to the chemical potential of the 2DEG, the inverse capacitance matrix reduces to:

$$\mathbf{C^{-1}} = \begin{pmatrix} 1/C_g + 1/(An_\uparrow) & 1/C_g \\ 1/C_g & 1/C_g + 1/(An_\downarrow) \end{pmatrix} \tag{5.15}$$

where A is the area of the 2D system, C_g is the geometric capacitance as defined before, and n_σ is the density of states for spin σ that might be significantly different for spin-up and spin-down electrons. The tunneling conductance G_σ for each spin subsystem is proportional to the density of states n_σ:

$$G_\sigma = an_\sigma \tag{5.16}$$

and G_s (associated with spin flip) is proportional to the product of the density of states in the up-spin and down-spin subsystems:

$$G_S = bn_\uparrow n_\downarrow \tag{5.17}$$

where a and b are proportionality constants. Equations 5.16 and 5.17 follow from Golden rule estimates of the tunneling rate and the spin-flip rate respectively. Equation 5.9 becomes:

$$\begin{pmatrix} \dot{Q}_\uparrow \\ \dot{Q}_\downarrow \end{pmatrix} = -aV_o \begin{pmatrix} n_\uparrow \\ n_\downarrow \end{pmatrix} + \begin{pmatrix} an_\uparrow/C_g + (a + bn_\downarrow)/A & n_\uparrow(a/C_g - b/A) \\ n_\downarrow(a/C_g - b/A) & an_\downarrow/C_g + (a + bn_\uparrow)/A \end{pmatrix} \begin{pmatrix} Q_\uparrow \\ Q_\downarrow \end{pmatrix} \tag{5.18}$$

We obtain the two relaxation times using Eq. 5.12:

$$\tau_+^{-1} = a(1/A + (n_\uparrow + n_\downarrow)/C_g) \tag{5.19}$$

$$\tau_-^{-1} = [a + b(n_\uparrow + n_\downarrow)]/A \tag{5.20}$$

The tunneling current contributions from each of the two spin subsystems contain two exponential decays with time constants τ_+ and τ_-:

$$I_\uparrow(t) = I_{\uparrow,+}\exp(-t/\tau_+) + I_{\uparrow,-}\exp(-t/\tau_-) \tag{5.21}$$

$$I_\downarrow(t) = I_{\downarrow,+}\exp(-t/\tau_+) + I_{\downarrow,-}\exp(-t/\tau_-) \tag{5.22}$$

Even though the solution contains two relaxation times, the boundary condition $Q_\uparrow(t = 0) = Q_\downarrow(t = 0) = 0$ (Eq. 5.10) leads to the vanishing of both the prefactors $I_{\uparrow,-}$ and $I_{\downarrow,-}$ of the slow decay (after a considerable amount of straightforward mathematics):

$$I_{\uparrow,-} = I_{\downarrow,-} = 0 \tag{5.23}$$

Therefore the total tunneling current, as well as its spin-up and spin-down components, contain only a single exponential decay:

$$\begin{aligned} I(t) &= I_{\uparrow,+}\exp(-t/\tau_+) + I_{\downarrow,+}\exp(-t/\tau_+) \\ &= I_+\exp(-t/\tau_+) \end{aligned} \tag{5.24}$$

where $I_+ = I_{\uparrow,+} + I_{\downarrow,+}$. Our observation of two decay times for tunneling into the $\nu = 1$

quantum Hall state is therefore evidence for interactions that couple the spin-up and spin-down subsystems, leading to non-zero $dN_\uparrow/d\mu_\downarrow$ and $dN_\downarrow/d\mu_\uparrow$. This subsection demonstrates that without this coupling, tunneling will only occur at a single rate even if the density of states $n_\uparrow$ and $n_\downarrow$ are significantly different and the spin flip rate is much slower than the tunneling rate ($G_S << G_\sigma$). The reason non-equilibrium spin accumulation does not occur is that the ratio of tunneling conductances ($G_\uparrow/G_\downarrow$) equals the ratio of the thermodynamic DOS ($n_\uparrow/n_\downarrow$), which, by definition, is the rate at which the chemical potential increases with density.

At $\nu = 1$, MacDonald found that the ratio of fast to slow relaxation rates is independent of G_σ and G_S, provided the tunnel barrier is thin enough that $G_\sigma \gg G_S$. If, in addition, the quantum contributions ($dN_\sigma/d\mu_{\sigma'}$) dominates the geometric term (C_g) of the inverse capacitance matrix, MacDonald found that $\tau_-/\tau_+ = (2K+1)^2 = 49$, where $K = 3$ assuming the lowest energy quasiparticle excitations at $\nu = 1$ are Skyrmions consisting of 3 flipped spins. In our experiment, the ratio of relaxation rates has a value of 30 and 90 in samples p040287 and p061998a respectively (Fig. 5-12), in rough agreement with MacDonald's theory. Discrepancies might arise from sample inhomogeneity at $\nu = 1$.

5.10 Comment on double tunneling rates at $\nu = 3$

There is one feature of the double rate tunneling phenomenon that is not explained by the theory of Skyrmions. We observe that electrons tunnel at two distinct rates into the 2D system at $\nu = 1$, 3 and 1/3, as shown in Fig. 5-5. We associated the appearance of two rates at $\nu = 1$ by the formation of Skyrmions. Similar arguments apply to the spin-polarized $\nu = 1/3$ fractional quantum Hall state, whose charged excitations are predicted [3, 4] to contain spin texture like at $\nu = 1$. However, at $\nu = 3$ Skyrmions are predicted to have higher energies than excitations consisting of a single flipped spin. A transport experiment by Schmeller *et al.* [46] demonstrated that at $\nu = 3$ the dependence of the energy gap on tilted magnetic field is consistent with elementary excitations being ordinary single spin-flip excitations. Spin relaxation mechanisms

other than the formation of Skyrmions could be responsible for the observation of two tunneling rates at $\nu = 3$.

5.11 Comparison to result from another research group

We note that Dolgopolov *et al.* [32] reported tunneling relaxation measurements on similar structures around $\nu = 1$ and did not observe the bifurcation of rates described in this Chapter. We believe that this experiment was performed over a range of frequencies too low and narrow to permit detection of the fast rate, and we speculate that their data reflect the behavior of the slow relaxation. Another possibility for the discrepancy is the difference in mobility between their samples and ours. In Dologpolov's sample the capacitance signal at $\nu = 1$ decreases only by 10% at 11.5T [32]. This leads Dolgopolov to claim that the thermodynamic DOS of the 2DEG is sufficiently high at $\nu = 1$ so that the displacement current flowing out of their sample is independent of the thermodynamic DOS. On the other hand, in our samples the capacitance signal at $\nu = 1$ drops by more than 90% at the same field of 11T at low temperatures. The thermodynamic DOS of our 2DEG is thus very small at $\nu = 1$. We therefore believe that in our samples the Landau levels are much narrower in energy and the 2DEG has much less disorder.

5.12 Summary

In this Chapter, we studied the effect of interactions among electronic spins on tunneling. We measure equilibrium tunneling between a 3D electrode and a high mobility 2D electron system. For most non-integer Landau level filling factors, we find that tunneling can be characterized by a single, well-defined tunneling rate. However, for spin-polarized quantum Hall states ($\nu = 1$, 3 and 1/3) tunneling occurs at two distinct rates that differ by up to 2 orders of magnitude. Upon increasing the temperature, the slow rate speeds up and the double tunneling rate phenomenon disappears. The

characteristic temperature is about 1/3 of the Zeeman energy. Furthermore, the slow rate is largely due to relaxations within the 2D plane because it is insensitive to variations in the tunnel barrier thickness in different samples.

From the above observations, we conclude that slow in-plane spin relaxation creates a bottleneck for tunneling of electrons into ferromagnetic quantum Hall states. We also described a theoretical model by Allan MacDonald on non-equilibrium electron spin dynamics. MacDonald explains the double tunneling rate phenomenon by the formation of Skyrmions in the tunneling process.

Chapter 6

Future Prospects

In this thesis, we measured the tunneling conductance into 2D electron systems using "time domain capacitance spectroscopy" (TDCS). Using TDCS, we are able to measure the complete current-voltage characteristics for tunneling even when the in-plane conductance is very low. For the first time, we detect the contributions of both localized and extended states to the tunneling current. TDCS has the unique capability of measuring the tunneling current into structures to which direct ohmic contact is difficult or impossible. We used TDCS to explore three different regimes of the 2DEG in this thesis. First we study the logarithmic Coulomb anomaly for tunneling into a disordered 2D electronic system. Then we demonstrated that in a magnetic field, the tunneling conductance depends linearly on voltage, with a slope inversely proportional to the magnetic field strength. Furthermore, we discovered that interactions among electronic spins can also slow down tunneling into ferromagnetic quantum Hall states, leading to non-equilibrium spin accumulation and the appearance of two tunneling rates.

TDCS enables us to measure tunneling in regimes not accessible before by conventional methods. We believe the results described in this thesis are only the beginning of a series of interesting TDCS experiments. This chapter will describe potentially interesting topics for future TDCS study.

6.1 Tunneling into $\nu = 1$ at tilted Magnetic Fields

In chapter 5, we observed two distinct tunneling rates into ferromagnetic quantum Hall states. We presented evidence that the slower of the two rates is due to non-equilibrium spin accumulation and possibly related to the formation of Skyrmion excitations at $\nu = 1$. We obtained the tunneling data in chapter 5 in a perpendicular magnetic field with in-plane component equal to zero. For an ideal, infinitely thin 2D system, an in-plane magnetic field only couples to the system through the Zeeman energy, while the perpendicular field affects both the Zeeman energy and the orbital motion that determines the filling factor. As we described in Chapter 5, the number of flipped spins contained in a Skyrmion is determined by the ratio of the Zeeman energy to the Coulomb energy. A small ratio favors the formation of Skyrmions. A sufficiently strong in-plane component of magnetic field might decrease the number of flipped spins a Skyrmion contains because it increases the Zeeman energy. In the picture of MacDonald (section 5.9), this modifies the constraint of the ratio at which spin-up and spin-down electrons must be added to the 2D system in order to create a lowest energy excitation.

However, interpretation of tilted field tunneling data might not be straight forward. In addition to the Zeeman coupling, the parallel component of magnetic field modifies the transverse momentum conservation rules and alters the tunneling rate [18], making it difficult to isolate spin effects.

6.2 Coulomb Anomaly in high mobility sample

In Chapter 3, we measured the logarithmic Coulomb anomaly for the first time in semiconductor 2D systems. One key observation is that the logarithmic correction persists to voltages higher than the inverse scattering time ($1/\tau$) when electron motion is quasi-ballistic. This regime is not accessible in thin metallic films because the scattering time is much shorter and the quasi-ballistic regime occurs at too high excitation voltages.

We performed most of the measurements in Chapter 3 on samples that have a high degree of disorder. For the high mobility samples used in our study of spin effects in Chapter 5, the scattering time (τ) is expected to be significantly longer. Preliminary measurements of the high mobility samples indeed indicates that the logarithmic tunneling anomaly takes place at about four times lower densities compared to the more disordered samples. Recall that the corrections to the single particle DOS are universal in systems with identical $E_F\tau$. Since E_F is a factor of 4 smaller in the high mobility samples when the corrections are significant, τ is larger by the same factor. This shifts the onset of the quasi-ballistic regime to voltages a factor of 4 smaller compared to the more disordered samples. In other words, the high mobility samples should provide an even larger voltage range for studying the quasi-ballistic behavior of electron motion.

6.3 Single Particle Density of States in a non-quantizing Magnetic Field

The density of states of a 2D system in strong magnetic field consist of Landau levels. In a sufficiently weak magnetic field, the energy separation between two adjacent Landau levels $\hbar\omega_c$ (where ω_c is the cyclotron frequency) is smaller than their disordered-induced width and the Landau quantization peaks disappear if $\omega_c\tau_s \ll 1$, where τ_s is the electron quantum lifetime. Rudin et al. [52, 53] recently studied theoretically the effect of electron-electron interactions on a 2D electron system in such a "classical" magnetic field. They found that if the disorder potential is weak and smooth (with correlation length much larger than the Fermi wavelength and amplitude much smaller than the Fermi energy), electrons experience small-angle scattering. The corresponding transport relaxation time τ_{tr} is considerably larger than τ_s. For the magnet field range satisfying $\omega_c\tau_s \ll 1 \ll \omega_c\tau_{tr}$, the classical trajectories are strongly affected by the magnetic field even though Landau quantization is destroyed. Rudin predicted that contrary to the non-interacting case, there are significant corrections

to the single particle density of states in this regime, resulting in peaks separated by the cyclotron energy. Unlike the Landau levels in strong field, the amplitude of the peaks decreases and their widths increase as a function of energy from the Fermi level.

To our knowledge, there has not been any experimental verification of Rudin's theory. Even though this thesis concentrates on tunneling conductance measurements in various low excitation regimes, TDCS should have no problem resolving the oscillations at high excitations predicted by Rudin. According to Rudin, the range of magnetic field where this theory is applicable depends on sample mobility. For high mobility samples, it is between 0.001T and 0.05T. This range shifts to higher fields in more disordered samples.

6.4 Excitation Voltage Study of the Tunneling Enhancement at weak magnetic field

In section 3.6, we described the enhancement of zero-bias tunneling conductance in a weak magnetic field at the density range over which the logarithmic Coulomb anomaly in tunneling occurs. As we mentioned, we cannot determine whether the enhancement is due to suppression of the Cooper channel interaction or a combination of interactions and weak localization effects. Measuring the excitation dependence of the conductance in a weak perpendicular and/or parallel magnetic field might enable us to distinguish between the two possibilities.

6.5 Excitation Voltage Dependence of Tunneling Conductance at Even Denominator Filling Factors

Recently, even denominator fractional quantum Hall states have received considerable attention. Lily [54] reported that at large half-integer fillings such as $\nu = 9/2$, $11/2$

and 13/2, in-plane transport measurements display strong anisotropy. The in-plane resistance attains either a maximum or a minimum at these filling factors depending on the orientation of the current. Such anisotropy is not present for lower filling factors of $\nu = 7/2$ and below. Koulakov et al. [36] predicted that a clean 2D system in the third or higher Landau levels may be unstable against the formation of charge density waves. The stable configuration is a stripe phase where the filling of the highest Landau level alternates between zero and one. Koulakov showed that the gap in the single particle DOS depends linearly on magnetic field for such system.

There has also been proposal of the possibility that a superconducting state might exist at $\nu = 5/2$ [55, 56, 57]. At $\nu = 5/2$, the lowest Landau level is completely filled and the lower spin-split level of the second Landau level is half filled. The superconducting state, if applicable, arises from a two-step process. First, electrons in the second, half filled Landau level forms a Fermi sea of composite Fermions [58], which then pair and condense into the novel superconducting state. Although the concept of the new phase is very interesting, so far there has not been experimental evidence for such a state.

Given the richness of the physics of even denominator fractional quantum Hall states, one would expect measurement of the tunneling conductance into high mobility 2D systems using TDCS, in particular the excitation voltage dependence, might yield useful information that might enable better understanding of their properties.

6.6 Reproducible Fluctuations in Equilibrium tunneling conductance

In Chapter 5, we focused on the double relaxation rate phenomenon for tunneling into the 2D system at odd integer filling factors. As shown in Fig. 5-5 the equilibrium tunneling conductance of the sample varies by more than 3 orders of magnitude depending on the exact value of the filling factor ν. In sample p092696a, we measured the equilibrium tunneling relaxation rate in very small steps in sample bias and found

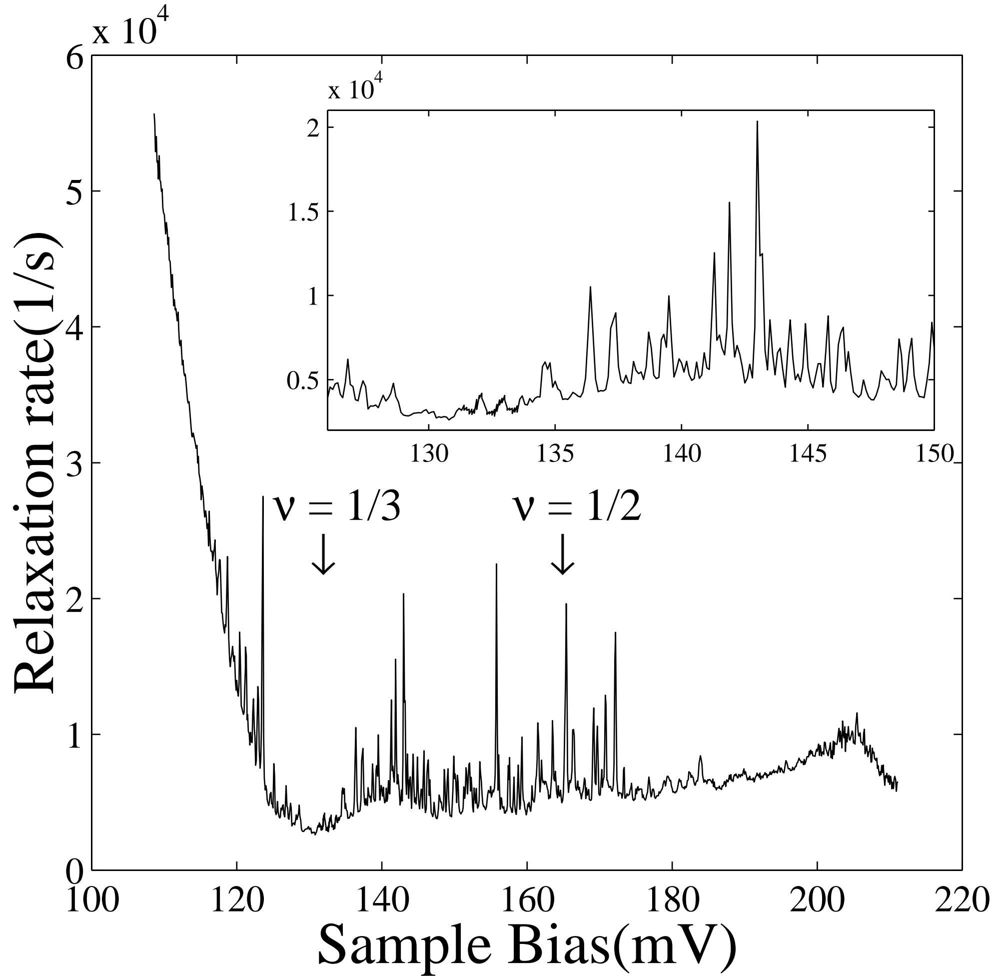

Figure 6-1: Relaxation rate as a function of sample bias for sample p092696a at 10T and 30 mK. The inset, which has identical axes and units as the main figure, illustrates the reproducible fluctuations by zooming into the bias range 125mV to 150mV of the curve in the main figure.

that the relaxation rate exhibits reproducible fluctuations, as shown in Fig. 6-1. At the peaks the relaxation rate increases by as much as a factor of 4. The range of sample bias displayed in Fig. 6-1 corresponds to filling factors ν from 0.28 to 0.7 approximately. The oscillation pattern changes upon thermal cycling, but the range of sample bias at which the fluctuation occurs remains essentially unchanged.

Figure 6-2b displays the evolution of the fluctuations with magnetic field. For each successive curve from the top, the magnetic field increases by 0.1T. We have subtracted a smooth background from the tunneling current. As the magnetic field is increased, the fluctuating features shift in sample bias by approximately the same

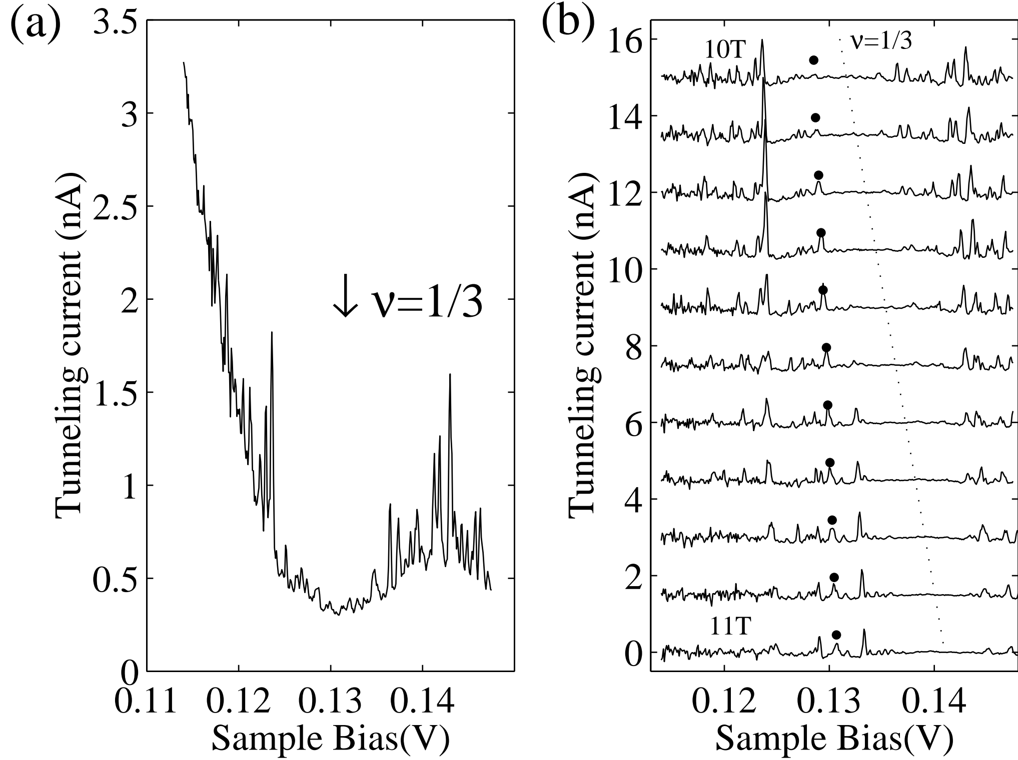

Figure 6-2: (a) Tunneling current vs sample bias at 10T. The excitation voltage is 12 μV across the tunnel barrier. (b) Evolution of the fluctuations as the magnetic field increases. We eliminate the smooth variation in (a) by fitting a 6th order polynomial and subtracting it from the data. The curves are displaced vertically for clarity. For each successive curve from the top, the magnetic field increases by 0.1T. The filled circle indicates the shift in position of a particular peak as the magnetic field increases and the dotted line marked the sample bias at which the $\nu = 1/3$ minimum in tunneling conductance occurs.

amount, independent of the filling factor at which they occur. For instance, the filled circles follow the shift in position of a particular peak as the magnetic field increases. The peak shifts by about 2mV in sample bias in Fig. 6-2b, comparable to the increase in cyclotron energy for the same increase in magnetic field. Apart from the shift in sample bias, there are no clear trends for the evolution of the peaks. Different peaks appear or disappear as the magnetic field increases. Another remarkable feature is that the fluctuations are mostly absent when the filling factor ν is close to 1/3.

Currently we do not have sufficient data to determine the origin of these fluctuations in tunneling conductance. One obvious possibility is the presence of impurity levels in the tunnel barrier that leads to resonances in tunneling. However, it is unclear why the fluctuations are absent at zero magnetic field and only occur at a

certain range of magnetic fields and sample bias. More experimental work is required to understand these conductance fluctuations.

6.7 Tunneling Rates into Quantum Dots and Spectroscopy of Excited States

This thesis focuses on TDCS measurements of the tunneling rates into 2D electron systems. As we pointed out in Chapter 2, TDCS is also capable of measuring the tunneling rate into a quantum dot. A quantum dot is a mesoscopic structure in which electron motion is confined in all three directions, unlike in 2D systems where only a single direction of motion is constrained. To create quantum dots in GaAs, one typically starts with a 2DEG at the interface of GaAs/AlGaAs or in a GaAs quantum well. Lateral confinement is provided either by applying negative voltages to metallic gates patterned on the surface of the heterostructure, or by selectively etching of the wafer while protecting the quantum dot with metal or photoresist [59, 60]. Ashoori et al. developed single electron capacitance spectroscopy (SECS) [61] to resolve the energy levels corresponding to the addition of single electrons in structures that are, apart from the lateral confinement, similar to the ones described in this thesis. One of the major advantage of SECS is that it is capable of measuring the addition spectrum to a quantum dot containing as few as one electron.

A combination of SECS and TDCS might allow one to measure the tunneling rate into single electron energy levels, as well as the excited states spectrum in quantum dots that contain only few electrons. Figure 6-3 illustrates this idea. In Fig. 6-3a, the bottom 3D electrode is in equilibrium with the quantum dot. An excitation voltage step of $V_1 = e/C$ (where C is the capacitance of the dot to the surroundings) is necessary to add an electron to the dot (Fig. 6-3b). We can further increase the excitation voltage to $V_2 = V_1 + \delta V$ so that the electron can also tunnel into the first excited state of the dot (Fig. 6-3c). Here δV is the quantum level spacing of the dot due to the lateral confinement. Since electrons can tunnel into both the ground state

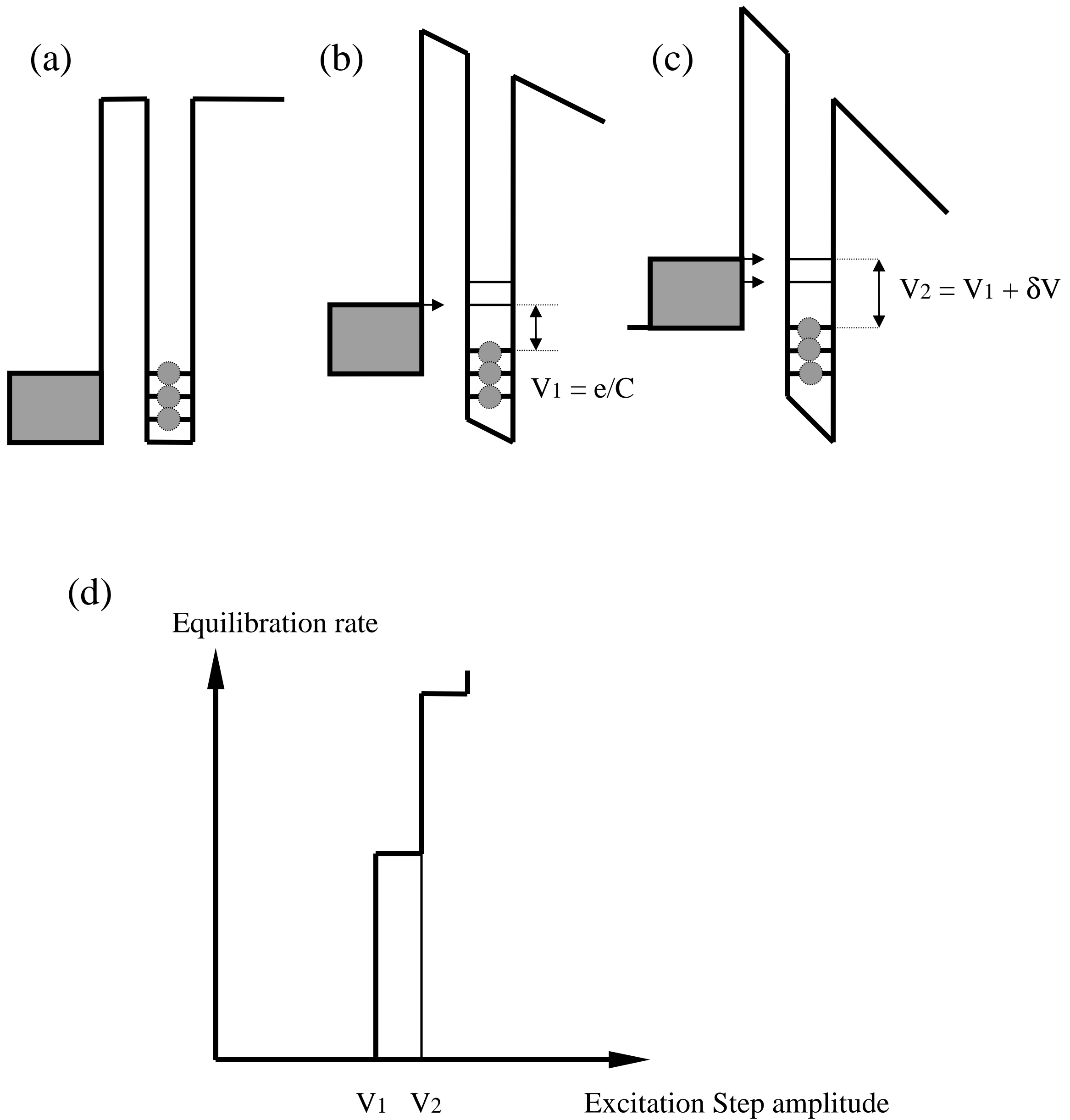

Figure 6-3: (a) Energy band diagram for a 3D electrode in equilibrium with a quantum dot consisting of 3 electrons. (b) An extra electron tunnels onto the dot when the excitation step voltage is $V_1 = e/C$. (c) When the excitation voltage equals $V_2 = V_1 + \delta V$ (where δV is the energy level spacing of the dot), electrons can tunnel into both the ground state and first excited state of the dot. (d) There is a sudden increase of the equilibration rates when the excitation amplitude reaches V_1 and V_2.

and the first excited state, the equilibration rate increases, as illustrated by Fig. 6-3d. Therefore, by measuring the dependence of equilibration rates as a function of voltage step amplitude, one can map out the excited states spectrum of the dot.

We have perform some preliminary experimental investigations of the feasibility of combining SECS and TDCS. We managed to resolve the addition energies of a dot by recording the time response using an EG&G 9825 averager (an earlier version of 9826) instead of using a lock-in amplifier as in SECS. However, we did not have the necessary bandwidth to determine the tunneling rates of current SECS samples. The major limitation is the coaxial cable connecting the sample to the preamplifer located outside the cryostat. There are two possible solutions to this problem. One can decrease the tunneling rate by designing samples with thicker tunnel barrier. Alternatively, one can apply a strong magnetic field to reduce the tunneling rate. In any case, we expect the combination of TDCS and SECS to be an extremely challenging experiment.

Appendix A

Extracting the Tunneling Current from Response of the Sample to a Step Voltage

This appendix describes how we deduce the current flowing across the tunneling barrier after application of the excitation voltage. As we mentioned in Chapter 2, there are no direct ohmic contacts to the 2DEG in our samples, and we cannot measure the tunneling current directly through conduction in the 2D plane. To measure the tunneling current, we utilize the fact that as electrons tunnel from the bottom 3D electrode into the 2D sheet, they repel electrons from the top electrode. We measure the displacement current I_D coming out of the top electrode by allowing this current to charge a standard capacitor C_S of known value. In this appendix, we show that the tunneling current is proportional to the time derivative of the voltage V_S across the standard capacitor:

$$I_{tunnel} = -C_{\Sigma} \frac{dV_S}{dt} \tag{A.1}$$

The proportionality constant C_{Σ} has dimensions of capacitance and is given by:

$$C_{\Sigma} = \frac{C_{block} C_{tunnel} + C_{tunnel} C_S + C_{block} C_S}{C_{block}} \tag{A.2}$$

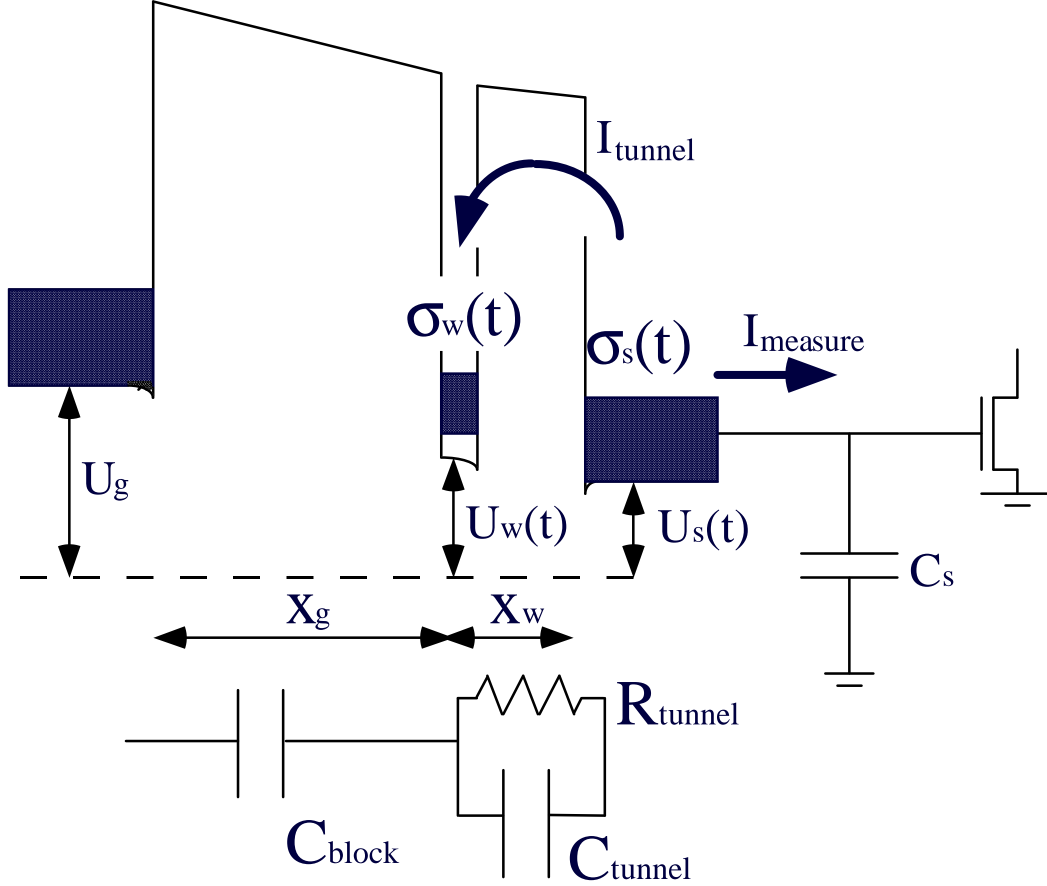

Figure A-1: This figure shows the band structure of the sample after application of the voltage step, with the equivalent circuit model of the sample underneath. The standard capacitor C_S and the transistor on the right are external circuit elements used to detect the tunneling current.

where C_{block} is the geometrical capacitance $\kappa A/x_g$ between the quantum well and the top electrode, while C_{tunnel} is the geometrical capacitance $\kappa A/x_w$ between the quantum well and the substrate. Here A is the area of the 2D system and κ is the dielectric constant of GaAs. Equation A.2 follows from charge conservation and Poisson's equation in a rather straightforward manner described below.

Figure A-1 shows the conduction band energy and equivalent circuit diagram of the sample, as well as the standard capacitor C_S and transistor used to detect the voltage V_S across C_S. Assuming a sheet charge model for electrons in the quantum well and

the two electrodes, Poisson's equation determines the following set of equations:

$$U_w(t) = U_S(t) - \frac{e^2}{\kappa} x_w \sigma_S(t) \tag{A.3}$$

$$U_g = U_S(t) - \frac{e^2}{\kappa}(x_w + x_g)\sigma_S(t) - \frac{e^2}{\kappa} x_g \sigma_w(t) \tag{A.4}$$

$\sigma_w(t)$ and $\sigma_S(t)$ represent the number density of excess electrons in the quantum well and the substrate respectively. $U_w(t)$ and $U_S(t)$ are the electrostatic potential energies at the conduction band edge of the quantum well and the substrate respectively, with respect to the potential energy at infinity (ground). U_g is the electrostatic potential energy of the conduction band edge of the top electrode, which is constant in time after application of the excitation voltage step. e is the magnitude of the electronic charge.

From charge conservation:

$$I_{tunnel}(t) + I_D(t) = A|e|\frac{d\sigma_S(t)}{dt} \tag{A.5}$$

$$I_{tunnel}(t) = -A|e|\frac{d\sigma_w(t)}{dt} \tag{A.6}$$

where I_{tunnel} is the tunneling current of interest that flows across the tunnel barrier and I_D is the displacement current coming out of the substrate. I_D charges the standard capacitor C_S:

$$I_D(t) = -\frac{C_S}{|e|}\frac{dU_S(t)}{dt} \tag{A.7}$$

U_S/e is the voltage on the top gate of C_S, which is amplified by the transistor and recorded. In practice, voltage steps of opposite polarity are applied to the other plate of C_S and the top electrode of the sample at precisely the same instant $t = 0$, as described in Chapter 2. For $t > 0$ the voltage on the bottom plate of the capacitor is constant, hence I_D is proportional to the time derivative of the voltage on the top capacitor plate in Eq. A.7.

From Eqs. A.3, A.4, A.5, A.6 and A.7, we eliminate $\sigma_w(t)$, $\sigma_S(t)$, $U_w(t)$ and $I_m(t)$, and write I_{tunnel} as a function of U_S. We outline the procedure below. First we take

the time derivative of Eq. A.3 and A.4:

$$\frac{d\sigma_S(t)}{dt} = \frac{\kappa}{e^2 x_w}\left[\frac{dU_S(t)}{dt} - \frac{dU_w(t)}{dt}\right] \tag{A.8}$$

$$\begin{aligned}\frac{d\sigma_w(t)}{dt} &= \frac{\kappa}{e^2 x_g}\frac{dU_S(t)}{dt} - \frac{(x_w + x_g)}{x_g}\frac{d\sigma_S(t)}{dt} &\text{(A.9)}\\ &= \frac{\kappa}{e^2 x_w}\left[\frac{(x_w + x_g)}{x_g}\frac{dU_w(t)}{dt} - \frac{dU_S(t)}{dt}\right] &\text{(A.10)}\end{aligned}$$

Equation A.10 follows from Eq. A.9 by substituting $d\sigma_S(t)/dt$ from Eq. A.8. Next we substitute Eqs. A.8 and A.10 into Eqs. A.5 and A.6 respectively to obtain:

$$I_{tunnel}(t) + I_D(t) = \frac{A\kappa}{|e| x_w}\left[\frac{dU_S(t)}{dt} - \frac{dU_w(t)}{dt}\right] \tag{A.11}$$

$$I_{tunnel}(t) = -\frac{A\kappa}{|e| x_w}\left[\frac{(x_w + x_g)}{x_g}\frac{dU_w(t)}{dt} - \frac{dU_S(t)}{dt}\right] \tag{A.12}$$

Since I_D is proportional to $dU_S(t)/dt$ as in Eq. A.7, we can eliminate $dU_w(t)/dt$ from Eqs. A.11 and A.12 to obtain a relation between I_{tunnel} and I_D:

$$I_{tunnel}(t) = -\left(\frac{C_{block}C_{tunnel} + C_{block}C_S + C_{tunnel}C_S}{C_{block}C_S}\right) I_D(t) \tag{A.13}$$

Substituting Eq. A.7 into Eq. A.13, we complete the derivation of Eq. A.1:

$$I_{tunnel}(t) = \left(\frac{C_{block}C_{tunnel} + C_{block}C_S + C_{tunnel}C_S}{C_{block}}\right)\frac{1}{|e|}\frac{dU_S(t)}{dt} = -C_\Sigma \frac{dV_S}{dt} \tag{A.14}$$

where C_Σ is given by Eq. A.2. The tunneling current is thus proportional to the time derivative of the voltage across the standard capacitor.

Note that Eq. A.14 does not contain explicitly the thermodynamic density of states $dN/d\mu$ of the 2D system. Provided that the capacitance bridge is properly balanced (section 2.4.2), variations of I_{tunnel} arising from finite $dN/d\mu$ are incorporated into the voltage signal $V_S(t)$, as we will describe below. In contrast, the relaxation rate of the chemical potential difference across the tunnel barrier does depend on $dN/d\mu$. To

illustrate the difference, let us consider the linear response limit when the excitation voltage is smaller than the thermal energy kT. In this limit, Ashoori found that the relaxation rate of the chemical potential across the tunnel barrier is given by [7]:

$$\frac{1}{\tau} = \frac{1}{\tau_{tunnel}} \left[\frac{Ae^2 g_s}{C_{tunnel}} (1 - \frac{x_w}{x_g}) + 1 \right] \tag{A.15}$$

where $1/\tau_{tunnel}$ is the mean tunneling rate per electron, determined by the thickness of the tunnel barrier. For simplicity, we assumed that the single-particle density of states g_s and thermodynamic density of states $dN/d\mu$ are identical. From Eq. A.15, when g_s goes to zero, the relaxation rate is equal to the tunneling rate:

$$\frac{1}{\tau} = \frac{1}{\tau_{tunnel}} \tag{A.16}$$

In other words, the relaxation rate does not go to zero even when the density of states vanishes. The tunneling current, nevertheless, must go to zero since there are no states in the 2D system for electrons to tunnel into. There is no contradiction because the tunneling current is proportional to the initial time derivative of the voltage across the standard capacitor V_S that is equivalent to the product of the initial voltage $V_S(t = 0)$ and the relaxation rate $1/\tau$, as we described in section 2.4.3:

$$I_{tunnel} \propto -\frac{dV_S}{dt}|_{t=0} = V_S(t = 0)\frac{1}{\tau} \tag{A.17}$$

$V_S(t = 0)$ is proportional to the amount of charge transferred into the 2D system in the tunneling process when an excitation voltage step is applied. Variations of I_{tunnel} arising from finite $dN/d\mu$ are contained implicitly in $V_S(t)$. For instance, in the limit when the density of states of the 2D system vanishes, there is no tunneling of electrons and $V_S(t = 0)$ goes to zero. From Eq. A.17, the tunneling current goes to zero accordingly even though the relaxation rate $1/\tau$ remains non-zero as given by Eq. A.16.

Appendix B

Increasing Voltage Resolution by Digital Dithering

This appendix describes the dithering technique we used to increase the voltage resolution of the signal averager. We designed our dithering circuit and software based on the Ph.D. thesis of Monroe [62] and Stathis [63]. There have been significant improvements in the speed of electronics since Monroe and Stathis implemented their analog dithering circuit. We are able to construct a dithering scheme based on a digital-to-analog voltage card inserted into the same computer where the 9826 signal averager resides.

The analog-to-digital convertors (ADC's) in the signal averager has a voltage resolution of 8 bits. We find that such resolution is inadequate for our experiment which requires accurate measurement of the initial time derivative of the signal. It is necessary to increase the effective resolution of the ADC's by a "digital dithering" technique. Fig. B-1 illustrates the basic concept of dithering. Suppose the signal that we are measuring is a linear ramp. The digitized signal recorded will be a series of steps no matter how many times we average the signal (Fig. B-1a) if the root-mean-square noise is smaller than the resolution δ of the ADC. In Fig. B-1b we add to the signal a DC offset of $\delta V/2$ and therefore change the horizontal positions of the steps of the averager output. If we now average the two waveforms in Figs. B-1a and b, we obtain a result that is a more accurate representation of the original ramp

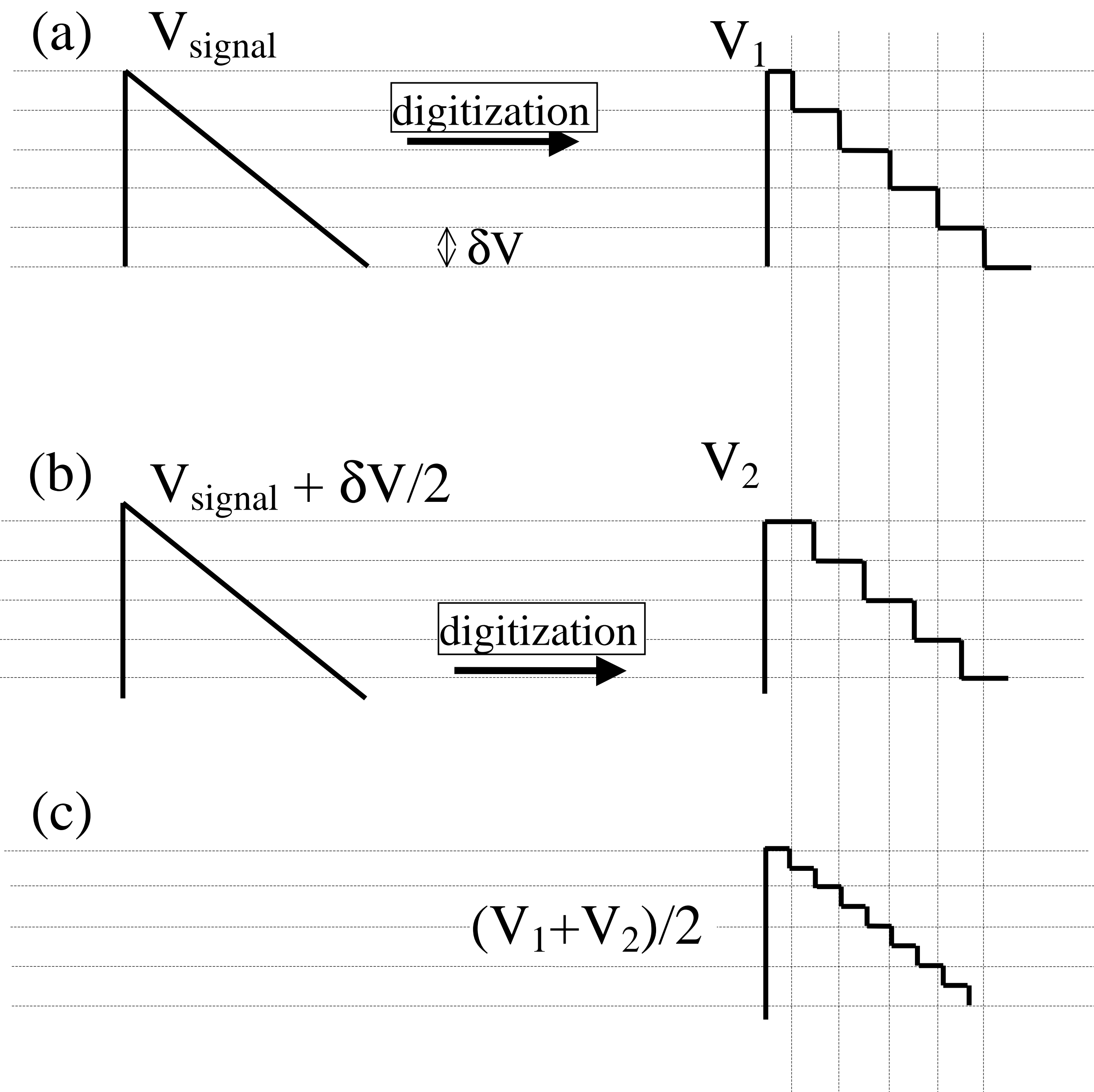

Figure B-1: Demonstration of the effect of dithering on a linear ramp signal. (a) Digitization of the ramp produces a series of steps. (b) Digitization of the ramp offset by half the voltage resolution leads to a series of step slightly shifted in time. (c) Averaging the digitized signal in (a) and (b) effectively increased the resolution by a factor of 2.

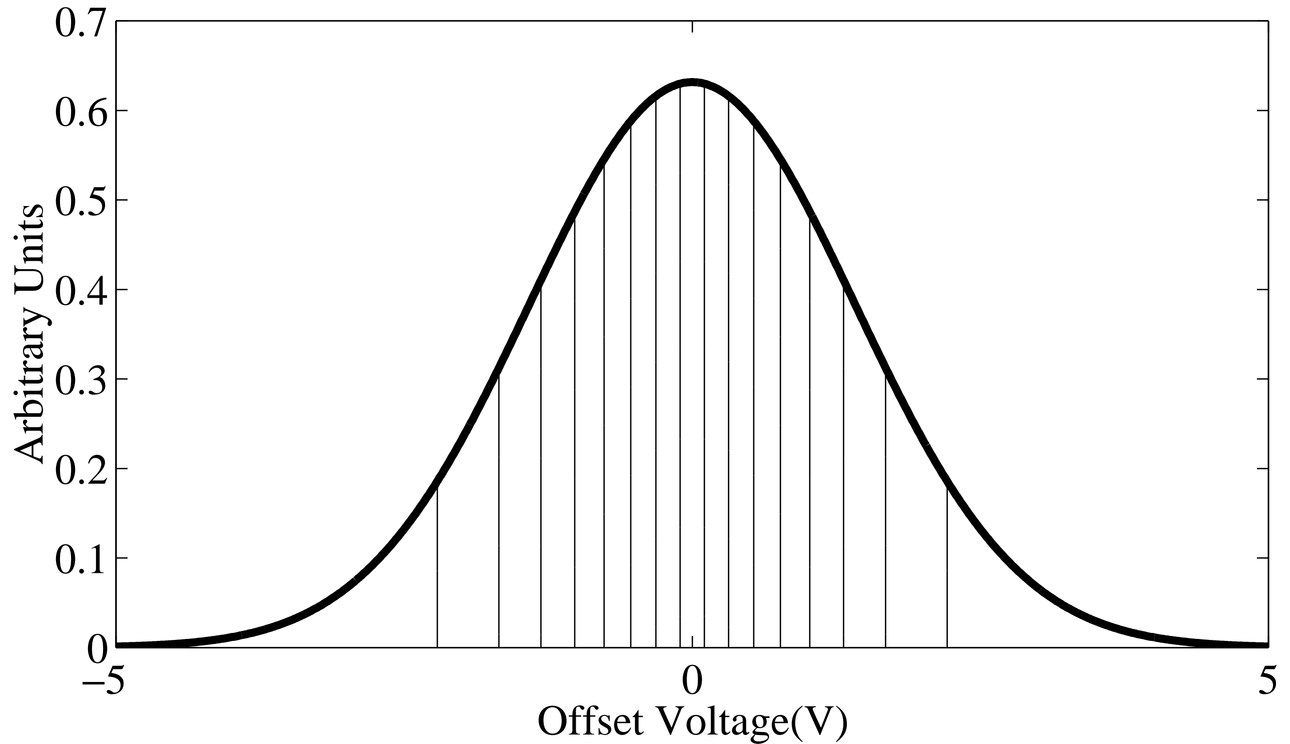

Figure B-2: The dithering voltages partition the area under a Guassian distribution equally. In this example, there are 16 dithering voltages. The standard deviation of the Guassian is $1V$ and the area under the Guassian is normalized to 1. Area between two adjacent thin vertical lines is constant and equal to $1/16$.

(Fig. B-1c). Instead of using only 2 DC offset voltages, we use as many as 256 DC offsets to obtain each time trace in our experiment.

We select the DC offsets so that they partition the area under a Gaussian equally, as shown in Fig. B-2 for the case of only 16 offset voltages. To avoid non-uniformity in the separation between adjacent bits in the ADC's, we use the largest possible width for the Guassian while keeping the trace with the DC offset in range of the averager. This way we utilize the full range of the averager for each averaged time trace.

Through dithering, we effectively increase the vertical resolution of the averager from 8 bit to 16 bit, a 256-fold improvement.

Appendix C

Sample Fabrication

In this appendix we describe the fabrication process of our samples. Our typical sample contains a quantum well sandwiched between two electrodes, as we described in Chapter 2. The goal of the fabrication process is to make independent electrical contacts to the top and bottom n-doped GaAs without shorting to the quantum well. For samples without dopants in the AlGaAs blocking barrier described in Chapters 3 and 4, it is rather straightforward to create the top Schottky contact. In contrast, making the top ohmic contacts to the high mobility samples in Chapter 5, which do not contain dopants in the AlGaAs blocking barrier, requires more caution. In the fabrication of ohmic contacts between metal and semiconductors, it is desirable to have a low and linear contact resistance. The contacts in our samples are no exception. However, at the same time we need to prevent the metalization from penetrating too deep into our heterostructure so that it shorts the top electrode to the quantum well. We adopt a fabrication process that compromises between these two requirements.

The most common metalization for making ohmic contacts to n-doped GaAs is germanium/gold/nickel [64]. Unfortunately, upon annealing, the metalization penetrates up to 1 μm into the GaAs, a distance comparable to the thickness of our top n-doped GaAs layer. We found indeed that almost all of our samples have the top and bottom electrodes shorted if we use germanium/gold/nickel as the top metalization. Therefore, germanium/gold/nickel metalization is not acceptable for the top ohmic contact. Instead we have to use the less penetrating germanium/palladium/gold

contact, based on solid phase epitaxy [65, 66, 67]. The adaptation of the germanium/palladium/gold contact increases the yield of working samples to an acceptable level. We describe the procedure for making the germanium/palladium/gold contact in detail in this appendix.

Mesa isolation is another essential step in the fabrication process. For samples with dopants in the AlGaAs blocking barrier, the chromium-gold Schottky contact provides a stable enough etching mask to protect the GaAs wafer that it covers. However, we find that both germanium/gold/nickel and germanium/palladium/gold metalization peal off from the GaAs wafer after a standard sulphuric acid/hydrogen peroxide/water wet etch. It seems likely that the etchant attacks germanium in the metalization. Therefore, we need to perform a second lithographic step to cover the metalization with photoresist for the wet etch. This step is not necessary for the samples with chromium/gold Schottky contacts.

C.1 Fabrication Procedure for Samples with Schottky Top Electrode

In Chapters 3 and 4 we measured samples with dopants in the AlGaAs blocking barriers. As described in sections 3.2 and 4.1, these samples consist of undoped GaAs top layers and the top metalization forms Schottky contacts. The fabrication procedures for these samples are as follows:

1. Glue samples face down onto a glass glide using PMMA. Bake glass slide with the samples at 130^oC for 1 minute so that the PMMA hardens.

2. After a quick etch using 1:8:1000 $H_2SO_4/H_2O_2/H_2O$ for $\sim$ 15 seconds, load the sample into an evaporator and deposit metallic layers according to the following sequence and thickness: nickel 50 $\AA$, germanium 450 $\AA$, gold 40 $\AA$, nickel 350 $\AA$, gold 1500 $\AA$.

3. Clean the samples in acetone to strip the PMMA. Then anneal the samples at 425^oC for 30 seconds in nitrogen gas to form the bottom contact.

4. Pattern samples with a negative photoresist NR8-1000 to facilitate metal lift off in step 6.

5. Glue samples to glass slide using PMMA. Put samples in UV asher to get rid of photoresist residuals in the exposed regions. Load in evaporator and deposit 50 $\AA$ of chromium and 1250 $\AA$ of gold.

6. Metal liftoff by putting the samples in acetone with ultrasonic agitation.

7. Wet etch to isolate the mesas using the metalization as etching mask. The etchant is 1:8:1000 $H_2SO_4/H_2O_2/H_2O$. It removes GaAs at about 400 $\AA$/min with constant stirring. For our samples with mesas up to 100 μm in diameter, etch until the bottom n doped GaAs is reached.

8. Using silver epoxy, attach the sample onto a piece of GaAs, slightly larger than the sample and evaporated with gold. The back contact is now accessible through the gold on base piece of GaAs.

C.2 Fabrication Procedure for Samples with Ohmic Top Electrode

In Chapter 5 we studied very high mobility samples with no dopants in the AlGaAs blocking barrier. We obtained these samples from Loren Pfeiffer and Ken West (Bell laboratory, Lucent Technologies). During MBE growth, the back side of the samples are usually covered by gallium that must be removed to form the bottom ohmic contact. The top layer of the wafer is n+ doped GaAs. In order to avoid the top ohmic contact from penetrating too deep to short the quantum well, the fabrication procedures for these samples are more complicated:

1. Glue samples face down onto a glass glide using photoresist to protect the front side. Put sample in hydrochloric acid to dissolve the gallium on the back surface. Heating might be necessary. However the temperature must be kept below 70^oC to avoid damaging the photoresist protection of the front side.

2. Remove the samples from the glass slide using acetone. Re-glue samples face down onto a glass glide using PMMA. Bake the glass slide with the samples at 130^oC for 1 minute so that the PMMA hardens. This step is necessary because PMMA holds the samples better than regular photoresist when the samples are heated during metal evaporation.

3. After a quick etch using 1:8:1000 $H_2SO_4/H_2O_2/H_2O$ for $\sim$ 15 seconds, load the sample into an evaporator and deposit metallic layers according to the following sequence and thickness: nickel 50 $\AA$, germanium 450 $\AA$, gold 40 $\AA$, nickel 350 $\AA$, gold 1500 $\AA$.

4. Clean the samples in acetone to strip the PMMA. Then anneal the samples at 425^oC for 30 seconds in nitrogen gas to form the bottom contact.

5. Pattern samples together with an ordinary n doped GaAs test wafer with a negative photoresist NR8-1000 to facilitate metal lift off in step 7.

6. Glue samples and test wafer to a glass slide using PMMA. Put glass slide in UV asher to get rid of photoresist residuals in the exposed regions. Load in evaporator and deposit metal according to the following sequence and thickness: palladium 500 $\AA$, germanium 1275 $\AA$, gold 1400 $\AA$.

7. Metal liftoff by putting the samples in acetone with ultrasonic agitation.

8. Anneal the test wafer for 20 minutes in nitrogen gas at different temperatures in the range of 240^oC to 290^oC. Then test the contact resistance at liquid nitrogen temperature. This test is necessary because the lowest temperature to achieve ohmic contacts differs for each run. Typically a minimum temperature of 265^oC is necessary for good ohmic contact. Anneal the sample at a temperature 10^oC above the minimum contact temperature for 20 minutes. Test the contacts at liquid nitrogen temperature to make sure it is ohmic.

9. Align and pattern the samples with a positive photoresist, which acts as etching masks in a step 10. Use a lithography mask with features 5 μm larger than the

metal pattern to completely cover the metal with photoresist.

10. Wet etch to isolate the mesas using the photoresist as etching mask. The etchant is 1:8:100 $H_2SO_4/H_2O_2/H_2O$. It removes GaAs at about 4000 $\AA$/min with constant stirring. For our samples with mesas up to 100 μm in diameter, etch until the bottom n doped GaAs is reached.

11. Dissolve the photoresist in acetone.

12. Using silver epoxy, attach the sample onto a piece of GaAs slightly larger than the sample and evaporated with gold, through which the back contact of the sample is accessible.

Bibliography

[1] K. von Klitzing, G. Dorda, and M. Pepper. New method for high-accuracy determination of the fine-structure constant based on quantized Hall resistance. *Physical Review Letters*, 45:494, 1980.

[2] T. Ando and Y. Uemura. Theory of quantum transport in a two-dimensional electron system under magnetic fields.

[3] S. L. Sondhi, A. Karlhede, S. A. Kivelson, and E. H. Rezayi. Skyrmions and the crossover from the integer to fractional quantum hall effect at small zeeman energies. *Physical Review B*, 47:16419, 1993.

[4] H. A. Fertig, L. Brey, R. Côté, and A. H. MacDonald. Charged spin-texture excitations and the hartree-fock approximation in the quantum hall effect. *Physical Review B*, 50:11018, 1994.

[5] A. L. Efros and B. I. Shklovskii. Coulomb gap and low temperature conductivity of disordered systems. *J. Phys. C.*, 8, 1975.

[6] B. L. Altshuler, A. G. Aronov, and P. A. Lee. Interaction effects in disordered fermi systems in two dimensions. *Physical Review Letters*, 44:1288, 1980.

[7] R. C. Ashoori. *The Density of States in the Two-Dimensional Electron Gas and Quantum Dots*. PhD thesis, Cornell University, 1991.

[8] Y. Imry and Z. Ovadyahu. Density-of-states anomalies in a disordered conductor: A tunneling study. *Physical Review Letters*, 49:841, 1982.

[9] A. E. White, R. C. Dynes, and J. P Garno. Correction to the two-dimensional density of states. *Physical Review B*, 31:1174, 1985.

[10] M. E. Gershenzon, V. N. Gubankov, and M. I. Faleĭ. Effect of the electron-electron interaction on state density in 2d aluminum films. *JETP Lett.*, 41:534, 1985.

[11] M. E. Gershenzon, V. N. Gubankov, and M. I. Faleĭ. Tunnel spectroscopy of the electron-electron interaction in disordered aluminum flims. *Sov. Phys. JETP*, 63:1287, 1986.

[12] Jr. J. M. Valles, R. C. Dynes, and J. P. Garno. Temperature dependence of the two-dmiensional electronic density of states in disordred metal films. *Physical Review B*, 40:7590, 1989.

[13] Shih-Ying Hsu and Jr. J. M. Valles. Electron tunneling into strongly disordered films: The influence of structure on electron-electron interactions. *Physical Review B*, 49:16600, 1994.

[14] Wenhao Wu, J. Williams, and P. W. Adams. Zeeman splitting of the coulomb anomaly: A tunneling study in two dimensions. *Physical Review B*, 77:1139, 1996.

[15] J. P. Eisenstein, L. N. Pfeiffer, and K. W. West. Coulomb barrier to tunneling between parallel two-dimensional electron systems. *Physical Review Letters*, 69:3804, 1992.

[16] P. W. Anderson. Absence of diffusion in certain random lattices. *Physical Review*, 109:1492, 1958.

[17] B. L. Altshuler and A. G. Aronov. Electron-electron interaction in disordered conductors. In A. L. Efros and M. Pollak, editors, *Electron-Electron Interactions In Disordered Systems*, chapter 1, pages 1–153. Elsevier Science Publishers, 1985.

[18] J. A. Lebens. *A study of tunneling phenomena in gallium arsenide-aluminum gallium arsenide heterostructures*. PhD thesis, Cornell University, 1988.

[19] R. C. Ashoori, J. A. Lebens, N. P. Bigelow, and R. H. Silsbee. Equilibrium tunneling from the two-dimensional electron gas in GaAs: Evidence for a magnetic-field-induced energy gap. *Physical Review Letters*, 64:681, 1990.

[20] R. C. Ashoori, J. A. Lebens, N. P. Bigelow, and R. H. Silsbee. Energy gaps of the two-dimensional electron gas explored with equilibrium tunneling spectroscopy. *Physical Review B*, 48:4616, 1993.

[21] H. B. Chan, P. I. Glicofridis, R. C. Ashoori, and M. L. Melloch. Universal linear density of states for tunneling into the two-dimensional electron gas in a magnetic field. *Physical Review Letters*, 79:2867, 1997.

[22] A. M. Rudin, I. L. Aleiner, and L. I. Glazman. Tunneling zero-bias anomaly in the quasiballistic regime. *Physical Review B*, 55:9322, 1997.

[23] L. S. Levitov and A. V. Shytov. Semiclassical theory of the coulomb anomaly. *JETP Lett.*, 66:214, 1997.

[24] J. C. Maxwell. In *A Treatise on Electricity and Magnetism*, volume II, chapter XII, page 296. Oxford: Clarendon Press, 1892.

[25] F. G. Pikus and A. L. Efros. Coulomb gap in two-dimensional electron gas with a close metallic electrode. *Physical Review B*, 51:16871, 1995.

[26] G. Bergmann. Weak localization in thin films: a time of flight experiment with conduction electrons. *Physics Report*, 107:1, 1984.

[27] D. J. Bishop, R. C. Dynes, and D. C. Tsui. Magnetoresistance in Si metal-oxide-semiconductor field-effect transistors: Evidence of weak localization and correlation. *Physical Review B*, 26:773, 1982.

[28] S. Chakravarty and A. Schmid. Weak localization: the quasiclassical theory of electrons in a random potential. *Physics Reports*, 140:193, 1986.

[29] B. Kramer and A. MacKinnon. Localization: theory and experiment. *Rep. Prog. Phys.*

[30] B. L. Altshuler, A. G. Aronov, M. E. Gershenson, and Yu. V. Sharvin. Quantum effects in disordered metal films. *Sov. Sci. Rev. A. Phys.*, 9:223, 1987.

[31] K. M. Brown, N. Turner, J. T. Nicholls, E. H. Linfield, M. Pepper, D. A. Ritchie, and G. A. C. Jones. Tunneling between two-dimensional electron gases in a strong magnetic field. *Physical Review B*, 50:15465, 1994.

[32] V.T. Dolgopolov, H. Drexler, W. Hansen, J.P. Kotthaus, and M. Holland. Electron correlations and coulomb gap in two-dimensional electron gas in high magnetic fields. *Physical Review B*, 51:7958, 1995.

[33] I. L. Aleiner, H. U. Baranger, and L. I. Glazman. Tunneling into a two-dimensional electron liquid in a weak magnetic field. *Physical Review Letters*, 74:3435, 1995.

[34] Song He, P. M. Platzman, and B. I. Halperin. Tunneling into a two-dimensional electron system in a strong magnetic field. *Physical Review Letters*, 71:777, 1993.

[35] Peter Johansson and Jari M. Kinaret. Magnetophonon shakeup in a wigner crystal: Applications to tunneling spectroscopy in the quantum hall regime. *Physical Review Letters*, 71:1435, 1993.

[36] A. A. Koulakov, M. M. Fogler, and B. I. Shklovskii. Charge density wave in two-dimensional electron liquid in weak magnetic field. *Physical Review Letters*, 76:499, 1996.

[37] C. M. Varma, A. I. Larkin, and E. Abrahams. Correlated state of double layerss of electron fluids. *Physical Review B*, 49:13999, 1994.

[38] S.-R. Eric Yang and A. H. MacDonald. Coulomb gaps in a strong magnetic field. *Physical Review Letters*, 70:4110, 1993.

[39] R. E. Cavicchi and R. H. Silsbee. Coulomb suppression of tunneling rate from small metal particles. *Physical Review Letters*, 52:1453, 1984.

[40] J. J. Palacios and H. A. Fertig. Signature of quantum hall effect skyrmions in tunneling: A theoretical study. *Physical Review Letters*, 79:471, 1997.

[41] D. K. Maude, M. Potemski, J. C. Portal, M. Henini, L. Eaves, G. Hill, and M. A. Pate. Spin excitations of a two-dimensional electron gas in the limit of vanishing landé g factor. *Physical Review Letters*, 77:4604, 1996.

[42] D. R. Leadley, R. J. Nicholas, D. K. Maude, A. N. Utjuzh, J. C. Portal, J. J. Harris, and C. T. Foxon. Fractional quantum hall effect measurements at zero g factor. *Physical Review Letters*, 79:4246, 1997.

[43] D. R. Leadley, R. J. Nicholas, D. K. Maude, A. N. Utjuzh, J. C. Portal, J. J. Harris, and C. T. Foxon. Searches for skyrmions in the limit of zero g factor. *Semicond. Sci. Technol.*, 13:671, 1998.

[44] S. E. Barrett, G. Dabbagh, L. N. Pfeiffer, K. W. West, and R. Tycko. Optically pumped nmr evidence for finite-size skyrmions in gaas quantum wells near landau level filling $\nu = 1$. *Physical Review Letters*, 74:5112, 1995.

[45] E. H. Aifer, B. B. Goldberg, and D. A. Broido. Evidence of skyrmion excitations about $\nu = 1$ in n-modulation-doped single quantum wells by interband optical transmission. *Physical Review Letters*, 76:680, 1996.

[46] A. Schmeller, J. P. Eisenstein, L. N. Pfeiffer, and K. W. West. Evidence for skyrmions and single spin flips in the integer quantized hall effect. *Physical Review Letters*, 75:4290, 1995.

[47] V. Bayot, E. Grivei, S. Melinte, M. B. Santos, and M. Shayegan. Giant low temperature heat capacity of GaAs quantum wells near landau level filling $\nu = 1$. *Physical Review Letters*, 76:4584, 1996.

[48] V. Bayot, E. Grivei, J.-M. Beuken, S. Melinte, and M. Shayegan. Critical behavior of nuclear-spin diffusion in GaAs/AlGaAs heterostructures near landau level filling $\nu = 1$. *Physical Review Letters*, 79:1718, 1997.

[49] D. C. Tsui, H. L. Stormer, and A. C. Gossard. Two-dimensional magnetotransport in the extreme quantum limit. *Physical Review Letters*, 48:1559, 1982.

[50] N. N. Kuzma, P. Khandelwal, S. E. Barrett, L. N. Pfeiffer, and K. W. West. Ultraslow electron spin dynamics in GaAs quantum wells probed by optically pumped NMR. *Science*, 281:686, 1998.

[51] A. H. MacDonald. Spin bottlenecks in the quantum hall regime. *LANL cond-mat 9906049*, 1999.

[52] A. M. Rudin, I. L. Aleiner, and L. I. Glazman. Interaction-induced oscillations of the tunneling density of states in a nonquantizing magnetic field. *Physical Review Letters*, 78:709, 1997.

[53] A. M. Rudin, I. L. Aleiner, and L. I. Glazman. Density of states of a two-dimensional electron gas in a nonquantizing magnetic field. *Physical Review B*, 58:15698, 1998.

[54] M. P. Lilly, K. B. Cooper, J. P. Eisenstein, L. N. Pfeiffer, and K. W. West. Evidence for an anisotropic state of two-dimensional electrons in high landau levels. *Physical Review Letters*, 82:394, 1999.

[55] H. L. Stormer, D. C. Tsui, and A. C. Gossard. The fractional quantum hall effect.

[56] M. Greiter, X. G. Wen, and F. Wilczek. Paired hall state at half filling. *Physical Review Letters*, 66:3205, 1991.

[57] G. Moore and N. Read. Signature of quantum hall effect skyrmions in tunneling: A theoretical study. *Nuclear Physics B*, 360:362, 1991.

[58] B. I. Halperin, P. A. Lee, and N. Read. Theory of the half-filled Landau level. *Physical Review B*, 47:7312, 1993.

[59] M. A. Kastner. Artifical atoms.

[60] R. C. Ashoori. Electrons in artificial atoms.

[61] R. C. Ashoori, H.L. Stormer, J.S. Weiner, L.N. Pfeiffer, S.J. Pearton, K.W. Baldwin, and K.W. West. Single-electron capacitance spectroscopy of discrete quantum levels. *Physical Review Letters*, 68:3088, 1992.

[62] D. P. Monroe. *Transient transport and optical studies of chalcogenide glasses*. PhD thesis, Massachusetts Institute of Technology, 1985.

[63] J. H. Stathis. *Optically induced metastable defect states in amorphous silicon dioxide*. PhD thesis, Massachusetts Institute of Technology, 1986.

[64] Ralph Williams. Ohmic contacts. In *Modern GaAs Processing Methods*, chapter 11, page 220. Artech House, 1990.

[65] E. D. Marshall, W. X. Chen, C. S. Wu, S. S. Lau, and T. F. Keuch. Non-alloyed ohmic contact to n-GaAs by solid phase epitaxy. *Appl. Phys. Lett*, 47:298, 1985.

[66] E. D. Marshall, B. Zhang, L. C. Wang, P. F. Jiao, W. X. Chen, T. Sawada, S. S. Lau, K. L. Kavanagh, and T. F. Keuch. Nonalloyed ohmic contacts to n-GaAs by solid-phase epitaxy of ge. *J. Appl. Phys.*, 62:942, 1987.

[67] C. L. Chen, L. J. Mahoney, M. C. Finn, R. C. Brooks, A. Chu, and J. G. Mavroides. Low resistance Pd/Ge/Au and Ge/Pd/Au ohmic contacts to n-type GaAs. *Appl. Phys. Lett*, 48:535, 1986.